INSTABILITY AND BUCKLING ANALYSIS OF STRETCHABLE SILICON SYSTEM

LIU ZHUANGJIAN

B. Sci., Tianjian University, China

M. Eng., Tongji University, China

M. Eng., National University of Singapore, Singapore

A THESIS SUBMITTED

FOR THE DEGREE OF DOCTOR OF PHILOSOPHY

DEPARTMENT OF CIVIL ENGINEERING

NATIONAL UNIVERSITY OF SINGAPORE

2009

Acknowledgements

This work would not have been possible without the contributions from many people. Therefore, I am deeply indebted to them all.

First and foremost, I would like to express my sincere gratitude to my supervisors, Professor KOH, Chan Ghee for constant guidance and help throughout my graduate studies and the preparation of this thesis. His patience, guidance and suggestions have been very helpful. Besides, I would also like to pay tribute to Dr. LU, Chun, Professor GUO, Junke and Professor LIN, Pengzhi for their valuable observations and suggestions in some stages of the research. Thanks are also due to many academic, technical and administrative staff for their support and assistance throughout the study.

I would like to thank Professor HUANG, Yonggang at Northwestern University and Dr. SONG, Jizhou at University of Miami, for their help in the realization of this work. I would also like to thank Professor ROGERS, John A., Dr. KHANG, Dahl-Young and Dr. KIM, Dae-Hyeong at University of Illinois at Urbana-Champaign, for their great help during my experimental investigation. They played a significant role in giving useful suggestions and discussions in my studies.

Appreciation is extended to the Institute of High Performance Computing (IHPC). The support provided by IHPC is gratefully acknowledged. The assistance

provided by my colleagues in IHPC during the numerical simulation stage of works is also greatly appreciated.

Finally, I would like to thank my wife and my family for all that they have done for me. And I wish to thank my parents, Professors LIU, Xunbo and DAI, Minliu, for their attention, patience, best wishes, and the love given. I also wish to thank my sister, Dr. LIU, Zhuangwei, for her continuous help in every situation I requested them.

Table of Contents

Summary

Stretchable electronics have great potential for applications in unconventional electronics, e.g. eyelike digital cameras, conformable skin sensors, intelligent surgical gloves, and structural monitoring devices. A traditional focus of this field is on the development of materials for circuits that can be formed on bendable substrates, such as plastic sheets or steel foils. Recently, much effort has been invested to achieve similar system on fully elastic substrates for electronics that can be stretched, compressed, twisted and deformed in ways that are much more flexible than ever. The wrinkling of a stiff thin film on a compliant substrate is of particular interest to achieve this aim. The design of these stretchable electronics systems encompasses a range of forms, from simple layouts consisting of single crystal silicon thin films on flat substrates to complex lithographically patterned films on substrates with structures of relief embossed on their surfaces.

Mechanics of materials underlies the development of this type of stretchable electronics. Various kinds of surface patterns at the micrometer scale are generated due to instability and buckling of thin films on a compliant substrate, and hence this area of work has recently attracted more attention. In this system, there is an interface stress due to a large mismatch in Young's moduli of two materials when this system in tension or compression. The highly ordered wave patterns, e.g. periodic waves, checkerboard, herringbone, and interacting wave patterns, are caused by interface stress. The desired mechanical properties are realized not through new materials but instead through new structural configurations of existing materials. These wrinkle patterns can be analyzed by mechanics theory and simulated by numerical methods.

In this study, the fabrication procedure of stretchable silicon systems is carried out. Controlled buckling is realized in single crystal silicon thin films initially, then deposited, typically by a vapor phase or physical transfer processes, onto prestrained elastomeric substrates. The desired mechanical properties are realized not through new materials but instead through new structural configurations which are established in the fabrication process. High performance, stretchable and foldable integrated circuits are also developed using this process. Then, an analytical study is performed to find a closed form solution for this buckling mode. Critical buckling strain is obtained based on linear analytical solutions. The wavelength and amplitude are then predicted for the buckling and post-buckling phases. To improve the accuracy of results, a non-linear closed form analytical solution is derived. The analytical study gives the wavelength and amplitude directly in terms of the film and substrate elastic properties, the thin film thickness, and the film prestrain.

Two and three dimensional finite element models are constructed for numerical analysis of single crystal silicon and integrated circuit with multilayer thin film substrate systems, respectively. The simulation results exhibit good agreement with experimental observation. The periodic, wave-like geometry can be represented well numerically using the finite element model. It is found that, when a thin film of stiff material is suitably patterned on a compliant substrate, a large elongation of the substrate induces small strains in the thin film, and the thin film accommodates the large elongation. The unique mechanical characteristics of wavy devices and the coupling of strain to electronic properties could provide insight into the design of device structures to achieve unusual electronic behaviour.

Key words: Buckling, Finite element method, Solid mechanics, Stretchable electronics.

List of Figures

List of Symbols

A and A''	Amplitude
$\mathbf{B}$	Strain-displacement matrix
D	Bending stiffness of plate
C_1 and C_2	Material parameters
$\mathbf{E}$	Stress-strain matrix
E_{IJ}	Green strain
E_f	Young's modulus of plate or thin film,
E_s	Young's modulus of substrate,
F_{iJ}	Deformation gradient
F^N	Force component
H	Substrate thickness
$\bar{I}_1$	Trace of left Cauchy-Green strain tensor
I_1	First strain invariant
J	Elastic volume strain
L	Stretched length of silicon ribbon
L_0	Initial length of silicon ribbon
L_c	Channel lengths
L_{edge}	Edge-effect length
$M_{\alpha\beta}$	Bending moment tensor
n_J	Unit normal vector of surface

$N_{ui}, N_{vi}, N_{wi}, N_{xi}, N_{yi}$	Shape functions
$N_{\alpha\beta}, N_{11}, N_{22}, N_{12}$	Uniform stress and components in plane or thin film
N_{cr}	Critical membrane force
R_c	Radius of curvature at the peak or trough of wave
p	Stress component acting perpendicular to the plate,
t	Thin film thickness
T_{IJ}	2nd Piola-Kirchoff stress
T_1, T_2 and T_3	Traction force components
T_D	Temperature
U	Strain energy
U^b	Bending strain energy in plate or thin film
U^m	Membrane strain energy in plate or thin film
U^s	Strain energy in the substrate
u, v or u_1, u_2	In-plane displacements
w	Displacement perpendicular to plane or film deflections
w_i	i-th eigenmode
W	Channel width
W^b	Bending energy density in plate or thin film
W^m	Membrane energy density in plate or thin film
W^s	Strain energy density in substrate
x_1, x_2, x_3	Cartesian coordinates
x_1'', x_2'', x_3''	Cartesian coordinates after stretching
α_s	Coefficient of thermal expansion

$\delta_{\alpha\beta}$	Kronecker delta $\delta_{\alpha\beta} = \begin{cases} 1, & if\ \alpha = \beta \\ 0, & if\ \alpha \neq \beta \end{cases}$
$\varepsilon_{\alpha\beta}$ and ε_{11}^{0}, ε_{22}^{0}, ε_{12}^{0}	Membrane strains components
$\varepsilon_{applied}$	Applied strain
ε_{cr}	Critical buckling strain
$\varepsilon_{fracture}$	Fracture strain
ε_{pre}	Prestrain
ε_{Si}^{peak}	Strain at peak (or trough) in wavy silicon ribbon
ε_{Si}	Silicon ribbon strain of wave
$\varepsilon_{bending}$	Bending strain
ε_{s}	Strain in substrate
ε_{f}	Strain in thin film
ε_{mem}	Membrane strain
ε_{peak}	Peak strain
ϕ_{i}	Scaling factor
k_{eq}	Wave number
λ and λ''	Wavelength
$\lambda_{\cot our}$	Contour length of wave
ν_{f}	Poisson's ratio of the plate (i.e. thin film)
ν_{s}	Poisson's ratio of substrate
σ_{0}	Prestress
σ_{cr}	Critical buckling stress

Chapter One

Introduction

1.1 Background

Most electronic circuits are not stretchable because they come in the form of rigid chips. Truly flexible circuits are made of organic semiconductors sprayed or stamped onto plastic sheets. Currently organic semiconductors, although useful for flexibility reasons, are slow for intensive computing tasks (Crone, et al., 2000). Silicon or other high-speed inorganic semiconductors based on elastomeric substrates are required for bendable and stretchable electronics systems (Yuan, et al., 2006). This is why stretchable silicon was selected as one of the ten emerging technologies by MIT Technology Review (Greene, 2006). Recently, a method has been found to stretch crystal silicon (Khang, et al., 2006) and then fabricate it into integrated circuits (Kim, et al., 2008). The work involved the use of single crystal silicon which is the same type of silicon found in microprocessors. However, as with other crystal materials, single crystal silicon does not stretch naturally. In order for it to be bendable and stretchable, it has to be prepared as an ultrathin layer only a few hundred nanometers thick on a bendable surface (Rogers, 2001). Instead of attaching the single crystal silicon to a plastic substrate, the new method involves affixing single crystal silicon in narrow strips onto a stretched, rubber-like polymer. When the stretched polymer snaps back into its natural relaxed state, the silicon strips buckle, but do not break, forming wrinkling waves that are ready to be stretched out again. Recently this process has been extended to the fabrication of integrated circuits (Kim, et al., 2008). The high performance, stretchable and foldable integrated circuits are developed using the same approach. This inorganic electronic device is systematically structured into aligned arrays of nanoribbons of single crystal silicon, with ultrathin plastic and elastomeric substrates. The designs combine multilayer layouts and ‘wavy’ structural configurations in silicon complementary logic gates, ring oscillators and differential amplifiers. This is a different conceptual approach to stretchable electronics. The desired mechanical properties are realized not through new materials but instead through new structural configurations which are established in the fabrication process. To understand the mechanism of this new structural material, analytical and computational models are developed here to investigate the mechanics characteristics in both single crystal silicon and integrated circuit systems. The results show that this type of stiff thin film-compliant substrate system has good potential of application for devices that require extreme mechanical deformations during installation or usage.

The potential applications of circuitry made from the stretchable silicon and integral circuits are vast, such as unusual types of displays, bendable monitors (Figure 1-1), stretchable display screens (Figure 1-2), and surgical gloves with sensors that could read chemical levels in the blood and alert a surgeon to a problem, without impairing the sense of touch (Figure 1-3). Stretchable electronics could allow a prosthetic limb to use pressure or temperature cues to change its shape. More applications can be found, for example, electronic eye cameras (Figure 1-4), intelligent, wireless medical sensors, conformable skin sensors, structural health monitoring devices and so on. Similar types of stiff thin film-compliant substrate system also have many other emerging applications such as micro- and nanoelectromechanical systems, tunable phase optics, force spectroscopy in cells, biocompatible topographic matrices for cell alignment, high precision micro- and nanometrology methods, and pattern formation for micro- and nanofabrication.

Figure 1-1 Evolution of display technology (Crawford, 2005)

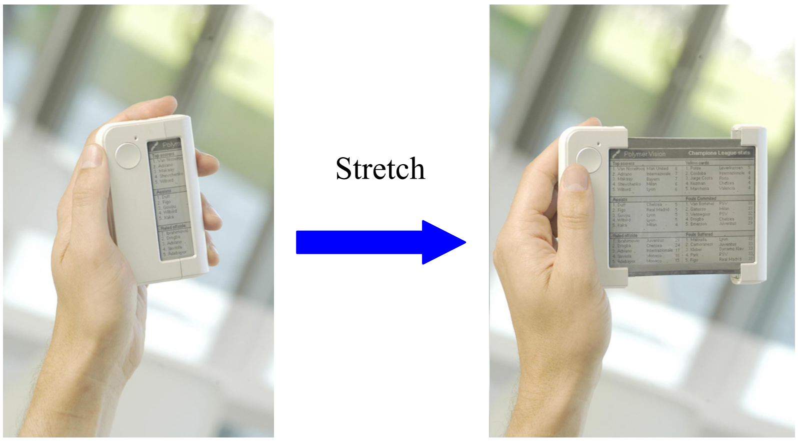

Figure 1-2 World’s first prototype of rollable display by Philips (Sinha, 2005)

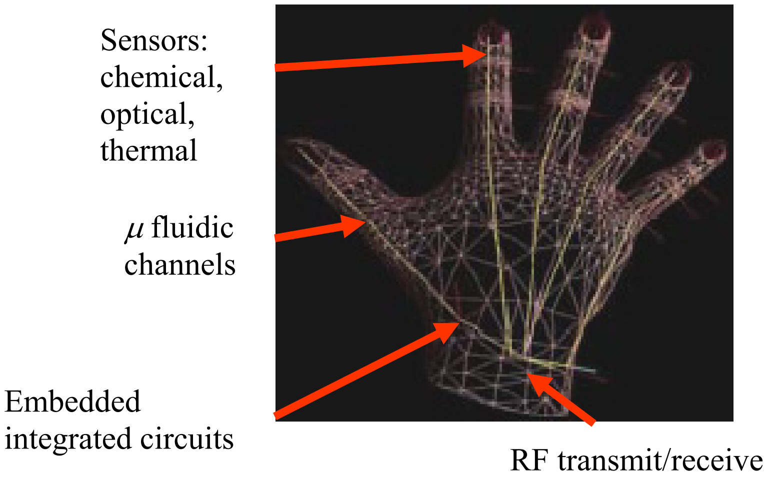

Figure 1-3 Smart micro sensor-based surgical glove (Lumelsky, 2001)

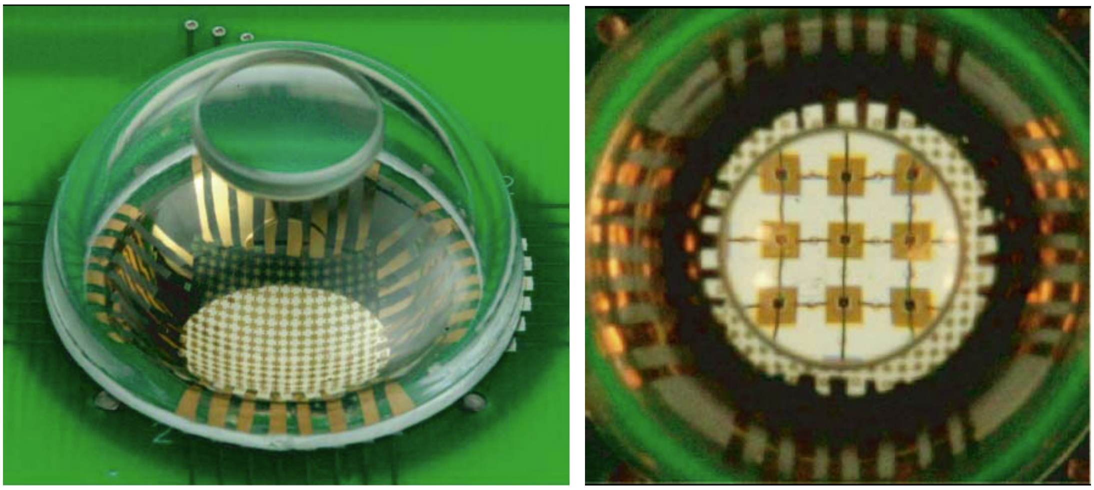

Figure 1-4 Electronic eye camera (Ko, et al., 2008)

A completely different conceptual approach to stretchable electronics emerges from certain research on bendable inorganic electronics (Sun, et al., 2006a; Baca, et al., 2008). Here, desired mechanical properties are realized not through new materials but instead through new structural configurations of established materials. For example, bendability can be achieved in intrinsically brittle materials, such as single-crystalline silicon (Baca, et al., 2008) by implementing the materials in ultrathin formats, nanowires (Duan, et al., 2003), nanoribbons, (Menard, et al., 2004), nanomembranes (Ahn, et al., 2006) and, in some cases, in advanced neutral mechanical plane designs (Kim, et al., 2008). An attractive feature of this strategy is that it leads naturally to systems with improved electrical performance and reliability comparable to those of wafer-scale electronics, far surpassing anything that is possible with known organic active materials. For example, transistor devices with field effect mobilities up to several hundred $cm^2V^{-1}s^{-1}$ in complementary circuits with bendability to radii of curvature as small as 0.05mm can be achieved in this fashion (Ahn, et al., 2006; Kim, et al., 2008). The extension to stretchable electrics is remarkably straightforward: ultrathin material structures formed into 'wavy' or buckled geometries offer stretchability with a physical structure similar to an accordion bellows, without inducing significant strains in the materials themselves (Baca, et al., 2008; Sun, et al., 2006b). This approach has recently been used to create stretchable conductors, transistors, diodes, photodetectors, circuits of various types and even fully integrated systems such as hemispherical electronic eye cameras (Ko, et al., 2008). A separate body of work uses material structures in a different way to yield a similar outcome. Here, open meshes (Someya, et al., 2004) constructed in bendable materials provide large, reversible levels of deformability for strains applied along certain axes, are used in systems such as sensitive robotic skins (Dinyari, et al., 2008). Cantilever-spring structures in silicon, exploit related examples of device level demonstrations of them. Dinyari, et al. (2008) and Hung, et al. (2004) conclude it with some perspectives on future research opportunities.

Stretchable electronics represents a much more challenging class of system, and is of interest for applications where circuits must be wrapped conformally around complex curvilinear shapes or integrated with biological tissues in ways that are impossible using devices that offer only simple bendability. The new type of stretchable electronic system studied here is impressive because it works with single-crystal silicon which is made out of standard, high performance silicon. The fully stretchable form of single-crystal silicon with micron-sized, wave-like geometries can be used to build high-performance electronic devices on rubber substrates. Figure 1-5 schematically illustrates one method for integrating thin films of high quality electronic materials with elastomeric substrates for stretchable electronics. The first step (Figure 1-5a) involves fabrication of thin elements of single crystal silicon or completes integrated devices (transistors, diodes, etc.) by conventional lithographic processing. After this process, the thin film structures are supported by, but not bonded to, the underlying wafer. Contact between the prestrained, compliant substrate and the stiff thin film, leads to bonding between these materials (Figure 1-5b and Figure 1-5c). When the substrate is peeled back, with the film bonded to its surface, and then the prestrain released, causes the substrate to relax back to its unstrained state. This relaxation leads to the spontaneous formation of well-controlled, highly periodic, stretchable wave structures in the thin film (Figure 1-5d) and the region of near the top surface of substrate.

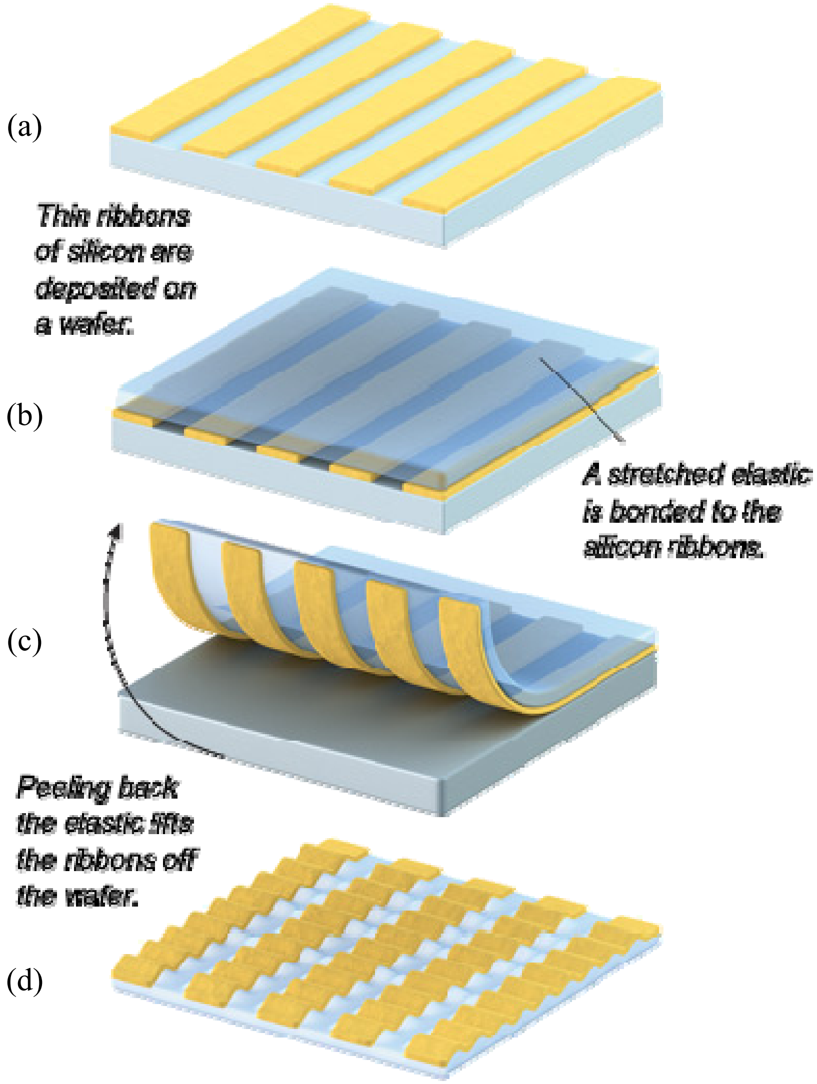

Figure 1-5 Schematic illustration of method for integrating thin films of high quality electronic materials (Greene, K., 2006)

The same method can also be applied to high performance, single crystalline silicon complementary metal oxide semiconductor (Si-CMOS) integrated circuits (ICs) to make them into reversibly foldable and stretchable systems. These systems combine high quality electronic materials, such as aligned arrays of silicon nanoribbons, with ultrathin film and elastomeric substrates exhibiting 'wavy' structural layouts. These approaches are important not only for the Si-CMOS circuits that they enable, but also for their straightforward scalability to much more highly integrated systems with other diverse classes of electronic materials, whose intrinsic brittle, fragile mechanical properties would otherwise preclude their use in such applications.

The most important stage of the fabrication process is to form highly periodic, stretchable wave structures in the thin film. The nonlinear buckling of thin, high modulus plates on compliant supports can be represented as a classical problem in mechanics. Over the last several decades, numerous theoretical and experimental studies of this phenomenon have been performed. Although buckling has historically been viewed as a mechanism for structural failure, the pioneering work of Bowden et al. (1998) showed that the buckling of stiff thin films on compliant substrates can be controlled in micro and nanoscale systems to generate interesting structures with well defined geometries and dimensions in the 100 nm – 100 μm ranges. This has generated numerous theoretical and experimental studies of the buckling of stiff thin film-compliant substrate systems (e.g. Chen and Hutchinson, 2004; Choi et al., 2007; Harrison et al., 2004; Huang, 2005; Huang et al., 2005; Huang and Suo, 2002; Jiang et al., 2007; Khang et al., 2006; Lacour et al., 2004, 2006; Stafford et al., 2004, 2006; Sun et al., 2006a, 2006b). This is because such systems have important applications in stretchable electronics (Choi et al., 2007; Jiang et al., 2007; Khang et al., 2006; Sun et al., 2007a, 2007b; Wagner et al., 2004), micro and nanoelectromechanical systems (MEMS and NEMS) (Fu et al., 2006), tunable phase optics (Harrison et al., 2004; Efimenko et al., 2005), force spectroscopy in cells (Harris et al., 1980), biocompatible topographic matrices for cell alignment (Jiang et al., 2002; Teixeira et al., 2003), high precision micro and nano-metrology methods (Stafford et al., 2004, 2006; Wilder et al., 2006), and pattern formation for micro/nano-fabrication (Bowden et al., 1998, 1999; Huck et al., 2000; Groenewold, J. 2001; Sharp and Jones, 2002; Yoo et al., 2002; Schmid et al., 2003; Moon et al., 2007). In these systems, controlled buckling is realized in the thin films deposited onto prestrained elastomeric substrates by releasing the substrate prestrain. These techniques (Khang. et al., 2006) enable systematic and repeatable studies of the buckling mechanics, to a precision that was not possible in previously studied systems.

In this study, experimental results are presented to demonstrate the fundamental aspects of the buckling process. The observations differ, at both qualitative and quantitative levels, from predictions based on previous mechanical models of this class of stiff thin film-compliant substrate system. Theoretical re-examination of this classical problem leads to a new analytical mechanics theory that provides a coherent and quantitatively accurate description of the mechanics. Numerical studies of wrinkled membranes are performed using the finite element method (FEM). The research work focuses on determining the region(s) affected by wrinkles and the direction of the wrinkles. Numerical simulation is used to compute the geometry of the wrinkles in thin film and PDMS structures of realistic shape and size, and compared with analytical and experimental investigation.

1.2 Research Objectives

The objectives of this research are as follows:

(1) To understand the fabrication mechanism of stretchable and bendable stiff thin film-compliant substrate system, from single crystal silicon ribbons to complete

integrated devices (transistors, diodes, etc) which are made by conventional lithographic processing. The extreme mechanical properties are realized through new structural configurations of materials.

(2) To explain quantitatively the mechanical behavior of the stretchable stiff thin film-compliant substrate system using both classical mechanics theory and numerical analysis techniques. The results are not only applicable to a particular system, like single crystal silicon ribbon on PDMS substrate, but also to the more general case of thin films on compliant supports. The buckled thin film deformation behavior, when subject to external strains, i.e. the post-buckling behavior, is modeled.

(3) To develop analytical and numerical models that can be used to assist the design of systems capable of eliminating the influence of mechanical strains on device performance. The models will, as mechanical design tools, allow engineers to construct stretchable/compressible electronics for different applications.

1.3 Thesis Organization

Chapter One gives an introduction to the background of this research, demonstrates the need of the understanding the mechanical behavior for this underlying technology, and state of the objectives of this study.

Chapter Two describes the design and implementation of stretchable silicon systems and measurement method to emulate the mechanical properties. The wrinkling patterns of the thin film are observed to understand mechanics phenomenon of buckling of stiff thin film-compliant substrate system. The measurement of the amplitude and wavelength (by SEM and ATF) is performed for comparison between analytical and numerical solutions.

Chapter Three expands the implementation of the stretchable silicon system to complete integrated devices and the mechanical and electrical properties are measured. The wrinkling patterns of the integrated circuits are observed and measured using SEM and ATF. The experimental data are used to verify the results of numerical simulation. The electrical properties are measured before and after buckling. The results show the devices can work well after buckling.

Chapter Four commences with basic mechanics theory. The buckling criterion is derived for a thin film on a compliant substrate. The critical strain, amplitude and wavelength, are measured to characterize Young's modulus, Poisson's ratio, and the prestrain of a single-crystal silicon ribbon on a PDMS substrate. Analytical results are used to yield a quantitatively accurate description of the stiff thin film-compliant substrate system mechanism in the fabrication process and to assess its mechanical behavior.

In Chapter Five, the analytical solution of buckling and post-buckling is improved upon based on a finite deformation approach. Buckling theory is established that accounts for finite deformations and geometrical nonlinearities. An accurate solution is obtained for changes in amplitude and wavelength with the prestrain and applied strain of the single-crystal silicon ribbon on a PDMS substrate. The analytical solution is compared with experiment observation.

Chapter Six focuses on two-dimensional numerical analysis: the FEM is used to study thin film buckling on a prestrained substrate, especially, for the case where analytical solutions are not possible, e.g. the edge effect on the end of a silicon ribbon. The numerical solutions reveal the physical phenomenon of buckling and its behavior dependence on prestrain and thin film and substrate properties. The numerical simulation results obtained are verified by both experimental observation and analytical results.

In Chapter Seven, three-dimensional numerical analyses are performed for stretchable integrated circuits. The results obtained by the numerical analysis capture the buckling pattern well. The stress and strain distributions are studied for the buckling of complex integrated circuits on a prestrained substrate.

Finally conclusions and suggestions for further work are provided in Chapter Eight.

Chapter Two

Experimental Observation and Measurement for Single Crystal Silicon

The research group at the University of Illinois at Urbana-Champaign (UIUC) reported a new approach to fabricate a stretchable silicon system (Khang, et al., 2006). The stretchability of this system is achieved directly in thin films of high-quality, single crystal silicon that have micrometer-scale, periodic, “wave”-like geometries. Instead of potentially destructive deformation in the materials themselves, these structures could sustain large compressive and tensile strains through changes in the wave amplitude and wavelength. Integrating such stretchable wavy silicon elements with dielectrics, patterns of dopants, and thin metal films leads to high-performance, stretchable electronic devices. The work reported in Chapter Two and Three is derived from the collaboration work conducted when the author underwent a research attachment at the Department of Materials Science and Engineering and the Department of Mechanical Science and Engineering at UIUC in 2007.

2.1 Materials Preparation and Fabrication Methods for Single Crystal Silicon

2.1.1 Single Crystal Silicon and Mother Wafer Sample Preparation

The silicon-on-insulator (SOI) wafers consist of three layers (Figure 2-1). There are single crystal silicon, SiO_2 and silicon substrates. In the current studies, a

SOI wafer of silicon (thickness ~100 nm) and SiO_2 (thickness 1.5–3.0 μm) are used on silicon substrates. The top single crystal silicon layer has a resistivity between 5–20 Ωcm, doped with boron ($p-$type) or phosphorous ($n-$type). The top silicon of these SOI wafers is patterned with photolithoresist (AZ 5214 photoresist, Karl Suss MJB-3 contact mask aligner) and reactive ion etched (RIE) to define the silicon ribbons of ~50 μm wide and 15mm long (PlasmaTherm RIE, SF6 40sccm, 50mTorr, 100W). The SiO_2 layer is removed by undercut etching in HF (49%); the etching time is mainly dependent on the width of the silicon ribbons. The lateral etch rate is typically 2–3 μm/min. Slabs of poly(dimethylsiloxane) (PDMS) elastomer (Sylgard 184, Dow Corning) are prepared by mixing the base and curing agent in a 10:1 weight ratio and curing at 70 ℃ for >2hrs or at room temperature for >12 hrs..

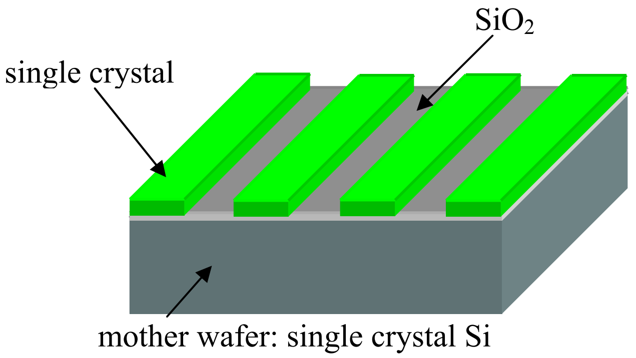

(a) Three layers are strongly bonded

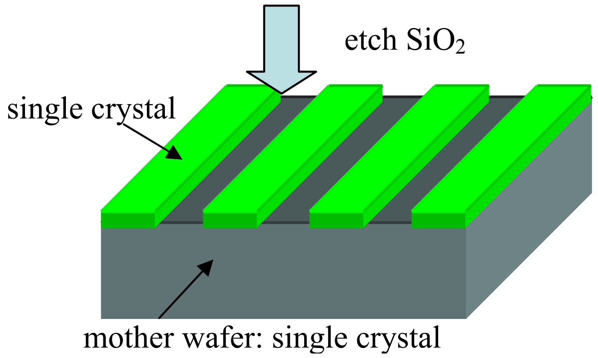

(b) Single crystal silicon ribbons placed upon the mother wafer

Figure 2-1 Single crystal silicon on mother wafer

2.1.2 Fabrication Sequence for Wavy, Single Crystal Silicon

Figure 2-2 presents the fabrication sequence for wavy, single-crystal silicon ribbons on elastomeric (rubber) substrates (Khang, et al., 2006). The first step (Figure 2-1a) involves fabrication of thin elements of single crystal silicon or completes integrated devices (transistors, diodes, etc.) by conventional lithographic processing, followed by etching to remove the exposed parts of the top silicon. Removing the resist with acetone and then etching the buried SiO_2 layer with concentrated hydrofluoric acid releases the ribbons from the underlying silicon substrate. The ends of the ribbons connect to the wafer to prevent them from washing away in the etchant. The widths (5–50 mm) and lengths (~15mm) of the resist lines define the dimensions of the ribbons. The thickness of the top Silicon (20–320 nm) on the SOI wafers defines the ribbon thickness.

In the next step (Figure 2-2b), the ribbon structures are supported by, but not bonded to, the underlying wafer. A flat elastomeric substrate poly(dimethylsiloxane) (PDMS), 1–3 mm thick) is elastically stretched and then brought into conformal contact with the ribbons. Then, peeling the PDMS away lifts the ribbons off the wafer and leaves them adhered to the PDMS surface, and then releasing the prestrain, causes the PDMS to relax back to its unstrained state. The relaxation leads to the spontaneous formation of well-controlled, highly periodic, stretchable wavy structures in the ribbons (Figure 2-2c).

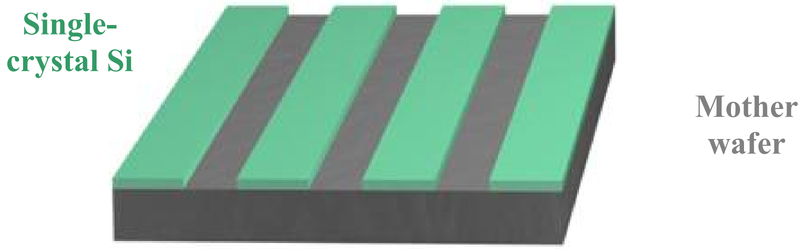

(a) Fabrication of single crystal silicon thin ribbon device elements

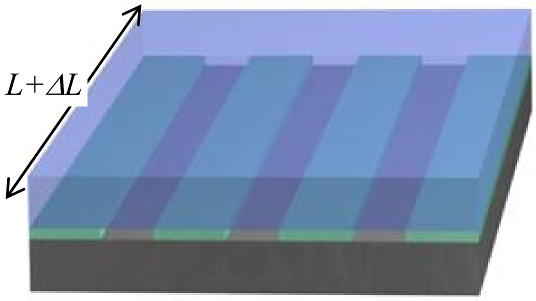

(b) Elements bonded to prestrained elastomeric substrate

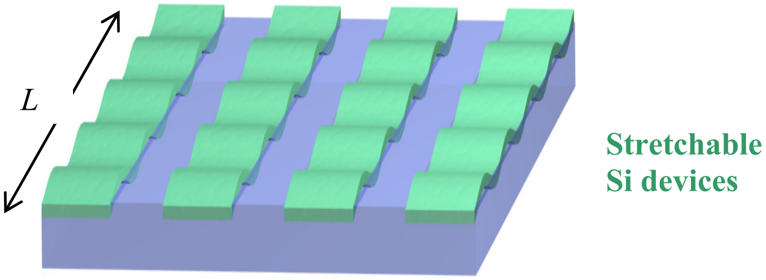

(c) PDMS peeled back, flipped over and shrunk.

Figure 2-2 Schematic illustration of process for building stretchable single crystal silicon devices on elastomeric substrates.

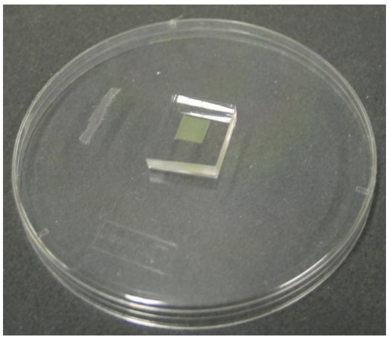

Figure 2-3 Stretchable single-crystal silicon devices on elastomeric substrates

These flat slabs of PDMS (thicknesses of ~3 mm) are brought into conformal contact with the silicon on the etched SOI wafer to generate the wavy structures. Any method that creates controlled expansion of the PDMS substrate prior to this contact followed by contraction after removal from the wafer can be used. There are three different techniques. The first technique is using mechanical rolling of PDMS substrate after contact with the SOI substrate, to generate the prestrain. Although the wavy structures could be made in this manner, they tended to have non-uniform wave periods and amplitudes. In the second technique, heating the PDMS substrate (coefficient of thermal expansion $\alpha_s = 3.1\times10^4$ K^{-1}) to temperatures of between 30ºC and 180ºC before contact and then cooling it after removal from the SOI, generates wavy silicon structures with excellent uniformity over large areas, in a highly reproducible fashion: with this technique, the prestrain level can be controlled in PDMS substrate very accurately by changing the temperature. The third technique is that PDMS substrate is stretched using mechanical stretching stages before contact with the SOI, then release physically it after mother wafer is removed. The mechanical stretching stage is shown in Figure 2-4. This method, like the thermal approach, enables good uniformity and reproducibility, but it is more difficult to finely tune the pre-strain level than the thermal method.

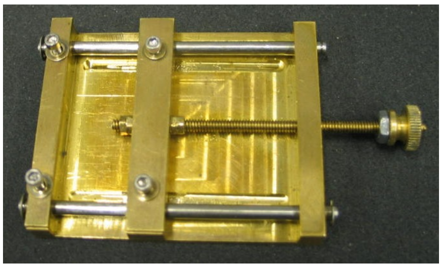

Figure 2-4 Mechanical stretching stage

For devices such as $p-n$ junction diodes and transistors, electron beam evaporated (Temescal BJD1800) and photolithographically patterned (through etching or liftoff) metal layers (Al, Cr, Au) are used as contacts and gate electrodes. Spin-on-dopants (SOD) (B-75X, Honeywell, USA for $p-$type; P509, Filmtronics, USA for $n-$type) are used to dope the silicon ribbons. The SOD materials are first spin-coated (4000 rpm, 20 s) onto pre-patterned SOI wafers. A silicon dioxide layer (of width ~300 nm) prepared by plasma-enhanced chemical vapor deposition (PECVD) (PlasmaTherm) is used as a mask for the SOD. After heating at 950ºC for 10 s, both the SOD and masking layer on the SOI wafer are etched away using 6:1 buffered oxide etchant (BOE). For the transistor devices, thermally grown (1100ºC, 10–20 min. dry oxidation with high purity oxygen flow in a furnace to thicknesses between 25 nm and 45 nm) silicon dioxide provides the gate dielectric.

After completing all device processing steps on the SOI substrate, the silicon ribbons (typically 50 μm wide and 15 mm long) with integrated device structures are covered by a photoresist (AZ5214 or Shipley S1818) to protect the device layer during HF etching of the underlying SiO_2. After removing the photoresist layer by oxygen plasma, a flat PDMS (70ºC, for > 4 hrs) slab without any prestrain is used to remove the ribbon devices from the SOI substrate, in a flat geometry. A slab of partially cured PDMS (>12 hrs at room temperature after mixing the base and curing agent) is then brought into contact with the silicon ribbon device on the fully cured PDMS slab. Completing the curing of the partially cured PDMS (by heating at 70ºC), followed by removal of this slab, and transferred the devices from the first PDMS slab to this new PDMS substrate. The shrinkage associated with cooling down to room temperature creates a prestrain such that the process of removal and release creates the wavy devices, with electrodes exposed for probing.

2.2 Pattern Observation and Measurement

2.2.1 Pattern Observation

Releasing the prestrain in the PDMS leads to surface deformations (wrinkling) that cause well-defined waves to form in the silicon and the PDMS surface (Figure 2-5) (Khang, et al., 2006). The optical images at different shrink stages are shown in Figure 2-6. These images clearly show that the overall wrinkle pattern of single crystal silicon ribbons range from flat strip to “wave”-like. The single crystal silicon ribbons start to buckle when its compression strain reaches the critical strain level. There are two types of buckling processes: buckling that starts along the whole length of the ribbon (Figure 2-6a) and buckling that starts from the two opposite ends of the ribbon (Figure 2-6b). The final wave pattern is the same, however, regardless of the type of buckling.

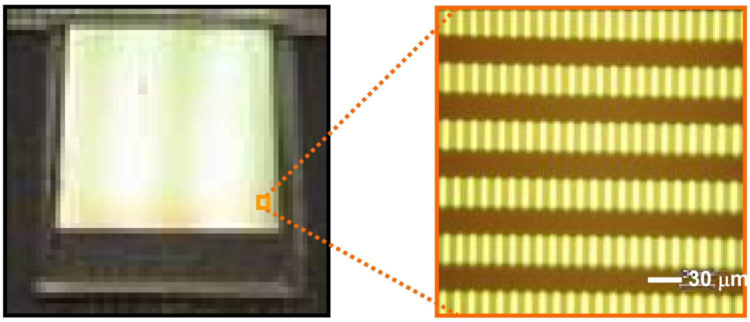

Figure 2-5 Surface deformations

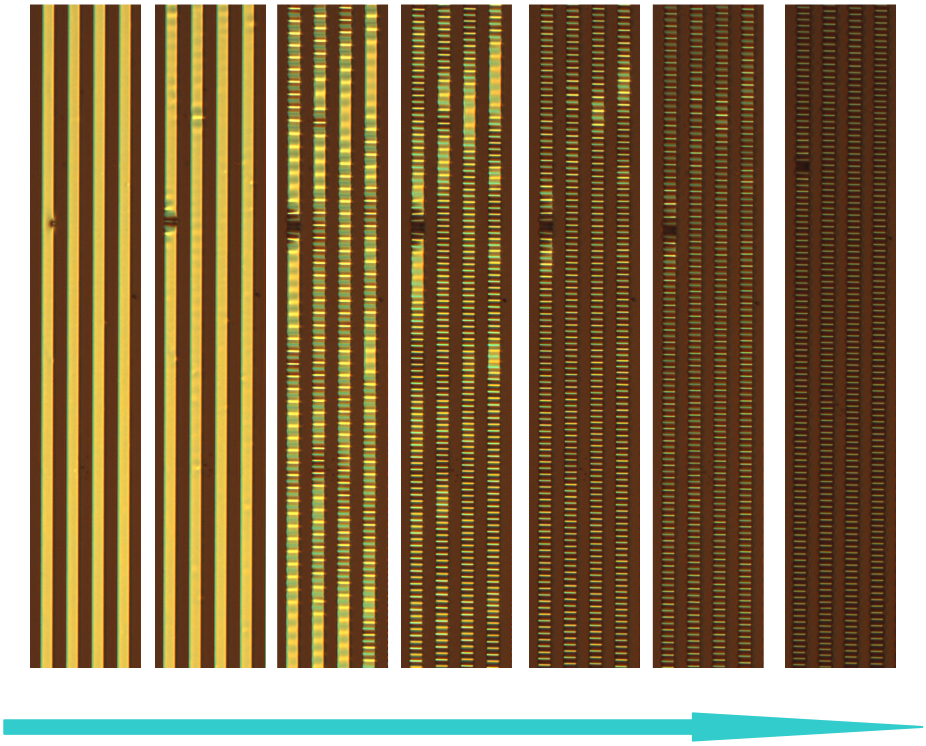

(a) Buckling starting along whole length of silicon ribbon

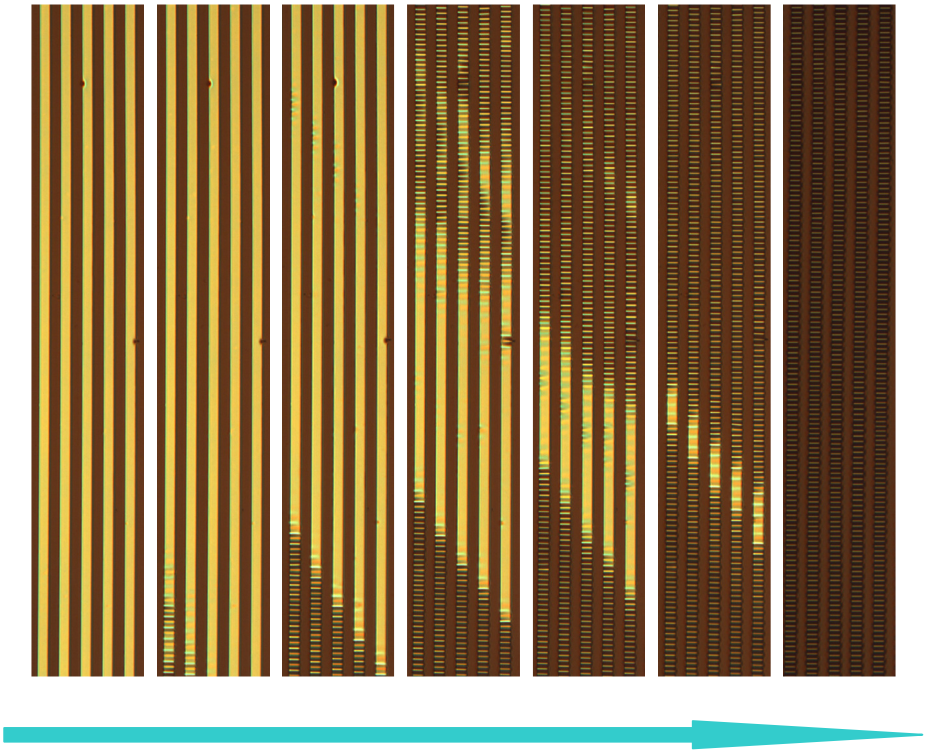

(b) Buckling starting from two opposite ends of silicon ribbon

Figure 2-6 Optical image of single crystal silicon ribbons at different shrink stage

Figures 2-7 (a) to (c) are close-up views of wrinkle patterns of single crystal silicon ribbons using a scanning electron micrograph (SEM). The silicon ribbons are formed as sinusoidal waves. In this 45º tilted view, the dark area under the silicon wave peak is partial separation of silicon ribbons and PDMS. Silicon ribbons and PDMS upon magnification and brightness changing, PDMS is still under the silicon. Although there is partial separation of silicon, no complete gap or separation along both sides of the silicon ribbon at wave peaks is evident (See Figure 2-8).

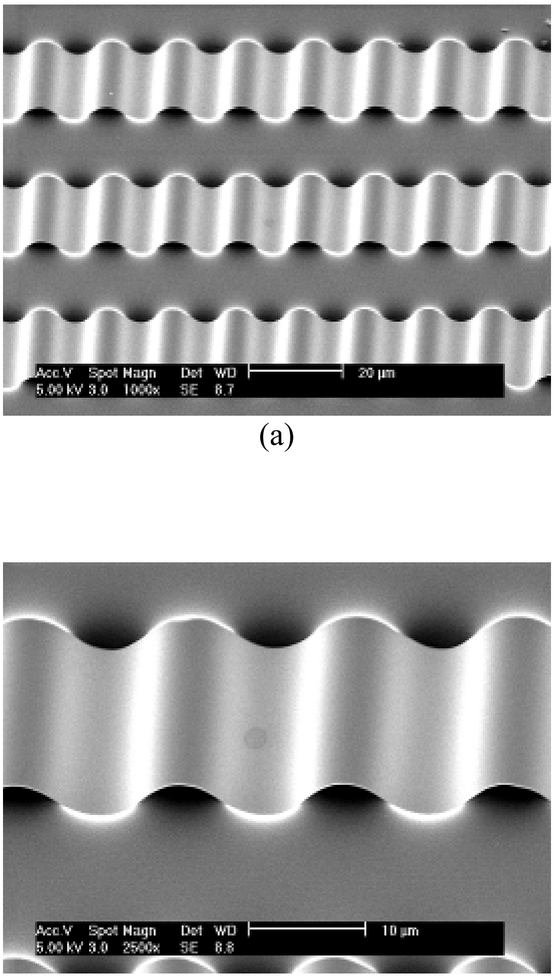

(a)

(b)

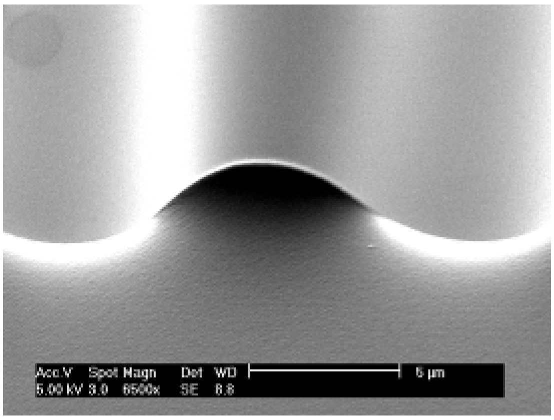

(c)

Figure 2-7 45º tilted view of wrinkled single crystal silicon ribbons using SEM

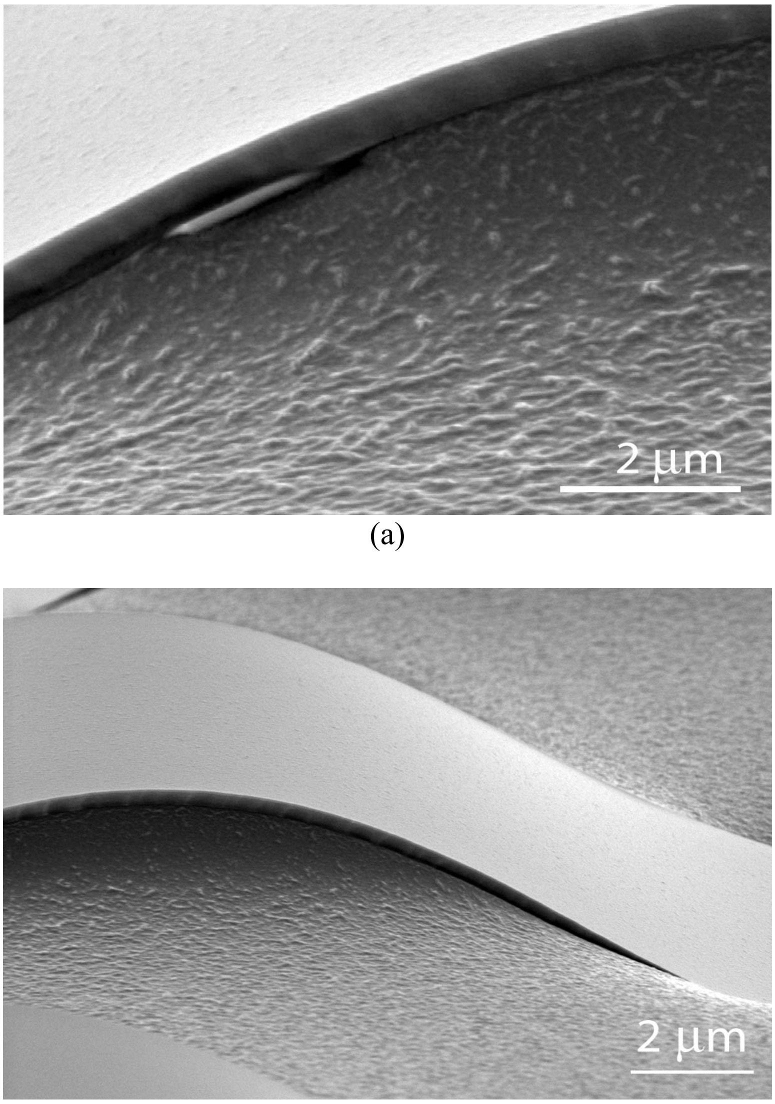

(a)

(b)

Figure 2-8 No debonding between silicon ribbon and PDMS at wave peaks

2.2.2 Measurements

Atomic force microscopy (AFM) (DI-3100, Veeco) is used to measure the wave properties (wavelength and amplitude) precisely. From the acquired images, the sectional profiles along the wavy silicon have been measured and analyzed statistically. The mechanical stretching stage is used, together with AFM and a semiconductor parameter analyzer (Agilent, 5155C) to measure the mechanical and electrical responses of wavy Si/PDMS. Raman measurements are performed with a Jobin Yvon HR 800 spectrometric analyzer using 632.8 nm light from a He-Ne laser. The Raman spectrum is measured at 1μm intervals along the wavy silicon, with a focus adjusted to maintain the focus position on the top surface of the silicon, based on the silicon Raman peak intensity. The measured spectrum is fitted by Lorentzian functions (or call Cauchy distribution) to locate the peak wave number. Due to the slight dependence of the peak wave numbers on the focal position of the microscope, the Raman results only provide qualitative insights into the stress distributions.

The relief profiles are sinusoidal (Figure 2-9), with periodicities between 5 and 50 mm and amplitudes between 100 nm and 1.5 mm, depending on the thickness of the silicon and the level of prestrain in the PDMS (Khang, et al., 2006). . The periods and amplitudes of the waves, for a given system, are uniform to within ~5% over large areas (several square centimeters). The flat morphology of the PDMS between the ribbons and the absence of correlated phases in the waves of adjacent ribbons suggest that the ribbons are not strongly mechanically coupled. Figure 2-10 shows micro-Raman measurements of the silicon peak, measured as a function of distance along one of the wavy ribbons (Khang, et al., 2006). . The results provide the insight view of the strain distributions of the wavy ribbons.

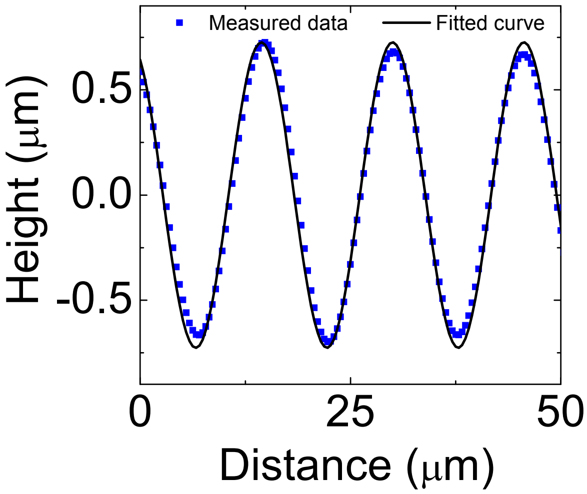

Figure 2-9 Sinusoidal profiles of wavy silicon ribbons

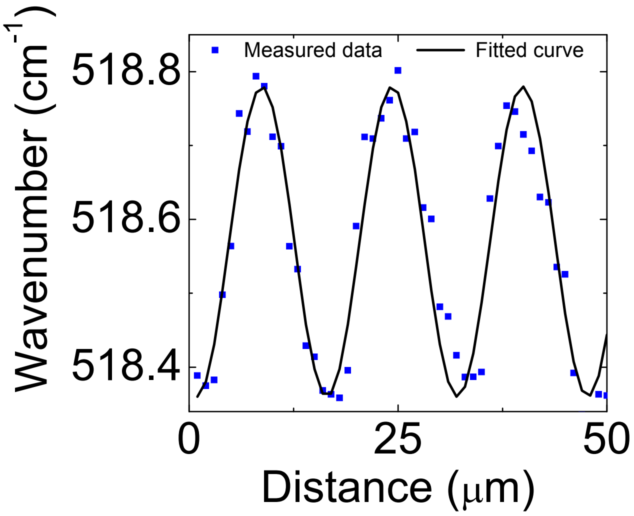

Figure 2-10 Micro-Raman measurements of silicon peak

2.2.3 Calculation of Contour Length and Silicon Ribbon Strain

One may assume from the experimental results that the shape of wavy silicon ribbon could be represented with simple sine functions, i.e. $y = A\sin(kx)$ $(k = 2\pi/\lambda)$ where A is the amplitude, λ is the wavelength. The contour length $\lambda_{contour}$ can then be calculated as $\lambda_{contour} = \int_0^{\lambda} \sqrt{1+y'^2}\,dx$ (Khang, et al., 2006). The ribbon strain of wavy silicon is calculated using $\varepsilon_{Si} = \frac{|\lambda - \lambda_{contour}|}{\lambda}$. The peak silicon ribbon strains occur at the peaks and troughs of the waves, and can be calculated using $\varepsilon_{Si}^{peak} = \frac{t}{2R_c}$, where t is the silicon ribbon thickness, and $R_c = -\frac{1}{y''}\Big|_{x=\pm\left[\frac{(2n-1)\pi}{2h}\right]}$ is the radius of curvature at the peak or trough, where n is an integer and y'' s the second derivative of y with respect to x. Using the sine function approximation to the actual shape, the substrate peak strain is given by $\varepsilon_{Si}^{peak} = \frac{2\pi^2 Ah}{\lambda^2}$.

2.3 Device Characterization

2.3.1 Stretchability of Wavy Silicon Ribbons

It is important to understand the electrical performance response of wavy structures on stretchable electronic devices under compressive and tensile strains. To reveal the mechanics of this process, stretching and compressing strains are applied to the elastomeric substrate after fabrication. The geometries of wavy silicon ribbons are measured by AFM, when the compressive or tensile force is applied on the PDMS. Both forces are parallel to the long dimension of the ribbons and cause strains both along the ribbons and perpendicular to them due to the Poisson's effect. The wavy silicon ribbon's pattern is changed according to strains along the ribbons. Figure 2-11 shows the optical image of a wavy silicon ribbon's surface under compressed, unperturbed, and tensioned states (Khang, et al., 2006). The three-dimensional height images and surface profiles, captured by AFM, are shown in Figure 2-12a (Khang, et al., 2006). It may be observed from these figures, that the silicon ribbons maintain their sinusoidal shapes (Figure 2-12b) during deformation, in which approximately half of the wave structure lies beneath the unperturbed position of the PDMS surface, as defined by the regions between the ribbons (Khang, et al., 2006). Figure 2-12b shows the wavelength and amplitude for compressive (negative) and tensile (positive) applied strains relative to the unperturbed state (zero). The data correspond to averaged AFM measurements collected from a large number (950) of ribbons per point. The applied strains are determined from the measured end-to-end dimensional changes of the PDMS substrate.

Direct surface measurements by AFM, as well as contour integrals evaluated from the sinusoidal wave shapes, show that the strains are equal to the ribbons strains (Figure 2-13) for the cases examined here. The symbols of red dot with error bar correspond to strains computed by numerical integration of the contour length, using wavelengths and amplitudes extracted from equations that describe the buckling process. The symbols of black dot with error bar correspond to strains measured from the ratio of surface area to horizontal distance in AFM surface profile along the wavy silicon ribbons. The small-amplitude (< 5 nm) waves that persist at tensile strains larger than the prestrain minus the critical strain might result from slight slippage of the silicon during the initial buckling process. The computed peak silicon strains and ribbon strains in this small- (or zero-) amplitude regime underestimate the actual values. The results indicate two physically different responses of the wavy ribbons to applied strain. One is that the wavelength does not change appreciably with applied tensile strain, which is consistent with post-buckling mechanics. Instead, the wavelength changes in amplitude to accommodate for the strain. In this regime, the silicon strain decreases as the PDMS is stretched; it reaches ~0% when the applied strain equals the prestrain.

Another is that the wavelengths decrease and amplitudes increase with increasing applied compressive strain. This mechanical response is similar to that of an accordion bellows shape, which is qualitatively different from the behavior in tension. During compression, the silicon strain increases with the applied strain, due to the decreasing radii of curvature at the wave peaks and troughs. The rates of increase and magnitudes of the silicon strains are, however, both much lower than the ribbon strains, as shown in Figure 2-12. This mechanical behaviour enables stretchability.

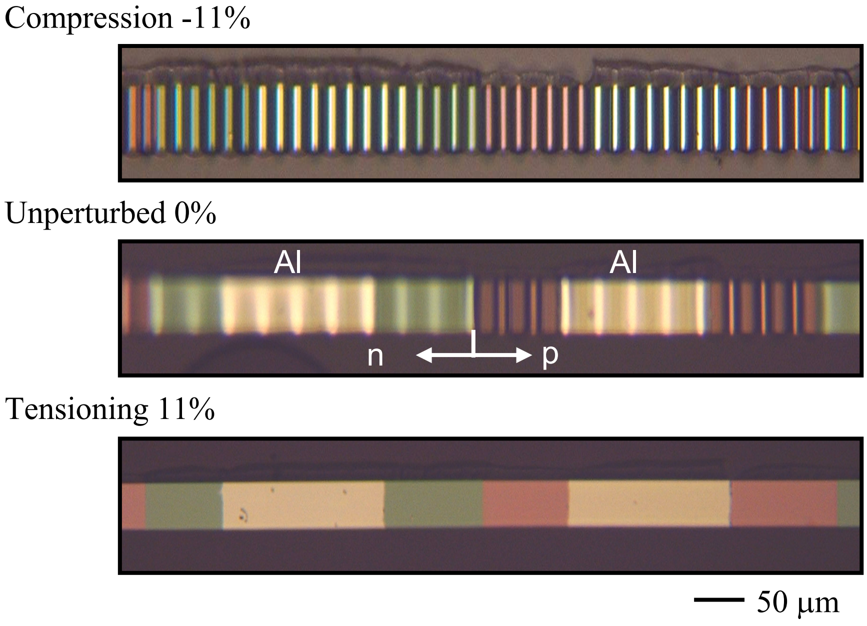

Figure 2-11 Optical image of stretchable single crystal silicon $p-n$ diode on PDMS substrate under applied strain

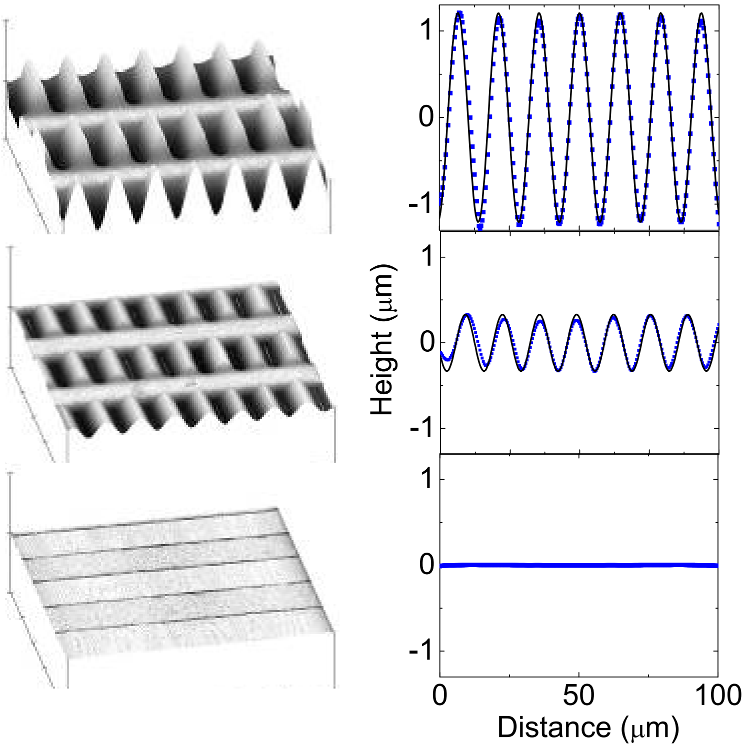

(a) Profile of silicon ribbon (b) Wavelength and amplitude

Figure 2-12 AFM images and relief profiles of wavy silicon ribbons.

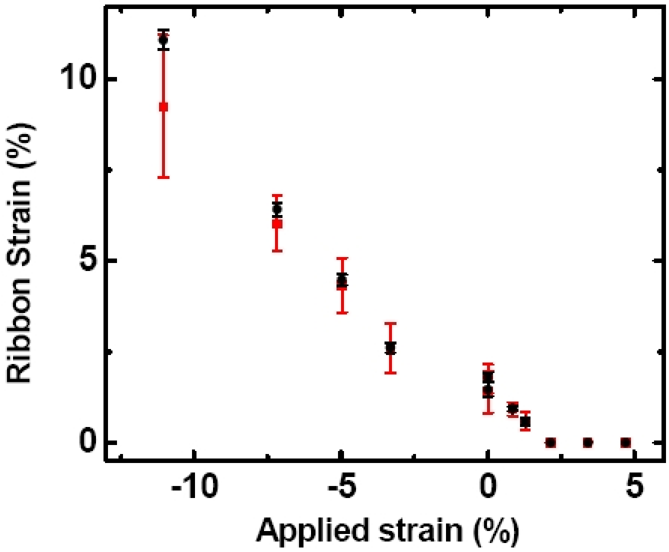

Figure 2-13 Silicon ribbon strain as function of applied strain.

2.3.2 Electric Performance of Wavy Silicon Ribbons

Wavy silicon does not affect the electric performance, such as current density vs. bias voltage. A semiconductor parameter analyzer (Agilent, 5155C) and a conventional probing station are used for the electrical characterization of the wavy $p-n$-junction diodes and transistors (Khang, et al., 2006). The light response of a $p-n$-diode is measured under an illumination intensity of ~1W/cm^2, as measured by an optical power meter (Ophir Optronics, Inc., Laser Power Meter AN/2). The mechanical stretching stages are used to measure the devices during and after tension and compression. As a means to explore the reversibility of the process, three different $p-n$-diodes are measured before and after ~100 cycles of compression (to ~5% strain), tension (to ~15% strain) and release, in ambient light. Thus these wavy transistors can be reversibly stretched and compressed without damaging the devices or substantially altering their electrical properties (Figure 2-14). Hence, there is great potential to make a new type of stretchable electric device using wavy geometries.

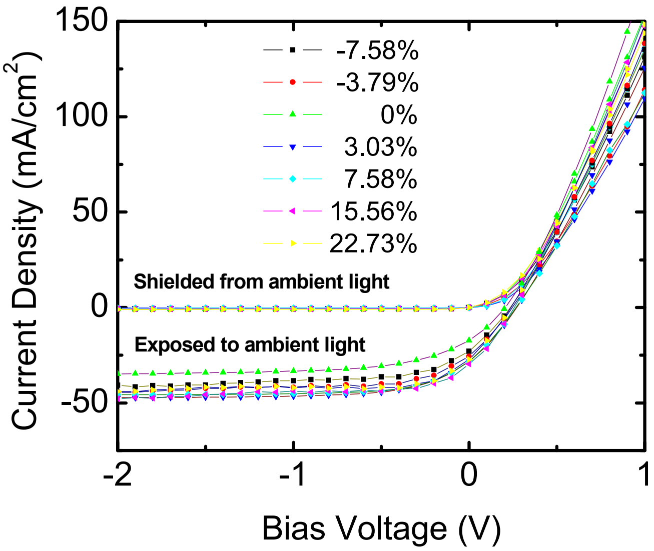

Figure 2-14 Current density vs. bias voltage for stretchable single crystal silicon $p-n$ diode at different applied strains

Chapter Three

Experimental Observation and Measurement for Integrated Circuits

The process of stretchable and foldable silicon integrated circuit fabrication to ensure high functional performance can only occur provided that single crystal silicon ribbon is adequately stretchable. The fully stretchable form of ‘wavy’ structural configurations in silicon complementary logic gates, ring oscillators and differential amplifiers of micron size, etc can be used to build high-performance electronic devices on rubber substrates. The fabrication process for ultrathin CMOS circuits exploits enables extreme levels of bendability and fully reversible stretchability/compressibility of the silicon nanoribbons.

The key steps of the fabrication process in forming ultrathin, foldable and stretchable circuits are discussed, and the measurement of material properties and deformation patterns is presented in this chapter.

3.1 Materials Preparation and Fabrication Methods for Integrated Circuits

The high performance, single crystalline silicon complementary metal oxide semiconductor (Si-CMOS) integrated circuits (ICs) are reversibly foldable and stretchable (Kim, et al., 2008). These systems combine high quality electronic materials, such as aligned arrays of silicon nanoribbons, with ultrathin and elastomeric substrates, in multilayer neutral mechanical plane designs and with ‘wavy’ structural layouts. High performance *n* and *p* channel metal oxide semiconductor field effect transistors (MOSFETs), CMOS logic gates, ring oscillators and differential amplifiers, all with electrical properties equal to analogous systems built on conventional silicon-on-insulator (SOI) wafers, demonstrate this fabricated concepts. Single crystalline silicon provides excellent electronic properties, including high electron and hole mobilities. Commodity bulk silicon wafers (Mack, et al., 2006) can be used instead of SOI, to reduce the cost of the systems. Vacuum evaporated materials such as nanocrystalline Si (Lee, et al., 2006), which also enable high performance, might offer further advantages in cost reduction of the fabrication process. Similar approaches to stretchable and foldable integrated circuits reported here can be used with these and other related classes of materials. Automated stages specially designed for transfer printing, enable multilayer registration with ~2 μm accuracy (Ahn, et al., 2006). These approaches are important not only for the Si-CMOS circuits whose multilayer registration they enable, but also for their straightforward scalability to much more highly integrated systems with other diverse classes of electronic materials, whose intrinsic brittle, fragile mechanical properties would otherwise preclude their use in such applications.

Figure 3-1 gives an overview of the fabrication process for ultrathin CMOS circuits that exploit silicon nanoribbons, and enable extreme levels of bendability or fully reversible stretchability/compressibility. There are two major steps in the process: (1) fabricating (ICs) and (2) forming foldable and stretchable circuits system. A cross-sectional view of typical integrated circuits is shown in Figure 3-2.

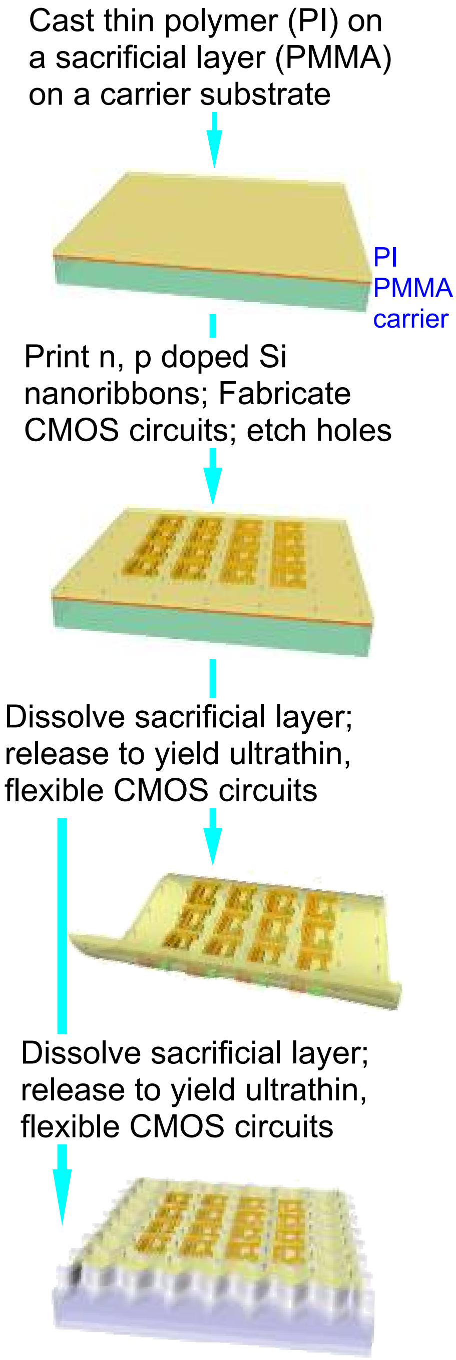

Figure 3-1 Overview of Fabrication Process

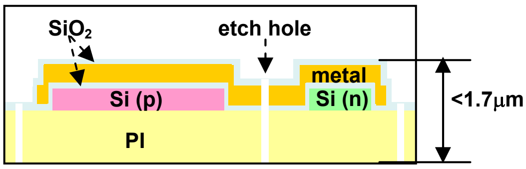

Figure 3-2 Cross-sectional view of ICs

3.1.1 Integrated Circuits Sample Fabrication

The transistors considered in this study used in the experimental work employed doped silicon nanoribbons for the semiconductor. The fabrication involves the following three steps (illustrates in Figure 3-3).

(1) First, an $n-$type silicon-on-insulator (SOI) wafer (Si (260 nm) / SiO_2 (1000 nm) / Si with doping of 2.7-5.2×10^{15} cm^3, SOITEC, France) is lightly doped with boron via a spin-on-dopant (B153, Filmtronics, USA) at a diffusion temperature of approximately 550~600 °C to define $p-$wells. SiO_2 (~ 300 nm) formed by plasma enhanced chemical vapor deposition (PECVD) was used as a diffusion mask. For this lithography procedure, AZ5214 photoresist (Clariant, USA) was spin coated at 3000 rpm for 30 sec. Next, highly doped $p-$type source/drain electrodes are formed beside the $p-$wells using the same boron spin-on-dopant, this time at a temperature of 1000~1050°C. Then, heavily doped $n-$type source and drain regions are defined inside the $p-$well with phosphorous spin-on-dopant (P509, Filmtronics, USA) at 950°C by using the same diffusion mask and photolithography procedure.

(2) After doping, the desired structure of Si ribbons is defined by lithographic and dry etching steps with a SF_6 plasma (Plasmatherm RIE system, 40 Sccm SF_6 flow with a chamber pressure of 50 mTorr, 100 W rf power for 30 s.). The underlying SiO_2 is removed by concentrated (49%) HF to release thin semiconductor ribbons. These released Si ribbons can then be transferred in organized arrays from the SOI wafer to the carrier wafer coated with thin layers of PMMA (MicroChem,

USA) (~100 nm, spin coat at 3000 rpm for 30 s) and poly(amic acid), precursor of PI (Polyimide) (~1.2 μm, spin coat at 4000 rpm for 60 sec) using an elastomeric stamp as the transfer element.

(3) After the complete curing of the PI at 300°C for 1-1.5 h, the active regions of the devices are isolated by SF_6 plasma and a thin gate oxide of SiO_2 (~50 nm) is deposited with PECVD. The PECVD SiO_2 on the source/drain contact regions is then removed by RIE or buffered oxide etchant through openings in a layer of photoresist pattern by photolithography. Cr/Au (~5 nm/~145 nm) for the source, drain and gate electrodes and metal (chromium–gold–chromium) interconnects are deposited with e-beam evaporation and then are patterned by photolithography and wet etching. A uniform layer SiO_2 (~50 nm) is then deposited by PECVD to form a passivation layer. Etching away this layer to produce contact windows, which enable electrical contact with devices and circuits, completes the fabrication process.

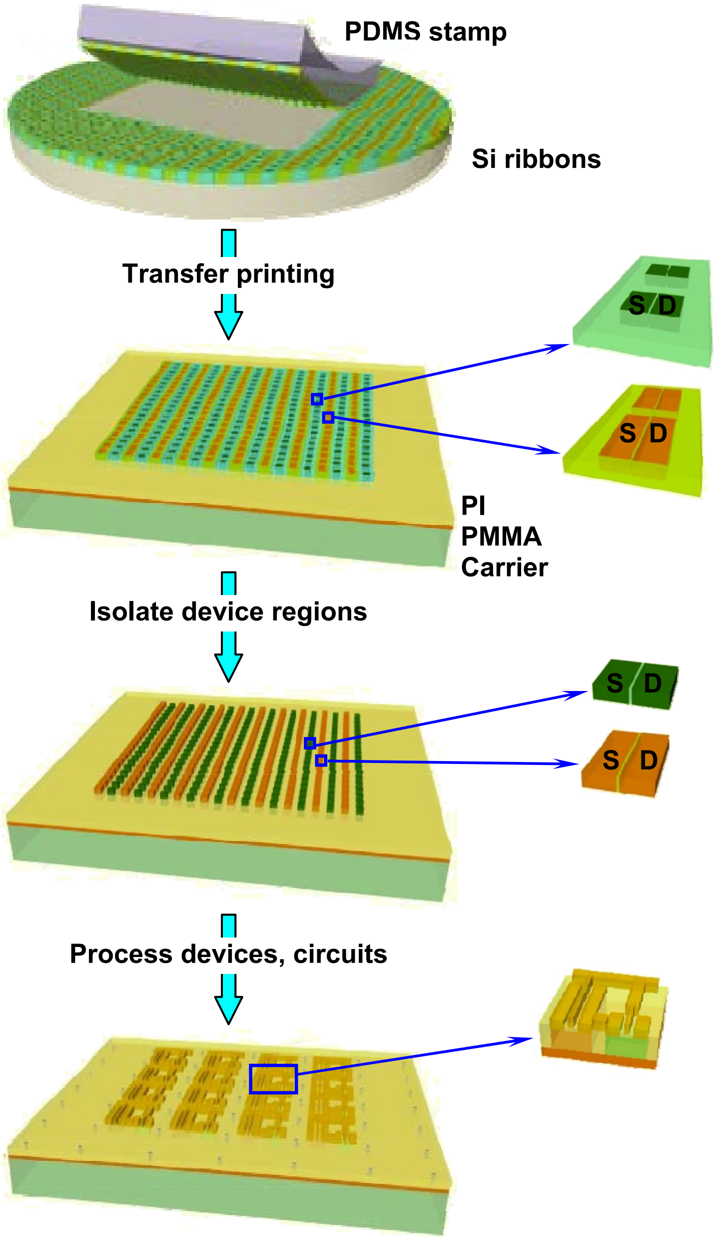

Figure 3-3 Schematic diagram for circuit preparation procedures

3.1.2 Fabrication Sequence for Ultrathin, Foldable and Stretchable Circuits - Si-CMOS inverters

Figure 3-4 schematically summarizes the steps for forming ultrathin, foldable and stretchable circuits. The procedure is almost the same as the fabrication methods for single crystalline silicon, but thin film constitutes the multi-layers of the ICs rather than single crystalline silicon. The procedure begins with spin-casting a sacrificial layer of poly(methylmethacrylate) (PMMA) (~100 nm) followed by a thin, substrate layer of polyimide (PI) (~1.2 μm) on a Si wafer that serves as a temporary carrier. A transfer printing process with a poly(dimethylsiloxane) (PDMS) stamp (Menard, et al., 2004; Meitl, et al., 2006) delivers to the surface of the PI organized arrays of n and p doped Si nanoribbons (see Figure 3-5) with integrated contacts, separately formed from $n-$type source wafers. Automated stages specially designed for this printing process enable multilayer registration with ~2 mm accuracy (Ahn, et al., 2006). Depositing and patterning SiO_2 (~50 nm) for gate dielectrics and interconnect crossovers, and the use of Cr/Au (5/145 nm) for the source, drain and gate electrodes and interconnects, yield fully integrated Si-CMOS circuits with performance comparable to similar systems formed on SOI wafers. Figure 3-6 shows an image of an array of Si-CMOS inverters and isolated n and p channel MOSFETs ($n-$MOSFETs and $p-$MOSFETs, respectively) formed in this manner, still residing on the carrier substrate.

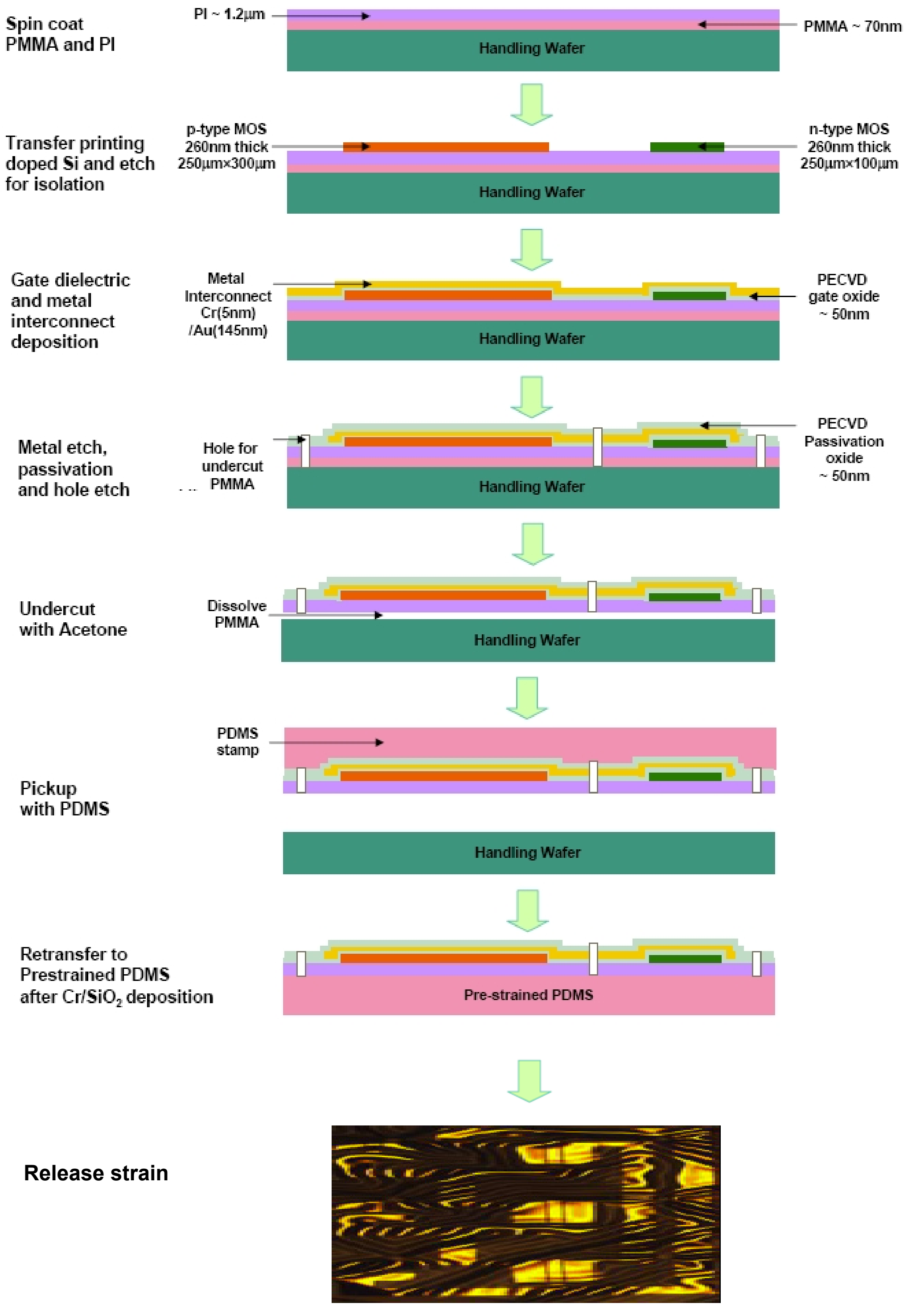

Figure 3-4 Fabrication Schematics of Ultrathin, Foldable and Stretchable Circuits

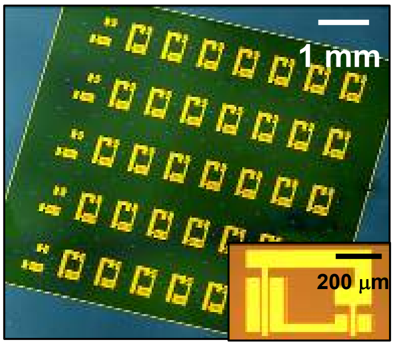

Figure 3-5 Circuits on carrier wafer

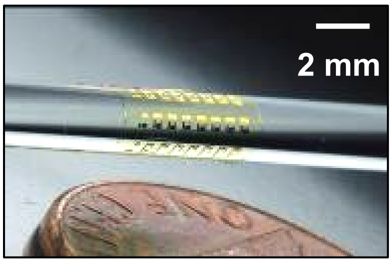

Figure 3-6 Ultrathin device on thin rod coated with PDMS

In the next step of the fabrication process, reactive ion etching is used to form a square array of small holes (~50 μm diameters, separated by 800 μm) that extend through the nonfunctional regions of the circuits and the thin PI layer, into the underlying PMMA. Immersion in acetone dissolves the PMMA by flow of solvent through the etch holes to release ultrathin, flexible circuits in a manner that does not degrade the properties of the devices. These systems can be implemented as flexible, free-standing sheets, or they can be integrated in wavy layouts on elastomeric substrates, to provide fully reversible stretchability/compressibility (Figure 3-7).

The fabrication continues with removal of the ultrathin circuits from the carrier substrate using a PDMS stamp, evaporating a thin layer of Cr/SiO_2 (3/30 nm) onto the exposed PI surface (i.e. the surface that was in contact with the PMMA), and then generating –OH groups on the surfaces of the SiO_2 and a biaxially prestrained

PDMS substrate ($\varepsilon_{pre} = \varepsilon_{xx} = \varepsilon_{yy}$, where the x and y coordinates lie in the plane of the circuit) by exposure to ozone induced with an ultraviolet lamp.

Transfer printing the circuit onto the PDMS substrate, followed by mild heating creates covalent linkages to form strong mechanical bonding between the Si CMOS/PI/Cr/SiO_2 and the PDMS. Relaxing the prestrain induces compressive forces on the circuits that lead to the formation of complex ‘wavy’ patterns of relief via a nonlinear buckling process. Circuits in this geometry offer fully reversible stretchability/compressibility without inducing substantial strains in the circuit materials themselves. Instead, the amplitudes and periods of the wave patterns change to accommodate applied strains ($\varepsilon_{applied}$, in any direction in the plane of the circuit), with physical behaviour similar to an accordion bellows (Jiang, et al., 2007). Figure 3-8 presents an optical image of a wavy Si-CMOS circuit on PDMS, formed with a biaxial prestrain of ~5.6%. The thickness of the PDMS can be selected to achieve any practical level of flexural rigidity, without compromising its stretchability.

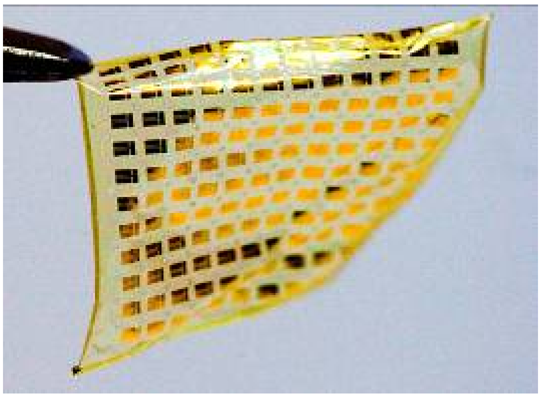

Figure 3-7 Thin and flexible feature of ultra-thin device: Si-CMOS inverters

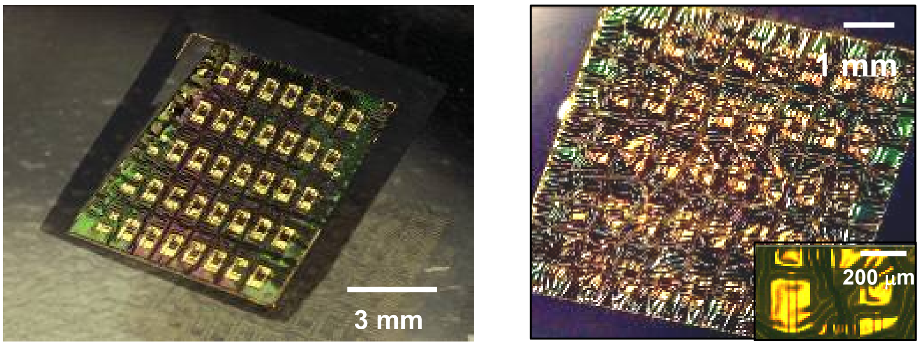

Figure 3-8 Wavy ultrathin Si-CMOS inverters

3.2 Pattern Observation and Device Characterization

3.2.1 Pattern Observation of Wavy Si-CMOS inverters

The release of strain, after transfer printing onto the pre-strainted PDMS, makes PDMS and an ultrathin devices shrink, and as a result forms wavy structures. Figure 3-9 shows optical micrographs of wavy Si-CMOS inverters formed with $\varepsilon_{pre} = 2.7\%$, 3.9% and 5.7%. The wave structures have complex layouts associated with nonlinear buckling physics in a mechanically heterogeneous system. Three features are notable. (1) The waves form most readily in the regions of smallest flexural rigidity, i.e. along the interconnect lines between the $p-$MOSFET and $n-$MOSFET sides of the inverter and the electronically inactive parts of the circuit sheet. (2) The wave structures begin to extend from the interconnect lines as ε_{pre} increases, to all parts of the circuit, including the comparatively rigid device regions. (3) The etch holes, which appear near the centers of these images, have a strong influence on the waves. In particular, waves tend to nucleate at these locations: they adopt wave vectors oriented tangential to the perimeters of the holes, due to the traction-free edges at these locations. Cracks form, most commonly in the metal electrodes near the etch holes, when local strains rise to levels 1~2% greater than the local prestrain. The maximum prestrain is ~10%, but the higher prestrain values could lead structure to cracking when prestrain is released. This behaviour can be quantitatively captured using FEM simulation and will be shown in Chapter Seven.

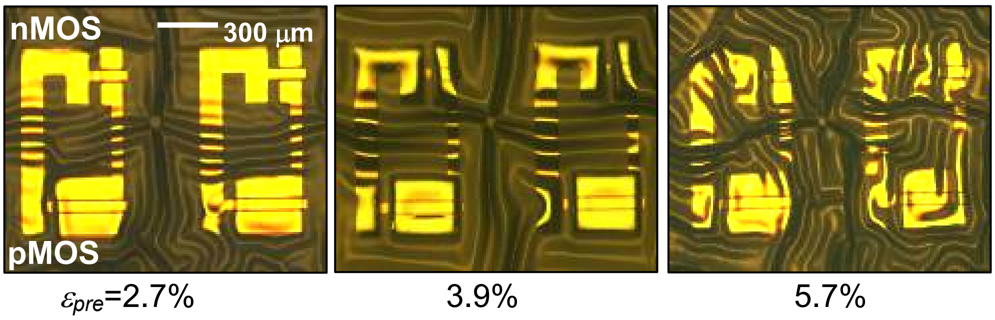

Figure 3-9 Wavy Si-CMOS inverters formed

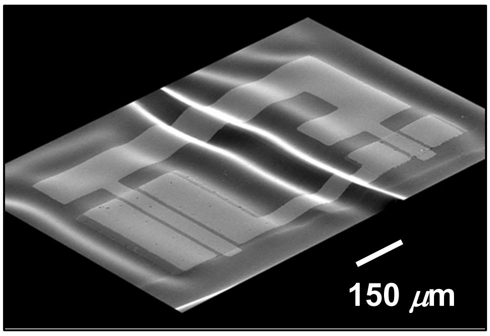

Figure 3-10 SEM of wavy Si-CMOS inverters

Figure 3-11 shows images of inverters under different tensile, and uniaxial applied strains, for a wavy circuit fabricated with ε_{pre}= 3.9%. The amplitudes and periods of the waves that lie along the direction of the applied force, decrease and increase respectively, to accommodate for the resultant strains. The Poisson effect causes compression in the orthogonal direction, which leads to increases and decreases in the amplitudes and periods of waves with this orientation, respectively.

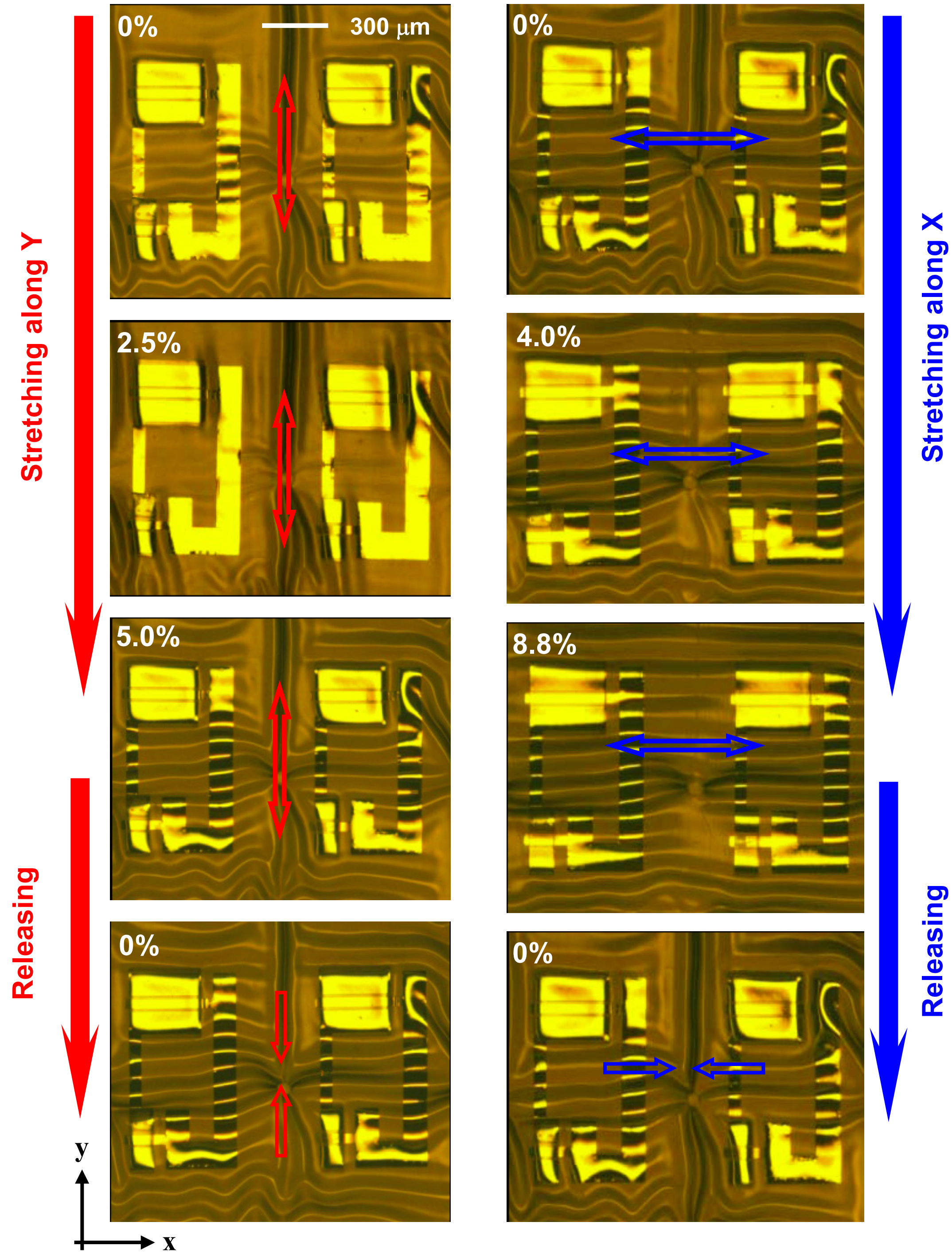

Figure 3-11 Wavy Si-CMOS inverters under tensile strains in x and y directions

3.2.2 Electric Performance of Wavy Si-CMOS inverters

Electric performance is important for wavy Si-CMOS inverters throughout a certain range of applied strains. Electrical measurements are performed for the Si-CMOS inverters working under applied strain. The strains applied on Si-CMOS inverters using mechanical bending stages that can load uniaxial tensile or compressive strains in any direction. The mechanical stretching stage is mounted directly on the electrical probing station that is coupled with semiconductor parameter analyzers (Agilent, 5155C).

Figure 3-12 presents the electrical properties of individual $n-$MOSFET and $p-$MOSFET devices with channel widths (W) of 300 μm and 100 μm, respectively, The measured and numerically simulated (by PSPICE) transfer curves are show in Figure 3-13 to match current outputs, and channel lengths (L_c) of 13 μm. These data indicate effective mobilities of 290 cm^2/Vs, and 140 cm^2/Vs for the n and p channel devices, respectively: the on/off ratios in both cases are >10^5. The gains exhibited by the inverters are as high as 100 with a supply voltage (V_{DD}) of 5V: this is consistent with circuit simulations that use the individual transistor responses.

Figure 3-14 summarizes the voltage at maximum gain, (V_M) for different $\varepsilon_{applied}$ along the x and y directions. Tensile strains parallel to the transistor channels, i.e. along the y direction, tend to reduce the compressive strains associated with the wavy structures in these locations. The complex, spatially-varying strain distributions and the practical difficulties associated with probing the devices make simple explanations for the associated changes in electrical properties elusive. It is also can be concluded the sensitivities of the p and n channel devices using Figure 3-15.

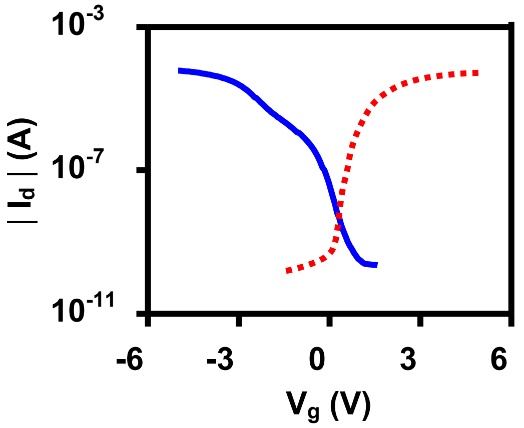

Figure 3-12 Measured and simulated $n-$ (blue) and $p-$(red) channel MOSFETs

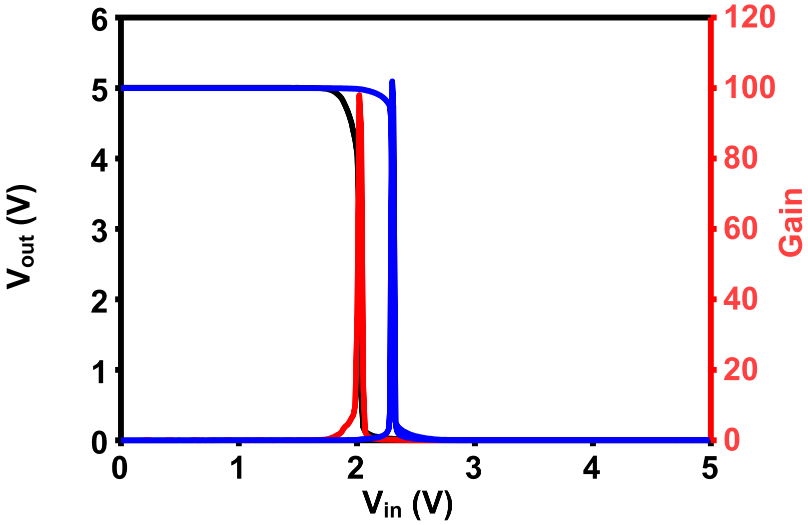

Figure 3-13 Measured (red and black) and simulated (blue) transfer characteristics of wavy inverters

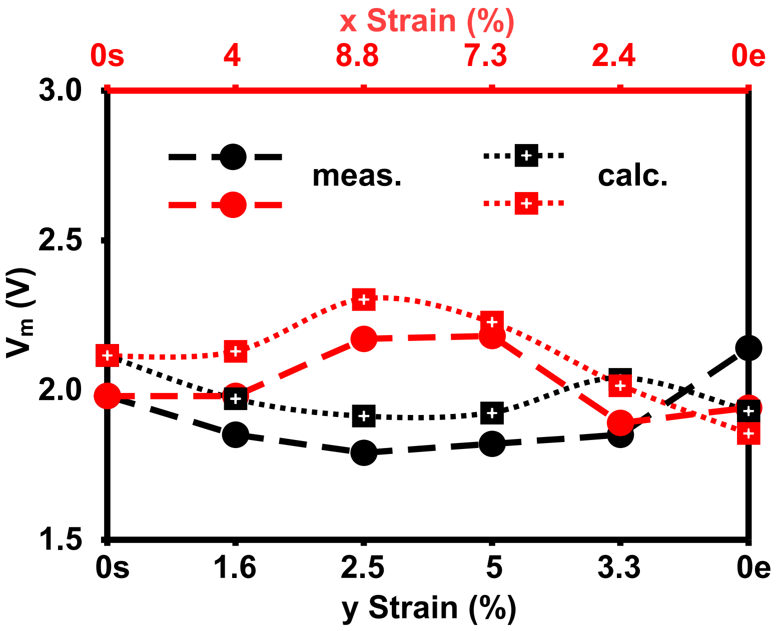

Figure 3-14 Measured (solid circles) and simulated (open squares) inverter threshold voltages for different applied strains (x and y directions)

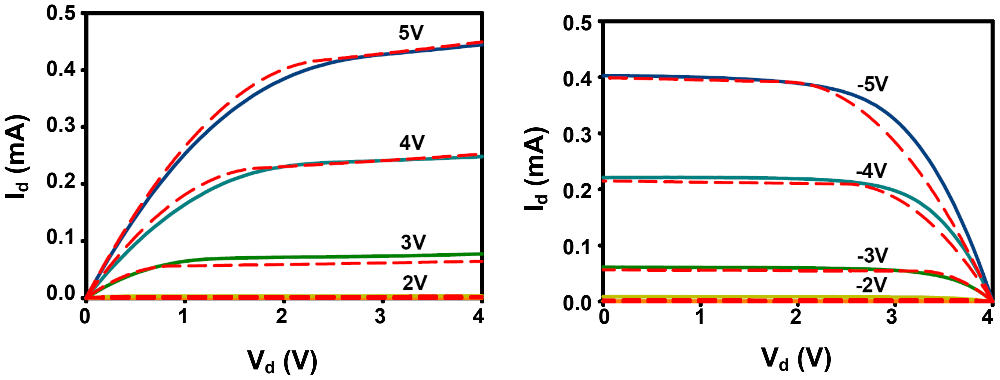

Figure 3-15 IV curves for NMOS (left) and PMOS (right) at 0% strain; measurement (solid lines) and simulation (dot lines)

Generally, the overall tensile and compressive strains in these systems could increase and decrease the electron mobility, respectively, with opposite effects on hole mobility (Thompson, et al., 2004; Maikap, et al., 2004; Moroz, et al., 2003), consistent with analysis of measured transistor data using standard long channel MOS device models (Streetman and Banerjee 1981). Tensile strains in the *x* direction, i.e.

perpendicular to the channels, cause compressive opposite mechanical strains, due to the Poisson effect, and therefore also opposite changes in the electrical properties. At the level of the inverters, the changes in the transistors cause decreases and increases in V_M of parallel and perpendicular strains, respectively. Individual measurements of the transistors at these various strain states enable simulations of changes in the inverters.

3.2.3 Profile of Wavy Si-CMOS inverters

In order to measure the wavelength and amplitude of wavy ultrathin electronic devices a surface profiler (Sloan Dektak 3) is used. A diamond stylus, in contact with a sample surface, moves and follows the surface profile of and measures physical surface variation at different positions.

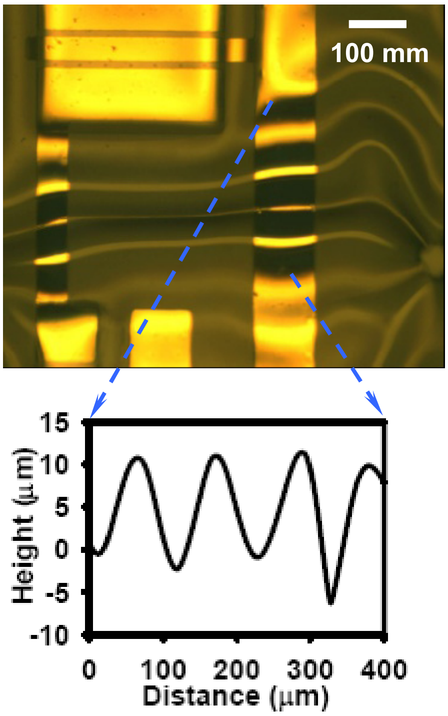

(a) Thin metal electrode part

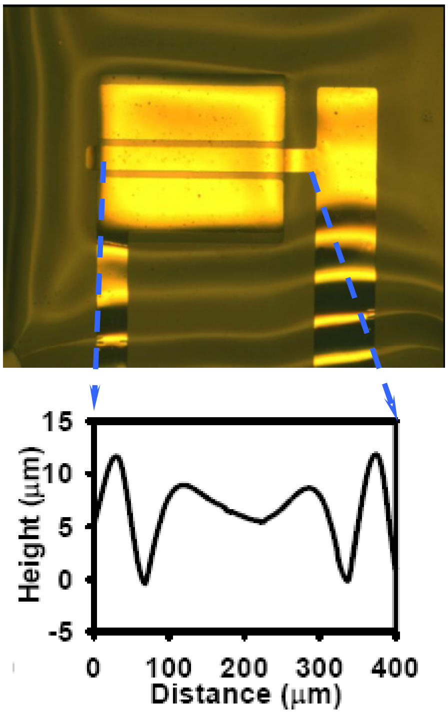

(b) Thick device part for $p-$MOS

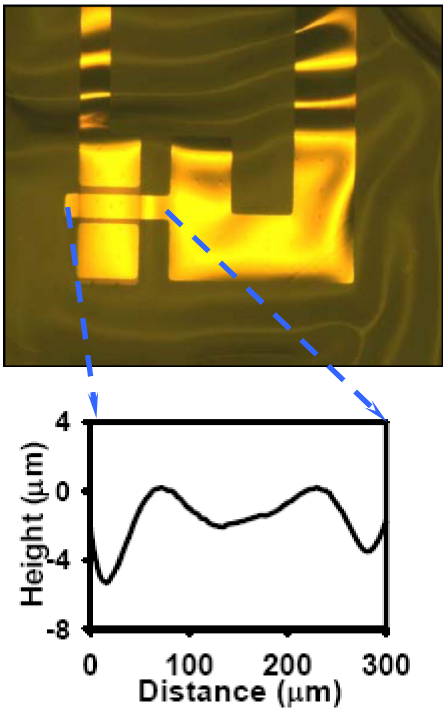

(c) Thick device part for $n-$MOS

Figure 3-16 Wavelength and amplitude measurement of wavy ultrathin devices

3.3 Fabrication of Si-CMOS ring oscillators

More complex stretchable circuits can be fabricated using Si-CMOS inverters as building blocks. Figure 3-17 shows optical images and stretching tests on Si-CMOS ring oscillators that use three Si-CMOS inverters. The mechanical responses are qualitatively consistent with considerations described in the discussion of the Si-CMOS inverters (Kim, et al., 2008).

The electrical measurements (Figure 3-18) indicate stable oscillation frequencies of ~3.0 MHz at supply voltages of 10 V, even under severe buckling deformations and strains of 5% and larger. The measured frequencies (Figure 3-19) are 2.9 MHz, 3.0 MHz, 3.1 MHz and 2.9 MHz for 0%, 2.5%, 5% and 0% applied strain, respectively. Formulating detailed explanations for these relatively small shifts is difficult, for reasons similar to those outlined in the discussion of the inverters in Section 3.2.2. The expected strain induced anisotropy in transport (Servati and Nathan. 2005) must also be considered. More general classes of circuits are also possible to be made using this method.

Figure 3-20 shows a differential amplifier (Ahn, et al., 2007) for a structural health monitor that integrates four components: a current source (three transistors with L_c = 30 μm and W = 80 μm), a current mirror (two transistors with L_c = 40 μm, W = 120 μm, L_c = 20 μm, and W = 120 μm), a differential pair (two transistors with L_c = 30 μm and W = 180 μm), and a load (two transistors with L_c = 40 μm and W = 80 μm). Figure 3-21 shows an optical image of the corresponding wavy circuit. This amplifier is designed to provide a voltage gain of ~1.4 for a 500 mV peak-to-peak input signal. Measurements (Figure 3-22) at various tensile strains along the red arrow show gains that vary by less than ~15%: 1.01 without applied strain (0% s; black), 1.14 at 2.5% strain (red), 1.19 at 5% strain (blue) and 1.08 after release (0% e; green).

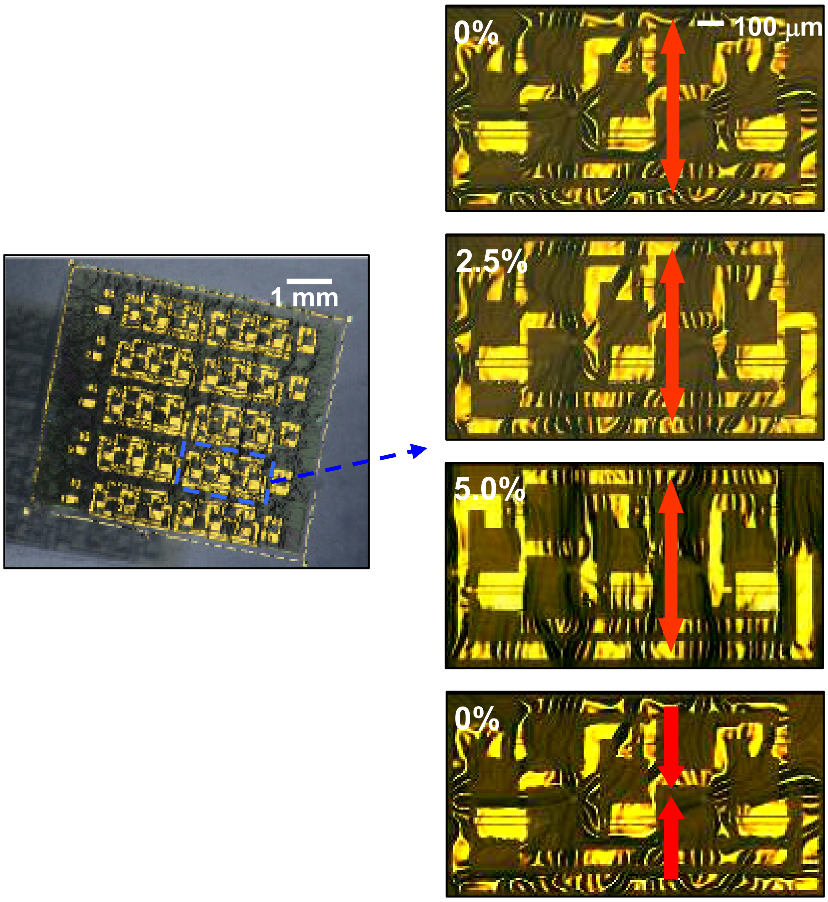

(a) (b)

Figure 3-17 Optical image of array of stretchable

(a) Wavy three stage CMOS ring oscillators

(b) Magnified views of oscillator at different applied strains along red arrow.

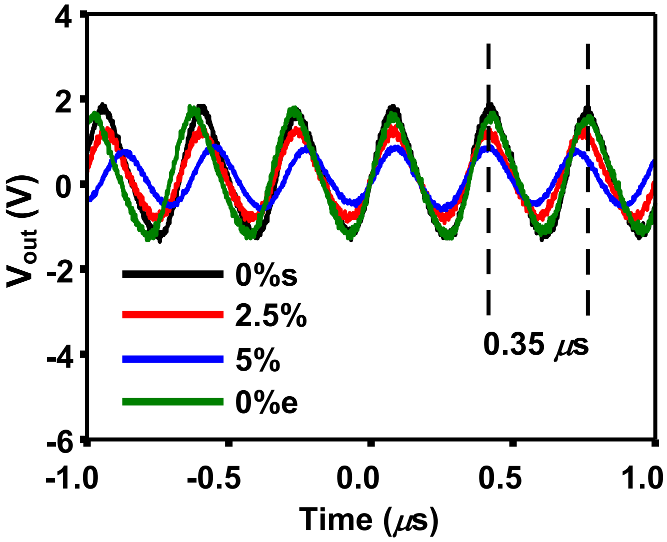

Figure 3-18 Time domain responses of an oscillator at different applied strains

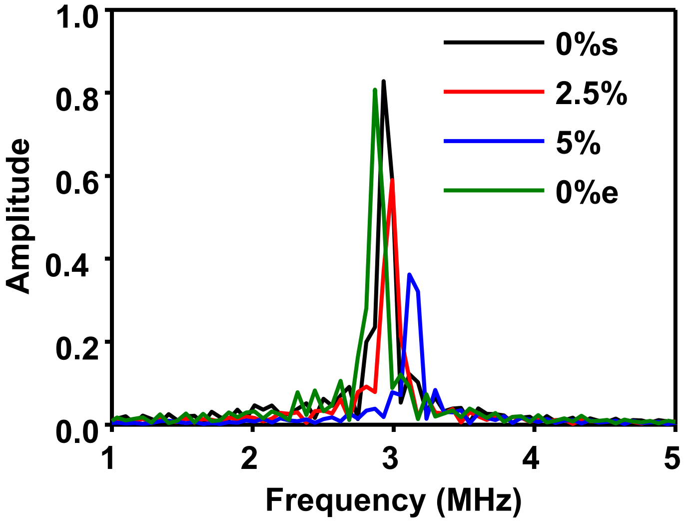

Figure 3-19 Frequency domain responses of an oscillator at different applied strains

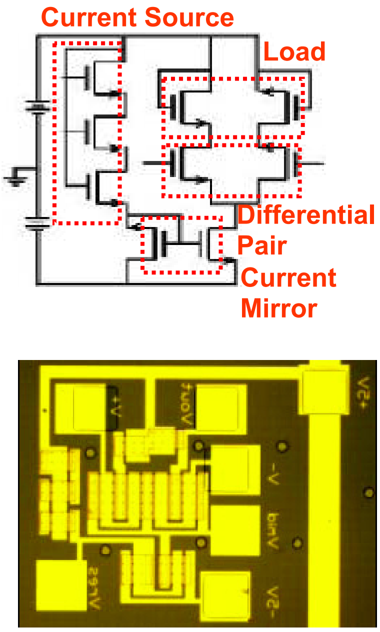

Figure 3-20 Circuit diagram of differential amplifier

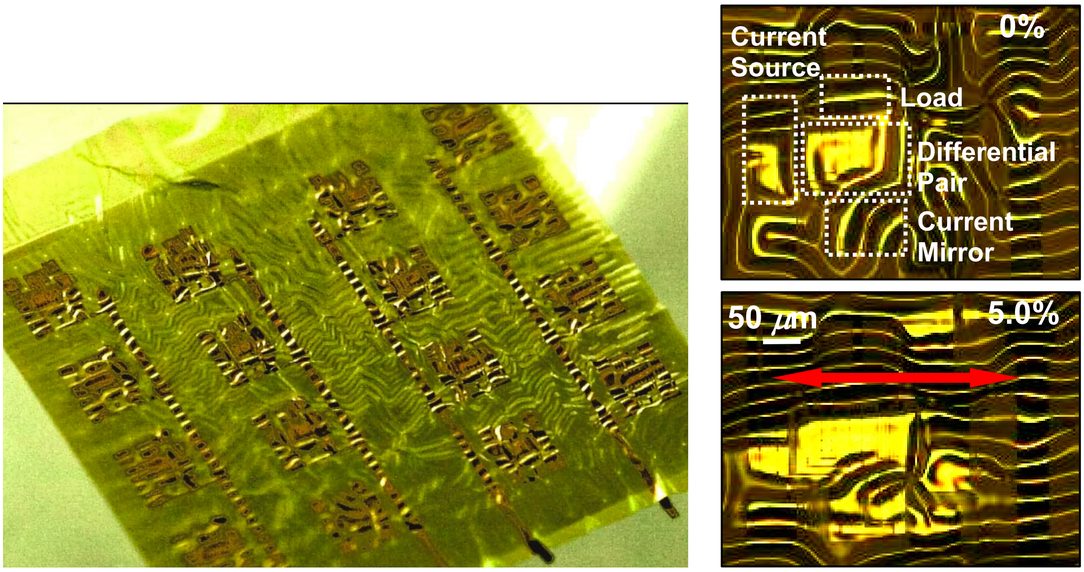

Figure 3-21 Wavy differential amplifier in its as-fabricated state and under applied strain in direction along red arrow

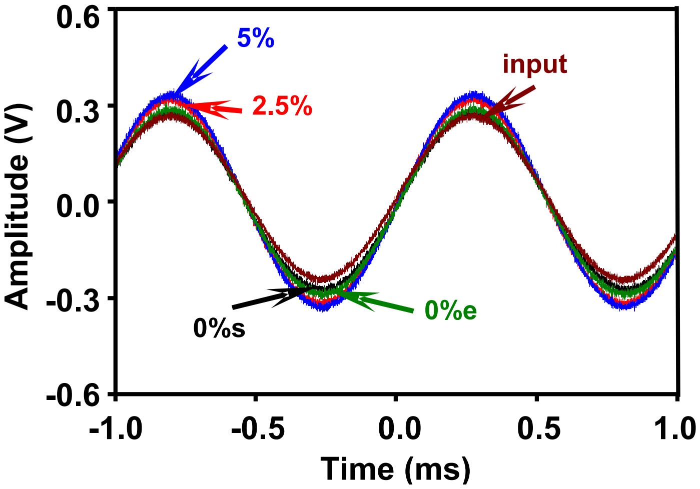

Figure 3-22 Output characteristics for various strain values

The fabrication process of this new type of integrated circuit presented here demonstrates the degree to which extreme mechanical properties, i.e. stretchability, and foldability, can be achieved in fully formed, high performance integrated circuits by use of optimized structural configurations and multilayer layouts, even with intrinsically brittle but high performance inorganic electronic materials. The desired mechanical properties achieved in this approach, are enabled by materials, e.g. PDMS, and thin PI and their multilayer assemblies that do not need to provide any active electronic functionality. Such designs offer the possibility of direct integration of electronics with biological systems, medical prosthetics and monitoring devices, complex machine parts, or with mechanically rugged, lightweight packages for other type of devices.

Chapter Four

Linear Analytical Study for Single Crystal Silicon

Stretchable electronic devices are different from conventional microelectronic devices since the former are expected to experience significant strains, and such strains may lead to device failure (mechanical or electrical). The mechanical behaviour of stretchable electronics is important since it can establish important design criteria concerning device failure. For example, mechanics analysis could yield the maximum strain or stress in a silicon ribbon, or the critical strain for buckling and so on. Furthermore it could find the relation between strain in a silicon ribbon and the silicon ribbon thickness, and elastic properties including the applied strain and prestrain. It is important to find the range of applied strain that the system can sustain without fracturing the silicon in its application.

4.1 Analytical Model

Consider a thin film of a stiff material (e.g. single crystal silicon) on a substrate of compliant material (e.g. PDMS) (see Figure 4-1). Subject to a compressive membrane force, the film may form a pattern of wrinkles, and may still remain bonded to the substrate (see Chapter Two experimental observation). This wrinkled system could then be used as a method to evaluate the mechanical properties of materials (Stafford et al., 2005).

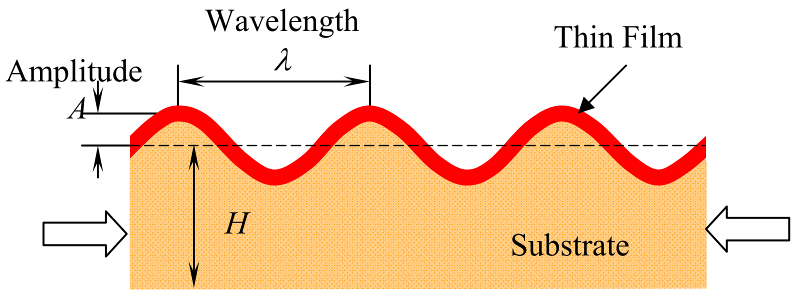

Figure 4-1 Wrinkled stiff thin film-compliant substrate system

In the case of a thin film partially debonded from a substrate, the film buckles like an edge-clamped plate when the compressive membrane force exceeds a critical value. The critical membrane force depends on the size of debond (Hutchinson and Suo, 1991). As the magnitude of the initial membrane force increases, the debonded film buckles into a complex pattern and the wavelength decreases (Gioia and Ortiz, 1997; Audoly, 2000). The buckled film may behave like a sheet of crumpled paper (Lobkovsky, et al., 1995; Ben Amar and Pomeau, 1997). The mechanical procedure is the opposites to the case of Goenewold, (2001), which concerns stretching of the thin plate, followed by a bonding to a soft substrate.

Much of the existing theoretical work on substrate-bonded films has been based on a linear perturbation analysis, as reviewed by Niu and Talreja (1999). Such an analysis determines the critical membrane force and the wavelength of the wrinkles, but leaves several questions unanswered with regards to, for example, the amplitude variation of the wrinkles, the wavelength changing with the amplitude increases and the surface pattern of wrinkles. Several recent nonlinear analyses have attempted to answer these questions. Cerda and Mahadevan (2003), Chen and Hutchinson (2004a) and Huang (2005) have calculated the wavelength and amplitude of sinusoidal wrinkles. Chen and Hutchinson (2004b) have found the herringbone pattern has the minimum energy among several other patterns that were computed. Huang et al. (2004) have shown, using numerical simulation and modeling the substrate as an array of springs and dashpots that wrinkles can evolve into several patterns, depending on the anisotropy of the membrane forces.

This study focuses on wrinkles in a substrate-bonded thin film (Figure 4-1). Specifically, the film is bonded to a pre-strained compliant substrate (see Chapter Two). It is shown here that the amplitude and wavelength of the sinusoidal wrinkles are functions of the modulus and thickness of the substrate. The analyses extend that of Chen and Hutchinson (2004a and b) and Huang (2005) to a film on a substrate of finite thickness, and complement the scaling analysis of Cerda and Mahadevan (2003). The analytical results give the relationship of wavelength and amplitude of the wrinkles as the wrinkles increases.

4.2 Governing Equations

A thin film on a substrate is typically flat and subject to a state of biaxial membrane strains, ε_{11}^{0} and ε_{22}^{0} , taken to be uniform in the film. The principal directions of the strain tensor coincide with the coordinates x_1 and x_2, so that ε_{12}^{0}=0. This flat state is assumed to be the reference state, and deformation is defined with respect to this state (see Figure 4-2). The wavelength (λ) is much larger than the film thickness (t). Accordingly, von Karman elastic nonlinear plate theory adequately models the film (Timoshenko and Woinowsky, 1959, Timoshenko and Gere, 1963). The governing equations in term of the film deflections (w) is

$$D\nabla^4 w - (N_{11} w,_{11} + N_{22} w,_{22} - 2N_{12} w,_{12}) = -p \tag{4-1a}$$

$$\frac{1}{Et}\nabla^4 F = w,_{12}^2 - w,_{11}\, w,_{22} \tag{4-1b}$$

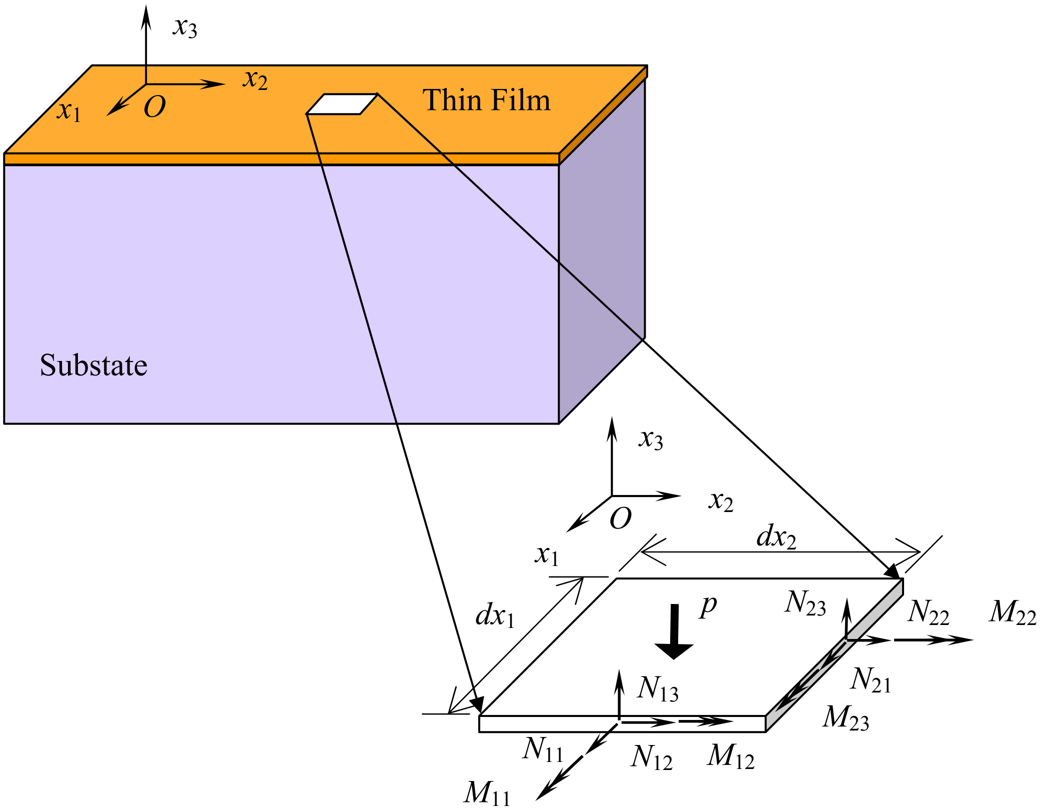

Figure 4-2 Forces applied to an infinitesimal thin film plate element

here, ∇^4 is the bi-harmonic operator,

$D = E_f t^3 / [12(1-\nu_f^2)]$ is the bending stiffness of the plate (thin film),

t is thin film thickness,

E_f is Young's modulus of the plate (thin film),

ν_f is Poisson's ratio of the plate (i.e. thin film),

w is the displacement perpendicular to the plane i.e. film deflections,

p is the stress component acting perpendicular to the plate that is exerted by the substrate,

$(\ )_{,\alpha} \equiv \partial(\ )/\partial x_\alpha$ is differential operator,

$N_{\alpha\beta} = \int \sigma_{\alpha\beta} dx_3$ is the stress resultant in the plane of the plate, and

F is the Airy stress function with $(N_{11} = F_{,22}, N_{22} = F_{,11}, N_{12} = F_{,12})$.

Let the in-plane displacements in the x_1 and x_2 directions be u_1 and u_2 respectively. The membrane strains $\varepsilon_{\alpha\beta}$ arise from three components: the initial strains, the gradients of the in-plane displacements, and the rotation caused by the deflection, that is,

$$\varepsilon_{\alpha\beta} = \varepsilon_{\alpha\beta}^{0} + \frac{1}{2}\left(\frac{\partial u_\alpha}{\partial x_\beta} + \frac{\partial u_\beta}{\partial x_\alpha}\right) + \frac{1}{2}\frac{\partial w}{\partial x_\alpha}\frac{\partial w}{\partial x_\beta} \qquad (\alpha, \beta = 1,2) \qquad \text{(4-2)}$$

While Equation (4-1) is the equilibrium equation, Equation (4-2) is the compatibility equation ensuring the existence of the governing in-plane displacement gradients, $u_{\alpha,\beta}$. The tangential components of the traction exerted by the substrate on the plate are ignored. This is a commonly used approximation in the analysis of wrinkling of a thin film on compliant substrate, (Allen, 1969). The middle surface strains are related to the displacements by Hooke's law:

$$\varepsilon_{\alpha\beta} = \frac{1}{2}(u_{\alpha,\beta} + u_{\beta,\alpha}) + \frac{1}{2} w_{,\alpha} w_{,\beta} \qquad \text{(4-3)}$$

The constitutive relations are as follows, where $M_{\alpha\beta}$ is the bending moment tensor. ($\delta_{\alpha\beta}$ is Kronecker delta).

$$N_{\alpha\beta} = [E_f(1-\nu_f^2)][(1-\nu_f)\varepsilon_{\alpha\beta} + \nu\varepsilon_{\gamma\gamma}\delta_{\alpha\beta}] \qquad (\alpha, \beta, \gamma = 1,2) \qquad \text{(4-4a)}$$

$$M_{\alpha\beta} = D[(1-\nu_f)w_{,\alpha\beta} + \nu_f w_{,\gamma\gamma}\delta_{\alpha\beta}] \qquad \text{(4-4b)}$$

On the interface between thin film and substrate, the traction force components T_1 and T_2 are

$$T_\alpha = \frac{\partial N_{\alpha\beta}}{\partial x_\beta} \quad (\alpha, \beta = 1,2) \tag{4-5}$$

and the normal traction force T_3 is

$$T_3 = -\frac{t^3 E}{12} \frac{\partial^4 w}{\partial^2 x_\alpha \partial^2 x_\alpha} + \frac{\partial}{\partial x_\beta}\left(N_{\alpha\beta} \frac{\partial w}{\partial x_\alpha} \right) \tag{4-6}$$

Thermal expansion method is used to prestrain the stiff thin film-compliant substrate system, Young's modulus, Poisson ratio and the coefficient of thermal expansion of the film are denoted by E_f, ν_f and α_f. The corresponding quantities for the substrate are denoted by E_s, ν_s and α_s. While the thin film thickness is t and the substrate is assumed to be infinitely thick, thus, it imposes its in-plane strains on the film. Assuming that the film is deposited on the substrate when both are at temperature T_D and the temperature of the system is then reduced by ΔT_D, and assuming that the film is elastic and unbuckled, the compressive equi-biaxial pre-stress stress, σ_0, in the film is

$$\sigma_{11} = \sigma_{22} = -\sigma_0 = -[E_f / (1 - \nu_f)] \int_{T_D - \Delta T_D}^{T_D} \Delta\alpha dT \tag{4-7}$$

where $\Delta\alpha = \alpha_s - \alpha_f$. For the systems under consideration $\Delta\alpha > 0$ and $\sigma_0 > 0$.

4.3 Criterion of Buckling

The critical stress or strain can be found using linearized stability analysis (Chen and Hutchinson, 2004a and b). The film is assumed to be infinite in length in the x_1 and x_2 directions. The unbuckled film has a uniform stress state given by

$N_{11} = N_{22} = \sigma_0 t$ and $N_{12} = 0$. The classical buckling analysis, based on linearization of Equations (4-1) and (4-2) about the pre-buckling state, leads to

$$D\nabla^4 w + \sigma_0 t \nabla^2 w = -p \tag{4-8}$$

The system of equations admits periodic solutions of the form (Chen and Hutchinson, 2004):

$$\begin{aligned} w &= \overline{w}\cos(k_1 x_1)\cos(k_2 x_2) \\ p &= \overline{p}\cos(k_1 x_1)\cos(k_2 x_2) \end{aligned} \tag{4-9}$$

here is (4-8) gives

$$(\Delta k^4 - \sigma_0 t k^2)\overline{w} = -\overline{p} \tag{4-10}$$

where $k = (k_1^2 + k_2^2)^{1/2}$.

The exact solution for the normal deflection of the surface, δ, of the infinitely deep substrate under normal loading p in Equation (4-9) with zero tangential tractions at the surface is

$$\delta = \overline{\delta}\cos(k_1 x_1)\cos(k_2 x_2) \tag{4-11}$$

where $\overline{\delta} = -\overline{p}/(\overline{E}_s k)$ with $\overline{E}_s = E_s/(1-\nu_s)$.

Combining $(Dk^4 - \sigma_0 t k^2)\overline{w} = -\overline{p}$ and $\overline{\delta} = 2\overline{p}/(\overline{E}_s k)$ subject to continuity e.g. $\overline{w} = \overline{\delta}$ gives the eigenvalue equation

$$\sigma_0 t = Dk^2 + \overline{E}_s / 2k \tag{4-12}$$

The critical buckling stress, σ_{cr}, is the minimum eigenvalue with respect to k, which is attained for $k_{cr} t (3\overline{E}_s/\overline{E}_f)^{1/3}$ giving

$$\varepsilon_{cr} = \frac{\sigma_{cr}}{\overline{E}_f} = \frac{1}{4}\left(3\frac{\overline{E}_s}{\overline{E}_f}\right)^{2/3} \tag{4-13}$$

with $\overline{E}_f = E_f/(1-\nu_f^2)$. This is the result for the one-dimensional, plane-strain wrinkling stress, which is widely known, (Allen, 1969). Note, however, for an equi-biaxial pre-stress, the critical stress applies not only to the one-dimensional mode with $k_1 = k_{cr}$ and $k_2 = 0$, but to any mode whose wave numbers satisfy

$$(k_1^2 + k_2^2)^{1/2} t = k_{cr} t = (3\overline{E}_s / \overline{E}_f)^{1/3} \tag{4-14}$$

The compressed film in the equi-biaxial state has multiple modes associated with the critical buckling stress. In what follows, both the one-dimensional mode and the square checkerboard mode with $k_1 = k_2 = k_{cr}/\sqrt{2}$ will be investigated.

4.4 Buckling Analysis

The experimental observation (illustrated in Chapter Two) shows that the stiff thin film-compliant substrate system become sinusoidal wrinkling once the strain reaches the critical buckling strain (Equation 4-13). Chen and Hutchinson (2004a) analyzed the sinusoidal wrinkles, of the deflection field $w = A\cos(kx)$ in a film on a substrate of infinite thickness, where A is the amplitude, k is the wave number and $\lambda = 2\pi/k$ is the wavelength. Huang et al. (2005) extended the solutions to analyze a film on a substrate of finite thickness, and showed that the wavelength of the wrinkles remains constant as the amplitude of the wrinkles increases.

To obtain the analytical solution, the shear stresses at the film/substrate interface are assumed to be zero (Huang et al. 2005). Therefore, the membrane forces N_{11} and N_{22} must be uniform in the film for the in-plane equilibrium equations (4-5) to be tenable. The membrane strains, according to Equation (4-3), are also uniform in the film. When $w = A\cos(kx_1)$ is substituted into Equation (4-1), the uniformity of the strains requires that the in-plane displacement field be

$$u_1 = \frac{1}{8}kA^2 \sin(2kx_1) \tag{4-15}$$

The membrane strains are

$$\begin{aligned} \varepsilon_{11} &= \varepsilon_{11}^0 + \frac{1}{4}k^2A^2 \\ \varepsilon_{22} &= \varepsilon_{22}^0 \\ \varepsilon_{12} &= 0 \end{aligned} \tag{4-16}$$

Thus the membrane forces are

$$\begin{aligned} N_{11} &= N_{11}^0 + \frac{1}{4}t\overline{E}_f k^2A^2 \\ N_{22} &= N_{22}^0 + \frac{1}{4}t\overline{E}_f k^2A^2 \\ N_{22} &= 0 \end{aligned} \tag{4-17}$$

where $N_{11}^0 = t\overline{E}_f(\varepsilon_{11}^0 + \nu\varepsilon_{22}^0)$

$N_{22}^0 = t\overline{E}_f(\varepsilon_{22}^0 + \nu\varepsilon_{11}^0)$

and N_{11}^0 and N_{22}^0 are initial membrane forces along the x_1 and x_2 directions, respectively. When $N_{11}^0 < 0$, the thin film is compressive. Once buckling occurs, the wrinkles change the in-plane quantities by quadratic terms in the amplitude, A. This dependence is expected from the quadratic contribution of the rotation to the membrane strains. But from the symmetrical contribution such that a change in the sign of the wrinkle amplitude, it does not change the in-plane quantities.

To find the values of the amplitude and wavelength, the average elastic energy per unit area is calculated for the wrinkled state (Huang et al. 2005). The average elastic energy is contributed by both components: thin film and substrate. The elastic energy in thin film is generated by membrane force and bending moment. Thus the total elastic energy consists of the following three parts.

(a) The membrane energy in the film is given by

$$U^m = \frac{1}{2}(N_{11}\varepsilon_{11} + N_{22}\varepsilon_{22}) = U^0 - \frac{1}{4}|N_{11}|k^2A^2 + \frac{t\overline{E}_f}{32}k^4A^4(N_{11}\varepsilon_{11} + N_{22}\varepsilon_{22}) \tag{4-18}$$

where $U^0 = \frac{t\overline{E}}{2}\left|(\varepsilon_{11}^0)^2 - 2\nu_f\varepsilon_{11}^0\varepsilon_{22}^0 + (\varepsilon_{22}^0)^2\right|$, is the initial energy in the flat film. Being constant, U^0 does not affect energy minimization. In the wrinkled state, the compressive membrane force reduces the energy. However, the wrinkles stretch the film, giving rise to the last term in Equation (4-18), and increasing the membrane energy: it is this term that stabilizes the wrinkle amplitude.

(b) The bending energy in the film is given by

$$U^b = \frac{k}{2\pi}\int_0^{2\pi/k}\frac{t^3\overline{E}_f}{24}\left(\frac{\partial^2 w}{\partial x_1^2}\right)^2 dx_1 = \frac{t^3\overline{E}_f}{48}k^4A^2 \tag{4-19}$$

(c) The energy in substrate is obtained by assuming the substrate a layer of elastic solid, of thickness H. Consider the boundary value problem of the substrate. The substrate is subject to $w = A\cos(kx_1)$ and zero shear stress on the top surface and rigidly constrained on the bottom surface. To solve this boundary value problem of the elastic field in the substrate, the separation of variables x_1 and x_3, is used and it is found that $T_3 = g\overline{E}_s kw$, with

$$g(kH,\nu_s)=\frac{(3-4\nu_s)\cosh(2kH)+5-12\nu_s+8\nu_s+2(kH)^2}{(6-8\nu_s)\sinh(2kH)-4kH}. \tag{4-20}$$

Figure 4-3 shows g is a monotonically decreasing function of kH.

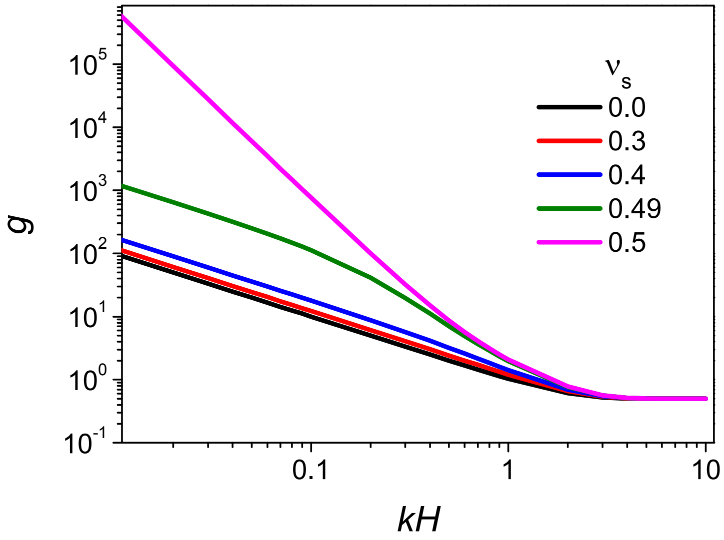

Figure 4-3 Dimensionless stiffness g as function of kH (Huang et al. 2005)

The thicker the substrate, the smaller the normal stress is needed to deform the top surface. The energy in the substrate is

$$U_s=\frac{k}{2\pi}\int_0^{2\pi/k}\frac{1}{2}T_3wdx_1=\frac{\overline{E}_s}{4}gkA^2 \tag{4-21}$$

The sum of the above three contributions gives the total energy of t stiff thin film-compliant substrate system, that is,

$$U(A,k)=U^m+U^b+U^s=U^0+\frac{1}{4}(t\overline{E}_f\phi-\left|N_{11}^0\right|)k^2A^2+\frac{t\overline{E}_f}{32}k^4A^4 \tag{4-22}$$

where $\phi=\frac{(kt)^2}{12}+\frac{g\overline{E}_s}{(kt)\overline{E}_f}$.

The energy for the bonded film and substrate is a fourth order polynomial in the amplitude A. When $\left|N_{11}^0\right| < t\overline{E}_f\phi$, the energy is minimal at the state $A = 0$, i.e. the film is flat. When $\left|N_{11}^0\right| > t\overline{E}_f\phi$, the flat film corresponds to a local energy maximum, and the energy minimizes when the film forms wrinkles with amplitude

$$A = \frac{2}{k}\left(\frac{|N_{11}{}^0|}{\overline{E}_f t} - \phi\right)^{1/2} \tag{4-23}$$

Substituting (4-23) into (4-21), the energy can be expressed as a function of the wave number

$$U(k) = U^0 - \frac{h\overline{E}}{2}\left(\frac{|N_{11}{}^0|}{\overline{E}_f t} - \phi\right)^2 \tag{4-24}$$

The equilibrium wrinkles state is at the wave number k_{eq} that minimizes the function $U(k)$ or, equivalently, the function $\phi(kt)$. Consequently, the wavelength of the wrinkles in equilibrium is independent of the initial membrane force, and remains constant as the amplitude of the wrinkles increases.

The critical membrane force for the onset of wrinkles is $N_{cr} \equiv t\overline{E}_f\phi_{\min}$, and Equation (4-23) reduces to

$$A = \frac{2}{k_{eq}}\left(\frac{|N_{11}{}^0| - N_{cr}}{\overline{E}_f t}\right)^{1/2} \tag{4-25}$$

The wrinkle amplitude is quadratic in excess of the membrane force. Equation (4-25) was derived by Chen and Hutchinson (2004) for a film on a substrate of infinite thickness. They also showed that it is also valid for a film on a substrate of finite thickness.

Three extreme cases are described based on the analytical results (Huang et al. 2005). The first extreme case is thick substrate, i.e. $kH \to \infty$ and the wavelength is the only length in the boundary value problem, so g that should be a constant; Equation (4-20) gives $g(\nu_s, \infty) = \frac{1}{2}$, which is independent of Poisson's ratio. Minimizing the function ϕ, Equation (4-22), the thick-substrate limits are reproduced here for convenience (Chen and Hutchinson, 2004):

$$\lambda_{eq} = 2\pi t \left(\frac{\bar{E}_f}{3\bar{E}_s} \right)^{1/3}$$

$$N_{cr} = \frac{1}{4} t\bar{E} \left(\frac{3\bar{E}_s}{\bar{E}_f} \right)^{1/3} \qquad (4\text{-}26)$$

$$A_{eq} = t \left(\frac{|N_{11}{}^{0}|}{N_c} - 1 \right)^{1/2}$$

The second extreme case is thin substrate, i.e. $kH \to 0$, and the stress field varies slowly in the x_1 direction. This limit can be analyzed using the Winkler model (Brush, and Almroth, 1975), which represents the substrate as a set of parallel springs with stiffness corresponding to that of a layer in a state of uniaxial strain, so that $T_3 = \left(\frac{(1-\nu_s)^2}{(1-2\nu)} \right) \frac{\bar{E}_s w}{H}$. The Winkler model is consistent with Equation (4-20), which gives the limit $g(kH, \nu_s) \to= [(1-\nu_s)^2/(1-2\nu_s)](k/H)^{-1}$ as $kH \to 0$. This limit is indicated in Figure 4-3 for $\nu_s = 0.0$ to 0.5. For this thin-substrate case, the limit of wavelength, amplitude and membrane force is obtained:

$$\lambda_{eq} = 2\pi t\left(\frac{H\overline{E}_f(1-2\nu_s)}{12\overline{E}_s(1-\nu_s)^2}\right)^{1/4}$$

$$N_{cr} = t\overline{E}_f\left(\frac{t\overline{E}_s(1-\nu_s)^2}{3H\overline{E}_f(1-2\nu_s)}\right)^{1/2} \tag{4-27}$$

$$A_{eq} = t\left(\frac{2}{3}\left(\frac{|N_{11}{}^0|}{N_c}-1\right)\right)^{1/2}$$

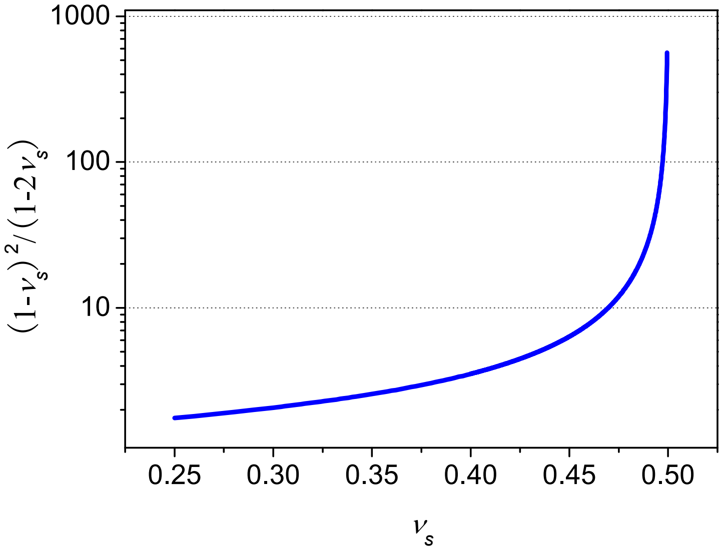

Figure 4-4 Sensitivity of $(1-\nu_s)^2/(1-2\nu_s)$ in terms of Poisson's ratio

The third extreme case concerns the sensitive dependence on Poisson's ratio. Poisson's ratio is the ratio of transverse contraction strain to longitudinal extension strain in the direction of stretching force. Compliant materials such as elastomers are nearly incompressible, with ν_s near 0.5. For nearly incompressible materials, the mechanical properties can be very sensitive to the exact value of the Poisson ratio (Koh and Kelly, 1989; Koh and Lam, 2001). Figure 4-4 highlights that the value of $\frac{(1-v_s)^2}{1-2v_s}$, which appears in Equation (4-27), is sensitive to Poisson's ratio v_s. When the substrate is nearly incompressible, the material is rigid under uniaxial strain conditions, and the Winkler model breaks down. The substrate does deform under sinusoidal stress on the top surface, but in a more complicated way. Equation (4-20) is still applicable when $v_s \to 0.5$, giving the limit $g(kH,0.5) \to (3/4)(kH)^{-3}$ as $kH \to 0$. In Figure 4-3, the thin-substrate limit for an incompressible substrate is indicated with $v_s = 0.5$, At $kH = 0.1$, for example, when Poisson's ratio changes from 0.3 to 0.5, g increases by more than an order of magnitude (Figure 4-3). For a nearly in compressible material, with $v_s = 0{,}49$ for example, Figure 4-5 shows that the g-coefficient approaches the Winkler limit when the substrate thickness is much smaller than the wavelength, but is well approximated by the incompressible limit when the substrate thickness is modestly small compared to the wavelength. When the substrate is incompressible, for the thin-substrate, the limitations obtained are:

$$\lambda_{eq} = 2\pi\sqrt{tH}\left(\frac{\overline{E}_f}{18\overline{E}_s}\right)^{1/6}$$

$$N_{cr} = \frac{t^2\overline{E}}{4H}\left(\frac{9\overline{E}_s}{4\overline{E}_f}\right)^{1/3} \tag{4-28}$$

$$A_{eq} = t\left(\frac{1}{2}\left(\frac{|N_{11}{}^{0}|}{N_c} - 1\right)\right)^{1/2}$$

The power-law relations in Equations (4-26) - (4-28) are predicted by Cerda and Mahadevan (2003) using a scaling analysis. Those calculations provide the explicit coefficients for the specific layered structure.

It should be cautioned that the elastomer is often taken as an incompressible material in practice. But the above discussion shows that the accurate Poisson's ratio should be used if the substrate is thin and nearly incompressible. For the same reason, the two thin-substrate limits, Equations (4-27) and (4-28), should be used with caution. A more reliable approach is to study the full results for substrates of arbitrary thicknesses, as to be presented in the later. However, the sensitive dependence on Poisson's ratio for wrinkles in a film on a thin substrate may lead to an experimental method to measure Poisson's ratio. Incidentally, wrinkles in a thin film on a thick substrate have been used to measure Young's modulus of the substrate (Stafford et al., 2004).

Figure 4-5 shows a plot of the critical membrane force N_{cr}, the wavelength λ_{eq}, and the wrinkle amplitude A_{eq} for a compressible substrate (ν_s=0.3) and for an incompressible substrate (ν_s=0.5) (Huang et al. 2005). For thick substrate and thin film much stiffer than the substrate (e.g. $\overline{E}_f / \overline{E}_s = 10^5$), wrinkles occur when the membrane strain exceeds about 10^{-4}. The wrinkle wavelength is several hundred times the film thickness, and the wrinkle amplitude is in the order of the film thickness. A thinner substrate, i.e. H/t is smaller, results in a higher critical membrane force and smaller wrinkle wavelength and amplitude. When the substrate is both thin and incompressible, even higher critical membrane forces is raised and smaller wrinkles are formed.

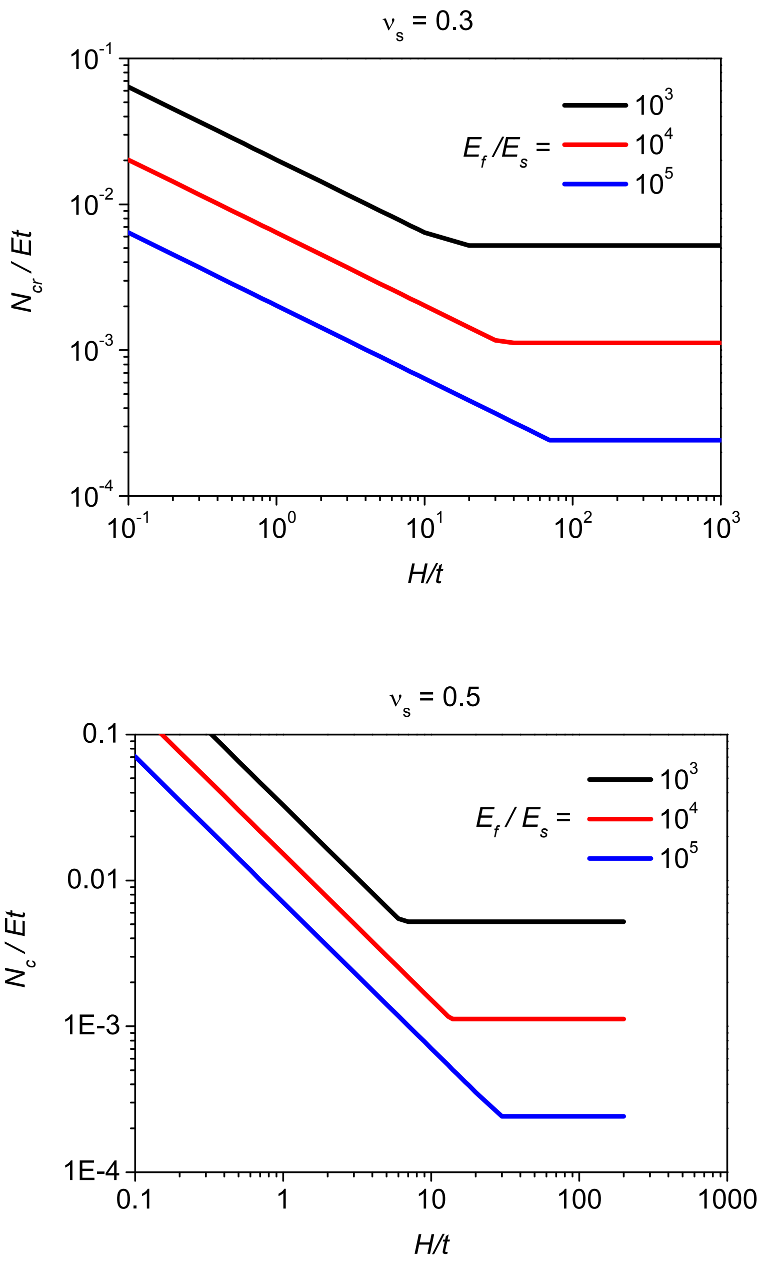

Figure 4-5 Critical membrane force N_{cr}, vs. substrate/film thickness ratio (Huang et al. 2005)

4.5 Post-Buckling Analysis

Figure 4-6 shows a simplified illustration of the fabrication procedure of a single crystalline silicon ribbon system. The details of the fabrication procedure are described in Chapter Two, but only two of these steps are important from a mechanical perspective and they control the stretchability of silicon ribbon system. The first step involves silicon ribbon being bonded on pre-strained substrate, and the second step involves a buckling of the silicon ribbon when releasing the pre-strained substrate to form a wrinkle pattern.

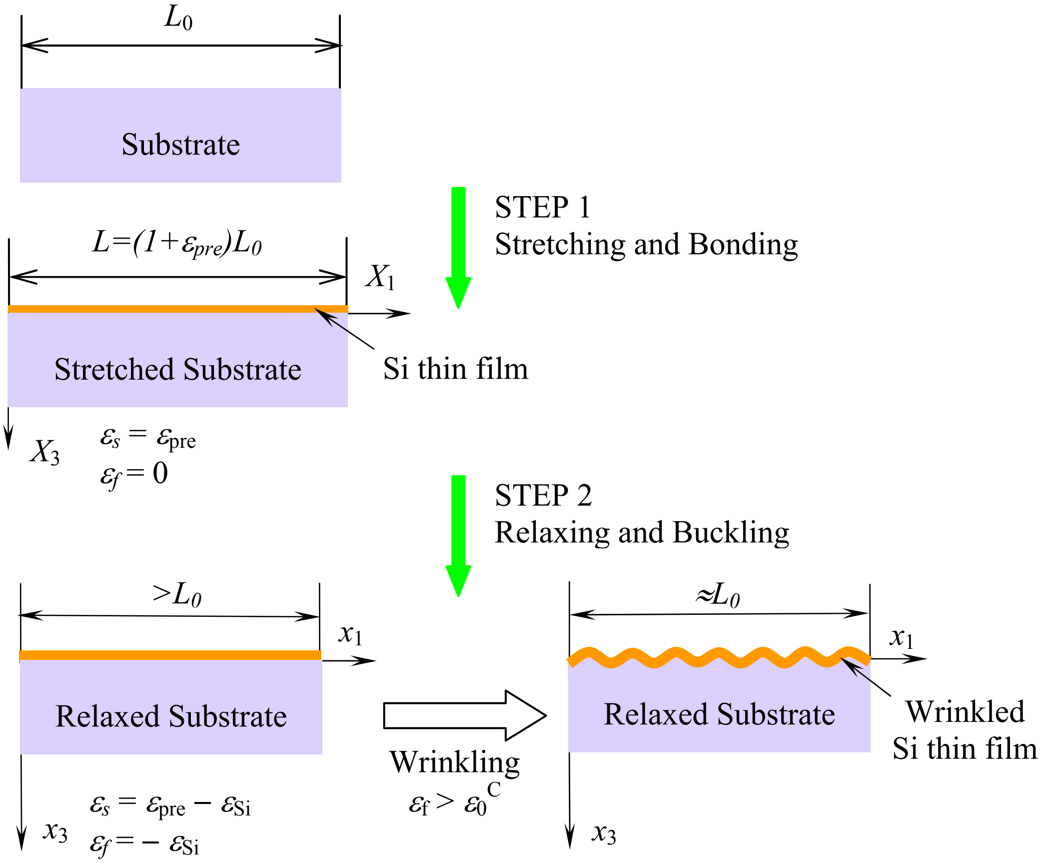

Figure 4-6 Illustration of fabrication procedures

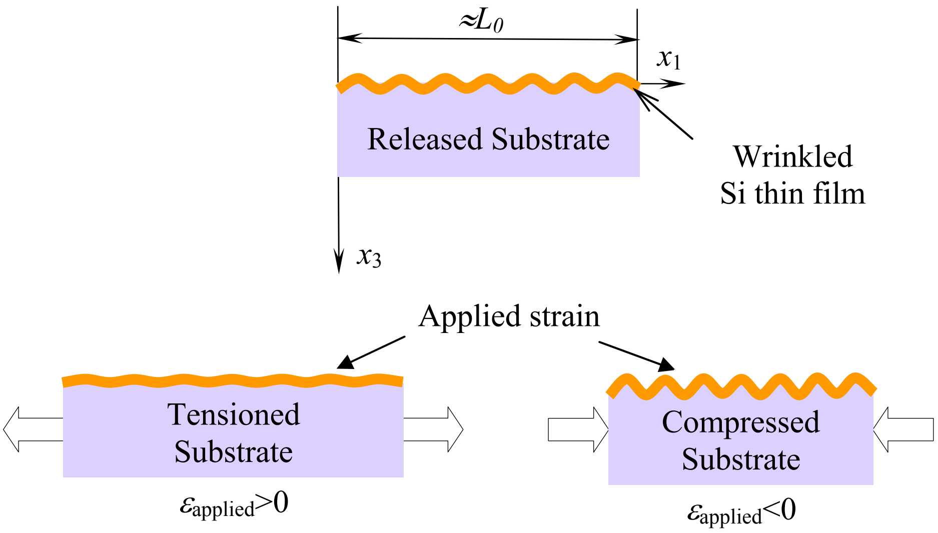

Figure 4-7 Applied strain on wrinkled thin film silicon system

The applied strain is imparted on the wrinkled thin film silicon system to examine the mechanical behavior of the stretchable silicon system after wrinkling (see Figure 4-7). In the experiments, it is observed that amplitude and wavelength of the wrinkled silicon ribbon changes under applied strain. To obtain the quantity of these changes, the analytical method in last section is adopted. Let the deflection of the film be w, and the in-plane displacements be u and v. Base on the experimental observations, a rational expression of displacement is

$$w = A\cos(kx_1) \tag{4-29}$$

$$u = \frac{1}{8}kA^2\sin(2kx_1) + \varepsilon_{applied}x_1 \tag{4-30}$$

$$v = 0 \tag{4-31}$$

Here A is the amplitude and k is the wave number, $\varepsilon_{applied}$ is the uniform strain in the x_1 direction. The components of strain in the middle plane of the film (plate) are

$$\varepsilon_{11} = \frac{1}{4}k^2A^2 + \varepsilon_{applied} \tag{4-32}$$

Because of the existence of pre-strain, ε_{pre}, in the x_1 direction, the strain component in the x_1 direction becomes

$$\varepsilon_{11} = \frac{1}{4}kA^2 + \varepsilon_{applied} + \varepsilon_{pre} \tag{4-33}$$

The constitutive relations give the membrane force in terms of strain, i.e.

$$N_{11} = t\overline{E}_f\varepsilon_{11} = t\overline{E}_f\frac{1}{4}k^2A^2 + t\overline{E}_f\varepsilon_{applied} + N_{11}^0 \tag{4-34}$$

The membrane energy in the film is

$$\begin{aligned} U^m &= \frac{1}{2}N_{11}\varepsilon_{11} \\ &= U^0 + \frac{1}{4}N_{11}^0k^2A^2 + \frac{1}{32}t\overline{E}_fk^2A^2 + N_{11}^0\varepsilon_{applied} + \frac{1}{4}t\overline{E}_fk^2A^2\varepsilon_{applied} + \frac{1}{2}t\overline{E}_f\varepsilon_{applied}^2 \end{aligned} \tag{4-35}$$

where $U^0 = \frac{1}{2}N_{11}^0\varepsilon_{pre}$. Here the equations of Huang (2005) are adopted as shown by equations (4-19) and (4-20). The bending energy in the film is same Equation (4-19)

$$U^b = \frac{1}{48}t^3\overline{E}_fk^4A^2 \tag{4-36}$$

the energy in the substrate is

$$U^s = \frac{1}{8}\overline{E}_skA^2 \tag{4-37}$$

since only the semi-infinite case is studied, from Equation (4-21) and $g = \frac{1}{2}$, the total energy of the stiff thin film-compliant substrate system is

$$\begin{aligned} U &= U^m + U^b + U^s \\ &= U^0 + (\frac{1}{4}N_{11}^0 + \frac{1}{48}t^3\overline{E}_fk^2 + \frac{1}{8}\overline{E}_s)k^2A^2 + N_{11}^0\varepsilon_{applied} + \\ &\frac{1}{32}t\overline{E}_fk^4A^4\varepsilon_{applied} + \frac{1}{4}t\overline{E}_fk^2A^2\varepsilon_{applied} + \frac{1}{2}t\overline{E}_f\varepsilon_{applied}^2 \end{aligned} \tag{4-38}$$

denote

$$\frac{1}{4}N_{11}^0+\frac{1}{48}t^3\overline{E}_f k^2+\frac{1}{8k}\overline{E}_s=\frac{1}{4}N_{11}^0+\frac{1}{48}t\overline{E}_f F \qquad (4\text{-}39)$$

where

$$F=\frac{1}{32}(tk)^2+\frac{1}{2tk}\frac{\overline{E}_s}{\overline{E}_f} \qquad (4\text{-}40)$$

The pre-strain is compressive, and therefore, $N_{11}^0<0$. Rewriting equation (4-38), strain energy in this system is

$$\begin{aligned}U=U^0+\frac{1}{4}(t\overline{E}_f F-\left|N_{11}^0\right|)k^2A^2+\frac{1}{32}t\overline{E}_f k^4A^4 \\ +N_{11}^0\varepsilon_{applied}+\frac{1}{4}t\overline{E}_f k^2A^2\varepsilon_{applied}+\frac{1}{2}t\overline{E}_f\varepsilon_{applied}^2\end{aligned} \qquad (4\text{-}41)$$

If one assumes that $\varepsilon_{applied}$ =0, and $\left|N_{11}^0\right|>t\overline{E}_f F$, then the original flat thin film will be wavy, i.e. the thin film buckled. So here define the critical buckling stress σ_{cr}, and critical strain ε_{cr},

$$\sigma_{cr}=\overline{E}_f F \qquad (4\text{-}42)$$

$$\varepsilon_{cr}=\sigma_{cr}/\overline{E}_f=F \qquad (4\text{-}43)$$

In the following post buckling study, $\left|N_{11}^0\right|>t\sigma_{cr}$ is considered.

For a given strain $\varepsilon_{applied}$, A and k are obtained from the conditions that the strain energy U is a minimum; hence

$$\frac{\partial U}{\partial A}=0 \qquad (4\text{-}44)$$

$$\frac{\partial U}{\partial k}=0 \qquad (4\text{-}45)$$

From (4-44),

$$\frac{\partial U}{\partial A}=\frac{1}{2}(t\sigma-\left|N_{11}^{0}\right|)k^{2}A+\frac{1}{8}t\overline{E}_{f}k^{4}A^{3}+\frac{1}{2}t\overline{E}_{f}k^{2}A\varepsilon_{applied}=0$$

and the amplitude

$$A=\frac{2}{k}(|\,\varepsilon_{pre}\,|-\varepsilon_{c}-\varepsilon_{applied})^{1/2} \tag{4-46}$$

decreases with tension and increases with compression. For $\varepsilon_{applied}=0$, the initial amplitude is

$$A_{0}=\frac{2}{k}(|\,\varepsilon_{pre}\,|-\varepsilon_{c})^{1/2} \tag{4-47}$$

Upon substituting (4-46) into (4-41), the total energy can be written as a function of the wave number, that is,

$$\begin{aligned}U&=U^{0}+\frac{1}{4}(t\overline{E}_{f}\varepsilon_{c}-t\overline{E}_{f}\left|\varepsilon_{pre}\right|)k^{2}\frac{4}{k^{2}}(\varepsilon_{pre}-\varepsilon_{c}-\varepsilon_{applied})\\&\quad+\frac{1}{32}t\overline{E}_{f}k^{4}\frac{16}{k^{4}}(\varepsilon_{pre}-\varepsilon_{c}-\varepsilon_{applied})^{2}+N_{11}^{0}\varepsilon_{applied}\\&\quad+\frac{1}{4}t\overline{E}_{f}k^{2}\frac{4}{k^{2}}(\varepsilon_{pre}-\varepsilon_{c}-\varepsilon_{applied})\varepsilon_{applied}+\frac{1}{2}t\overline{E}_{f}\varepsilon_{applied}^{2}\\&=U^{0}-\frac{1}{2}t\overline{E}_{f}(\left|\varepsilon_{pre}\right|-\varepsilon_{c})^{2}+t\overline{E}_{f}(\left|\varepsilon_{pre}\right|-\varepsilon_{c})\varepsilon_{applied}+N_{11}^{0}\varepsilon_{applied}\end{aligned} \tag{4-48}$$

From Equation (4-45), we can obtain

$$\begin{aligned}\frac{\partial U}{\partial k}&=\frac{\partial U}{\partial\varepsilon_{cr}}\frac{\partial\varepsilon_{cr}}{\partial k}\\&=\left[t\overline{E}_{f}(\left|\varepsilon_{pre}\right|-\varepsilon_{cr})-t\overline{E}_{f}\varepsilon_{applied}\right]\frac{\partial\varepsilon_{cr}}{\partial k}\\&=\left[\left|N_{11}^{0}\right|-t\sigma_{c}-t\overline{E}_{f}\varepsilon_{applied}\right]\frac{\partial\varepsilon_{cr}}{\partial k}\end{aligned}$$

Hence $\frac{\partial\varepsilon_{cr}}{\partial k}=0$, which leads to

$$k=\frac{1}{3}\left(\frac{3\overline{E}_{s}}{\overline{E}_{f}}\right)^{1/3} \tag{4-49}$$

Thus the wave number k does not depend on loading, and is equal to the initial wave number k_0

$$k_0 = \frac{1}{3}\left(\frac{3\overline{E}_s}{\overline{E}_f}\right)^{1/3} \tag{4-50}$$

At equilibrium, with amplitude A and wavelength k, the critical strain

$$\varepsilon_{cr}\frac{\sigma_{cr}}{\overline{E}_f} = \frac{1}{4}\left(\frac{3\overline{E}_s}{\overline{E}_f}\right)^{2/3} = \frac{1}{4}t^2k^2 \tag{4-51}$$

The wavelength λ and initial wavelength λ_0 are

$$\lambda = \lambda_0 = 2\pi t\left(\frac{\overline{E}_f}{3\overline{E}_s}\right)^{1/3} = \frac{\pi t}{\sqrt{\varepsilon_{cr}}} \tag{4-52}$$

The initial amplitude is

$$A_0 = \frac{2}{k}(|\varepsilon_{pre}| - \varepsilon_{cr})^{1/2} = t\left(\frac{|\varepsilon_{pre}|}{\varepsilon_{cr}} - 1\right)^{1/2} \tag{4-53}$$

and the amplitude after applied strain is

$$A = \frac{2}{k}(|\varepsilon_{pre}| - \varepsilon_{cr} - \varepsilon_{applied})^{1/2} = t\left(\frac{|\varepsilon_{pre}| - \varepsilon_{applied}}{\varepsilon_{cr}} - 1\right)^{1/2} \tag{4-54}$$

When a wrinkled film remains bonded to a compliant substrate, the critical membrane force depends on the modulus of the substrate (Allen, 1969). When the critical strain condition is satisfied, as observed experimentally, the bonded film wrinkles into wavy patterns but the wavelength of the individual wrinkles remains practically unchanged as the amplitude of the wrinkles increases (Ohzono and Shimomura, 2005).

This simple criterion (Equation 4-51) is very useful in the design of stretchable silicon against failure. It is, unfortunately, limited to the simple geometry shown in

Figure 4-6. For the wider applications of functional stretchable electronics, it is necessary to design stretchable silicon with complex geometries subject to complex loading (e.g. biaxial stretching). It is important to study these new deformation patterns and establish the corresponding failure criteria for the design of stretchable electronics.

For example, for the simple geometry shown in Figure 4-6, a mechanical analysis (Khang et al., 2006) gives the maximum strain in the silicon ribbon in terms of the applied strain $\varepsilon_f^{peak} = 2\varepsilon_{cr}\left(\frac{\varepsilon_{pre} - \varepsilon_{applied}}{\varepsilon_{cr}} - 1\right)^{1/2}$, where ε_{pre} is the prestrain, $\varepsilon_{cr} = 0.52\left[\frac{E_s(1-\nu_f^2)}{E_f(1-\nu_s^2)}\right]^{2/3}$ is the critical strain for buckling, and E and ν are Young's modulus and Poisson's ratio (of PDMS and Si). This criterion shows that the maximum strain in silicon ribbons is independent of the silicon ribbon thickness, and is controlled by the elastic properties as well as the applied strain and pre-strain. It is useful to define the range of the applied strain that the system can sustain without fracturing the silicon. For a prestrain of 0.9%, this range is -27% to 2.9% assuming that the silicon failure strain is ~2% (for either compression or tension). Controlling the level of prestrain allows this range of strain to balance desired degrees of compressive and tensile deformability. For example, a prestrain of 3.5% (the maximum in experiment) yields a range of -24% to 5.5%.

The linear analytical models derived here can explain experimental observations at a quantitative level. These results have relevance to the many useful applications of controlled buckling structures in stretchable stiff thin film-compliant substrate system. The analytical solutions show the critical strain for buckling and the wrinkling amplitude and wavelength increase with the prestrain. Figure 4-8 shows the analytical results agree reasonably well with experimental results at small prestrain (Khang, et al., 2006) and therefore the analytical solutions provides valuable guide to the precise design and control of the buckling profile in stiff thin film-compliant substrate system.

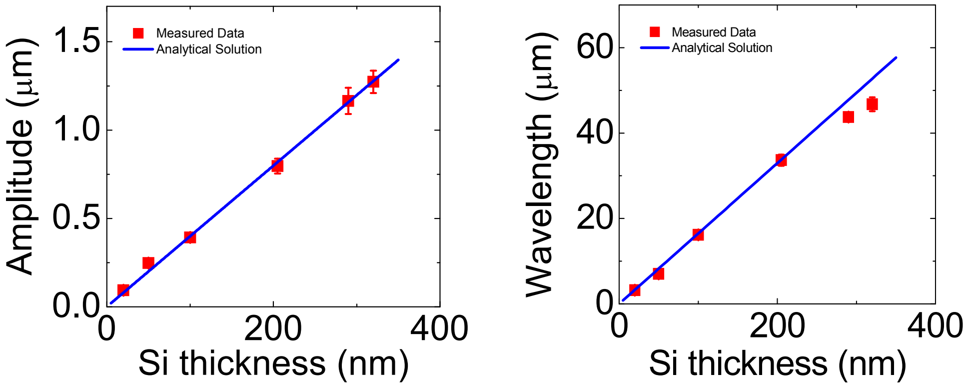

Figure 4-8 Comparison of experimental data and linear analytical prediction of wavelength and amplitude of wavy silicon at prestrain=0.9%.

Chapter Five

Non-Linear Analytical Study for Single Crystal Silicon

The wavelength and amplitude of wrinkled film under prestrain and applied strain can be computed based on the analytical solution procedure presented in Chapter Four. Equation (4-52) shows that the wavelength the buckled Si ribbons (100 nm thickness) on PDMS is constant with varying prestrain (this is true also for the applied strain), but the experiments (Khang et al., 2006; Jiang et al., 2007) indicate qualitatively a different characteristic behavior, i.e. a clear and systematic decrease in wavelength with increasing prestrain, as shown in Figure 5-1. In addition, the amplitude of the experimental data decreases more rapidly than the theoretical prediction when prestrain is increased more (Equation 4-54), especially at large strain values as shown in Figure 5-2. This strain dependent behavior has also been reported for layers of polystyrene (PS) on PDMS substrates when the prestrain varies from ~0% to 10% (Harrison et al., 2004), and in platinum films on rubber substrates for prestrains of ~400% (Volynskii et al., 2000; Jiang et al., 2007) indicate that strain dependent wavelength is due to the finite deformation (i.e. large strain) in the compliant substrate.

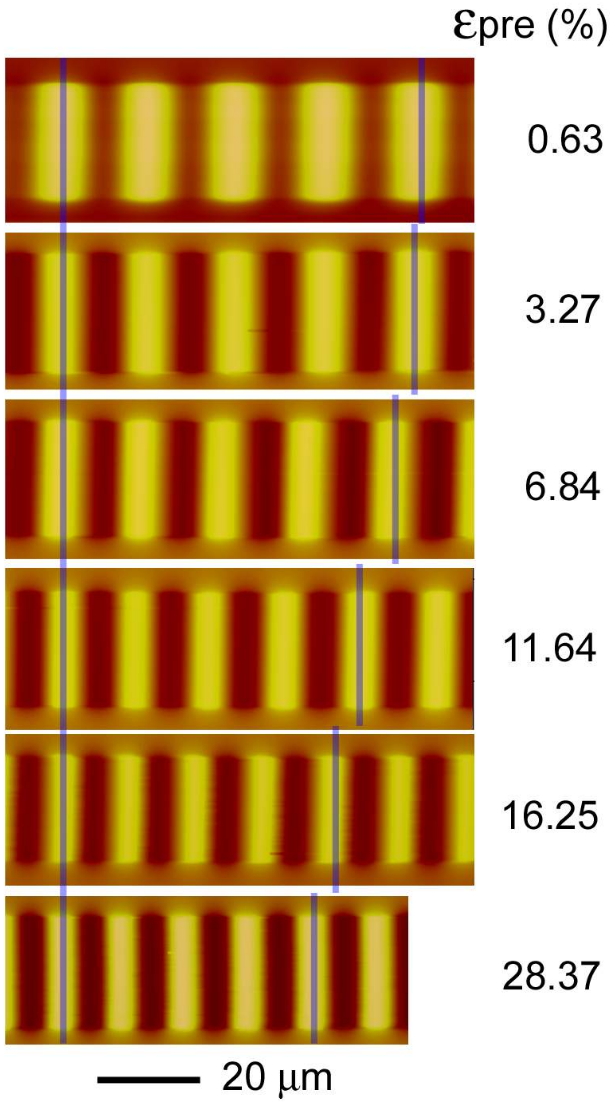

Figure 5-1 Optical micrographs of buckled Si ribbons on PDMS formed with various prestrains (indicated on the right, as percentages)

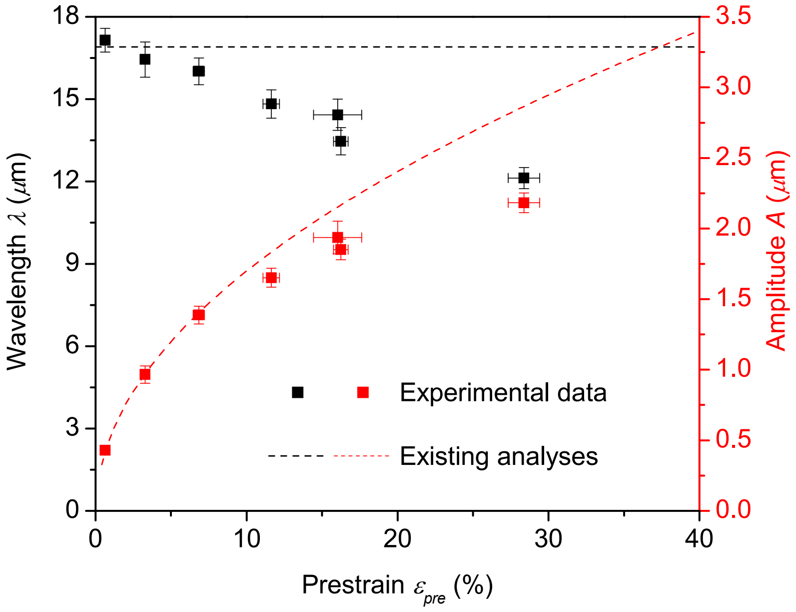

Figure 5-2 Comparison of experimental data and linear analytical prediction of wavelength and amplitude of wavy silicon.

The analysis here focuses on the buckling of the stiff thin film-compliant substrate system illustrated in Figure 5-3, although the linear theoretical considerations apply to all related systems in which buckling occurs. The new analytical model for buckling will account for finite deformations and geometrical nonlinearities to yield a quantitatively more accurate description of the system. The effects of nonlinearities at large prestrain values will be included, i.e. (1) different initial strain-free configurations for the thin film and substrate, (2) the nonlinear strain-displacement relation in the substrate, and (3) the nonlinear Neo-Hookean constitutive law for the substrate. The analytical solution will be obtained via the perturbation method, and will be verified by experimental data and numerical analysis.

5.1 *Finite Deformation Buckling Analysis*

The analysis presented in this chapter is different from the linear buckling analyses in the following three aspects: (1) geometrical configurations change, (2) finite strain, and (3) the use of nonlinear constitutive model.

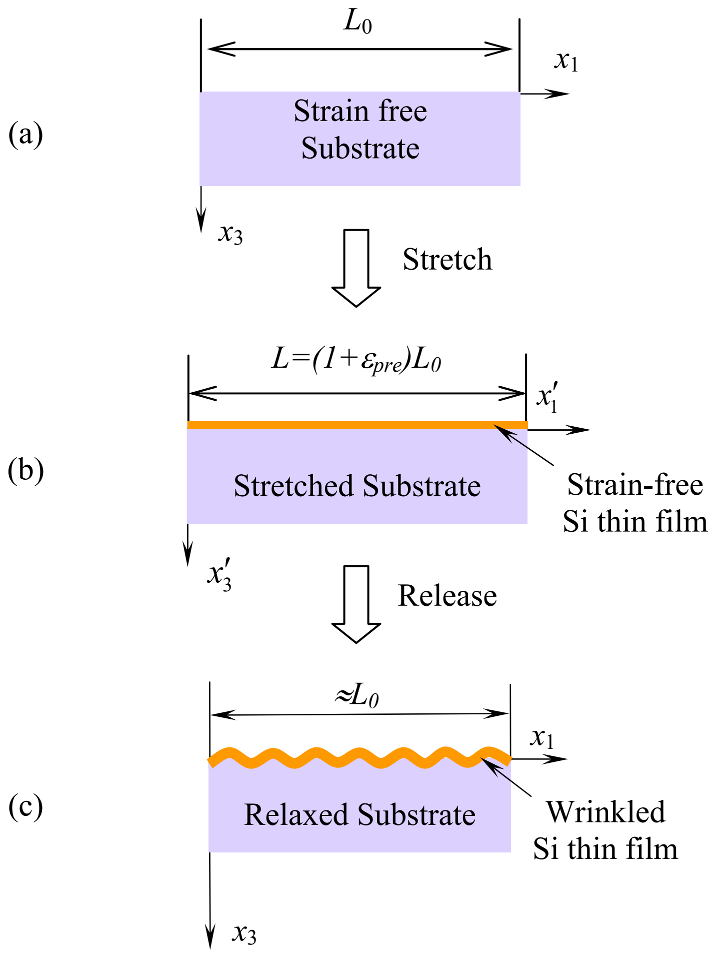

Figure 5-3 Fabrication process of stiff thin film-compliant substrate system

Figure 5-3 illustrates the controlled buckling shown initially in Figure 2-2 of Chapter 2: (a) the upper figure shows the initial, strain-free state of the PDMS before stretching at the original length L_0, (b) the middle figure shows the stretched PDMS attached to a strain-free Si thin film, where the length of the PDMS approaches

$(1+\varepsilon_{pre})L_0$, which is also the original length of the Si film, and ε_{pre} is the prestrain in the stretched PDMS, and (c) the lower figure shows a release of the prestrain which buckles the Si film. The coordinate x_1' in the middle figure is related to x_1 in the top figure by the transformation $x_1' = (1+\varepsilon_{pre})x_1$.

(1) Geometrical configuration change

The initial strain-free (or stress-free) states are different for the PDMS substrate and Si thin film. The Si thin film, as illustrated in Figure 5-3, is strain free in the upper (a) configuration, but becomes compressed in the lower (c) configuration. On the other hand, the PDMS substrate is stretched and relaxed in the upper (a) and lower (c) configurations, respectively.

(2) Finite strain analysis

The maximum prestrain could reach up to 28% (Jiang et al., 2007) when the PDMS substrate is stretched in the experiments. Thus, the strain-displacement relation in the PDMS substrate becomes nonlinear. Finite deformation theory should be applied in the analysis.

(3) Nonlinear Constitutive Model

The stress-strain relation will not remain linear when the deformation becomes large in the PDMS substrate. The nonlinear constitutive law should be applied for the substrate.

5.1.1 Thin Film

The thin film can be modeled as a beam since the wavelength $(\lambda = 15\mu\text{m})$ in the film direction, x_1, is much larger than the film thickness (0.1μm). The beam undergoes large rotation once the film buckles. The membrane strain ε_{11} is related to the in-plane displacement u_1 and out-of-plane displacement w by

$$\varepsilon_{11} = \frac{du_1}{dx_1} + \frac{1}{2}\left(\frac{dw}{dx_1}\right)^2 \tag{5-1}$$

where x_1' is the coordinate for the strain-free configuration of the film (middle figure, Figure 5-3). Jiang, et al. (2008) obtained the analytical solution for the stiff thin film of finite width on a compliant substrate. For a film width of 20 μm as in the experiments, the wavelength and amplitude given by the analytical solution for finite width are only a few per cents different from the present results based on the plane-strain analysis (Jiang, et al. 2008). Since the film width (in the direction normal to x_1' and x_3') is much larger than the film thickness, the deformation is assumed to be plane strain. The strain ε_{11} in the film is so small that the membrane force N_{11} may be related to ε_{11} via the plane-strain modulus $\overline{E}_f$ of the film,

$$N_{11} = \overline{E}_f t \varepsilon_{11} \tag{5-2}$$

The force equilibrium gives the shear and normal tractions at the film and substrate interface as

$$T_1 = \frac{dN_{11}}{dx_1'} \tag{5-3}$$

and

$$T_3 = -\frac{\overline{E}_f t^3}{12}\frac{d^4 w}{dx_1'^4} + \frac{d}{dx_1'}\left(N_{11}\frac{dw}{dx_1}\right) \tag{5-4}$$

respectively.

The strain energy density in the film consists of the membrane energy density,

$$W^m = \frac{1}{2} N_{11} \varepsilon_{11} = \frac{\overline{E}_f h_f}{2} \varepsilon_{11}^2 \tag{5-5}$$

and the bending energy density,

$$W^b = \frac{\overline{E}_f h_f^3}{24} \left(\frac{d^2 w}{dx_1'^2} \right)^2 \tag{5-6}$$

5.1.2 Substrate

The substrate is modeled as a semi-infinite solid. The displacements in the substrate are denoted by $u_1(x_1, x_3)$ and $u_3(x_1, x_3)$, where x_1 and x_3 are the coordinates for the strain-free configuration of the PDMS substrate (Figure 5-3 (a)). For large deformation in substrate, the Green strains E_{IJ} in the substrate are related to the displacements as follows

$$E_{IJ} = \frac{1}{2} \left(\frac{\partial u_I}{\partial x_J} + \frac{\partial u_J}{\partial x_I} + \frac{\partial u_K}{\partial x_I} \frac{\partial u_K}{\partial x_J} \right) \tag{5-7}$$

where $I = 1$ and 3 and $J = 1$ and 3 for this 2D problem.

The Neo-Hookean constitutive law (Symon, 1971), which is the simplest nonlinear elastic constitutive relation, is used to represent the substrate

$$T_{IJ} = \frac{\partial W_s}{\partial E_{IJ}} \tag{5-8}$$

where T_{IJ} is the 2nd Piola-Kirchoff stress, and the strain energy density W^s in substrate is of the form

$$W^s = \frac{E_s}{6(1-2\nu_s)}(J-1)^2 + \frac{E_s}{4(1+\nu_s)}(\bar{I}_1 - 3)$$

here J is the volume change at a point and is the determinant of the deformation gradient F_{iJ} , $\bar{I}_1$ is the trace of the left Cauchy-Green strain tensor $B_{IJ} = F_{IK}F_{JK}$ multiplied by $J^{-2/3}$, E_s and ν_s are the Young's modulus and Poisson's ratio of the substrate, respectively, E_s=1.8 MPa and ν_s=0.48 for PDMS (Wilder et al., 2006, INSPEC, 1988).

The 2D force equilibrium equation for finite deformation is

$$\begin{cases} \dfrac{\partial T_{11}F_{11}}{\partial x_1} + \dfrac{\partial T_{13}F_{13}}{\partial x_1} + \dfrac{\partial T_{31}F_{11}}{\partial x_3} + \dfrac{\partial T_{33}F_{13}}{\partial x_3} = 0 \\ \dfrac{\partial T_{11}F_{31}}{\partial x_1} + \dfrac{\partial T_{13}F_{33}}{\partial x_1} + \dfrac{\partial T_{31}F_{31}}{\partial x_3} + \dfrac{\partial T_{33}F_{33}}{\partial x_3} = 0 \end{cases} \tag{5-9}$$

and the traction on the surface is $T_i = F_{iK}F_{JK}n_J$, where n_J is the unit normal vector of the surface.

5.1.3 Buckling Analysis

The out-of-plane displacement w of the buckled thin film can be represented by

$$w = A\cos\left(\frac{2\pi x_1}{\lambda}\right) = A\cos\left[\frac{2\pi x_1'}{(1+\varepsilon_{pre})\lambda}\right] \tag{5-10}$$

in the strain-free configuration (Figure 5-3b) as well as in the relaxed configuration (Figure 5-3c). Here the amplitude A and wavelength λ are to be determined.

The bending energy density W^b can be obtained from Equation (5-6). The bending energy U^b is the integral of W^b over the length of strain-free thin film, $L = (1+\varepsilon_{pre})L_0$ (Figure 5-3 (b)), where L_0 is the length of the strain-free PDMS substrate (Figure 5-3 (a)). Hence the bending energy is

$$U^b = \frac{\pi^4}{3} \frac{\overline{E}_f t^3 A^2}{\left[(1+\varepsilon_{pre})\lambda\right]^4}(1+\varepsilon_{pre})L_0 \tag{5-11}$$

The effect of interface shear is negligibly small on the buckling of the stiff thin film-compliant substrate system (Huang et al., 2005). The vanishing shear $T_1 = 0$ in Equation (5-3) results in the in-plane displacement

$$u_1 = \frac{\pi A^2}{4(1+\varepsilon_{pre})\lambda}\sin\left[\frac{4\pi x_1'}{(1+\varepsilon_{pre})\lambda}\right] - \frac{\varepsilon_{pre}}{(1+\varepsilon_{pre})}x_1' \tag{5-12}$$

where the second term on the right hand side represents the uniform displacement field in the film if the film does not buckle after the prestretched PDMS is relaxed, and the first term on the right hand side is the axial displacement associated with the buckling.

The membrane strain is

$$\varepsilon_{11} = \frac{\pi^2 A^2}{(1+\varepsilon_{pre})^2\lambda^2} - \frac{\varepsilon_{pre}}{1+\varepsilon_{pre}} \tag{5-13}$$

from which the membrane energy density W^m can be obtained via Equation (5-5). The membrane energy U^m is the integral of W^m over the length of strain-free thin film and is of the form

$$U^m = \frac{1}{2}\overline{E}_f t\left[\frac{\pi^2 A^2}{(1+\varepsilon_{pre})^2\lambda^2} - \frac{\varepsilon_{pre}}{1+\varepsilon_{pre}}\right]^2(1+\varepsilon_{pre})L_0 \tag{5-14}$$

where $L = (1+\varepsilon_{pre})L_0$ is the length of the strain-free thin film (Figure 5-3b).

The strain energy density in the substrate is a function of positions x_1 and x_3, as well as the amplitude A and wavelength λ of wrinkled film and substrate. Its integral over the substrate volume gives the strain energy in the substrate

$$U^s = U^s(A, \lambda) \tag{5-15}$$

where U^s is proportional to L_0. The amplitude A and wavelength λ are then determined by minimizing the total energy,

$$\frac{\partial}{\partial A}(U^m + U^b + U^s) = \frac{\partial}{\partial \lambda}(U^m + U^b + U^s) = 0\,. \tag{5-16}$$

5.2 Perturbation Analysis of Substrate

The deformation is highly nonlinear due to large prestrain in the substrate. Since the amplitude A is much smaller than the wavelength λ, a perturbation method is used to expand the displacement field via the power series of the parameter $\delta = A/\lambda$, i.e.

$$\begin{cases} u_1(x_1, x_3) = A(u_1^{(0)} + \delta u_1^{(1)}) + \delta u_1^{(2)}) + \cdots) \\ u_3(x_1, x_3) = A(u_3^{(0)} + \delta u_3^{(1)}) + \delta u_3^{(2)}) + \cdots) \end{cases} \tag{5-17}$$

where $u_1^{(i)}$ and $u_3^{(i)}$ are the i^{th} order, non-dimensional functions to be determined. The Green strain can be similarly expanded as follows

$$E_{IJ} = A(E_{IJ}^{(0)} + \delta E_{IJ}^{(0)} + E_{IJ}^{(0)} + \cdots) \tag{5-18}$$

where $E_{IJ}^{(i)}$ is related to $u_1^{(i)}$ and $u_3^{(i)}$ via Equation (5-7) as

$$E_{IJ}^{(0)} = \frac{1}{2}\left(\frac{\partial u_I^{(0)}}{\partial x_J} + \frac{\partial u_J^{(0)}}{\partial x_I}\right) + \frac{A}{2}\frac{\partial u_K^{(0)}}{\partial x_I}\frac{\partial u_K^{(0)}}{\partial x_J}$$

$$E_{IJ}^{(1)} = \frac{1}{2}\left(\frac{\partial u_I^{(1)}}{\partial x_J} + \frac{\partial u_J^{(1)}}{\partial x_I}\right) + \frac{A}{2}\left(\frac{\partial u_K^{(0)}}{\partial x_I}\frac{\partial u_K^{(1)}}{\partial x_J} + \frac{\partial u_K^{(0)}}{\partial x_J}\frac{\partial u_K^{(1)}}{\partial x_I}\right) \tag{5-19}$$

$$E_{IJ}^{(2)} = \frac{1}{2}\left(\frac{\partial u_I^{(2)}}{\partial x_J} + \frac{\partial u_J^{(2)}}{\partial x_I}\right) + \frac{A}{2}\left(\frac{\partial u_K^{(0)}}{\partial x_I}\frac{\partial u_K^{(2)}}{\partial x_J} + \frac{\partial u_K^{(0)}}{\partial x_J}\frac{\partial u_K^{(2)}}{\partial x_I} + \frac{\partial u_K^{(1)}}{\partial x_I}\frac{\partial u_K^{(1)}}{\partial x_J}\right)$$

The 2nd Piola-Kirchoff stress T_{IJ} can be obtained from the expansion of the constitutive law (Equation 5-8) as follows

$$\begin{aligned}
T_{11} &= \frac{E_s}{6(1-2\nu_s)}\begin{pmatrix} 2E_{11} + 2E_{33} + 2E_{11}E_{33} - 3E_{11}^2 - 4E_{13}^2 - E_{33}^2 \\ + 4E_{13}^2E_{33} + 12E_{11}E_{13}^2 - 3E_{11}^2E_{33} - E_{11}E_{33}^2 + 5E_{11}^3 - E_{33}^3 \end{pmatrix} \\
&\quad + \frac{E_s}{1+\nu_s}\begin{pmatrix} \frac{2}{3}E_{11} - \frac{2}{3}E_{33} + \frac{4}{9}E_{11}E_{33} - \frac{16}{9}E_{11}^2 - 2E_{13}^2 - \frac{2}{9}E_{33}^2 \\ + \frac{32}{9}E_{13}^2E_{33} + \frac{80}{9}E_{11}E_{13}^2 - \frac{8}{9}E_{11}^2E_{33} + \frac{112}{27}E_{11}^3 - \frac{8}{27}E_{33}^3 \end{pmatrix} \\
T_{33} &= \frac{E_s}{6(1-2\nu_s)}\begin{pmatrix} 2E_{11} + 2E_{33} + 2E_{11}E_{33} - 3E_{33}^2 - 4E_{13}^2 - E_{11}^2 \\ + 4E_{13}^2E_{33} + 12E_{33}E_{13}^2 - 3E_{33}^2E_{11} - E_{33}E_{11}^2 + 5E_{33}^3 - E_{11}^3 \end{pmatrix} \\
&\quad + \frac{E_s}{1+\nu_s}\begin{pmatrix} \frac{2}{3}E_{33} - \frac{1}{3}E_{11} + \frac{4}{9}E_{11}E_{33} - \frac{16}{9}E_{33}^2 - 2E_{13}^2 - \frac{2}{9}E_{11}^2 \\ + \frac{32}{9}E_{13}^2E_{11} + \frac{80}{9}E_{33}E_{13}^2 - \frac{8}{9}E_{33}^2E_{11} + \frac{112}{27}E_{33}^3 - \frac{8}{27}E_{11}^3 \end{pmatrix} \\
T_{13} &= \frac{E_s}{3(1-2\nu_s)}\left(-2E_{11}E_{33} - 2E_{13}E_{33} + 3E_{11}^2E_{13} + 3E_{13}E_{33}^2 + 2E_{11}E_{13}E_{33} + 4E_{13}^3\right) \\
&\quad + \frac{E_s}{1+\nu_s}\left(E_{13} - 2E_{11}E_{13} - 2E_{13}E_{33} + \frac{40}{9}E_{11}^2E_{13} + \frac{40}{9}E_{13}E_{33}^2 + \frac{32}{9}E_{11}E_{13}E_{33} + \frac{16}{3}E_{33}^3\right)
\end{aligned} \tag{5-20}$$

The deformation gradient can be expanded into its terms as

$$\begin{aligned}
F_{11} &= 1 + \frac{\partial u_1}{\partial x_1} = 1 + A\left[\frac{\partial u_1^{(0)}}{\partial x_1} + \delta\frac{\partial u_1^{(1)}}{\partial x_1} + \delta^2\frac{\partial u_1^{(2)}}{\partial x_1} + \cdots\right] \\
F_{13} &= \frac{\partial u_1}{\partial x_3} = A\left[\frac{\partial u_1^{(0)}}{\partial x_3} + \delta\frac{\partial u_1^{(1)}}{\partial x_3} + \delta^2\frac{\partial u_1^{(2)}}{\partial x_3} + \cdots\right] \\
F_{31} &= \frac{\partial u_3}{\partial x_1} = A\left[\frac{\partial u_3^{(0)}}{\partial x_1} + \delta\frac{\partial u_3^{(1)}}{\partial x_1} + \delta^2\frac{\partial u_3^{(2)}}{\partial x_1} + \cdots\right] \\
F_{33} &= 1 + \frac{\partial u_3}{\partial x_3} = 1 + A\left[\frac{\partial u_3^{(0)}}{\partial x_3} + \delta\frac{\partial u_3^{(1)}}{\partial x_3} + \delta^2\frac{\partial u_3^{(2)}}{\partial x_3} + \cdots\right]
\end{aligned} \tag{5-21}$$

Substitution of Equations (5-19)-(5-21) into equilibrium equation (5-9) yields the linear ordinary differential equations for $u_i^{(0)}$, $u_i^{(1)}$ and $u_i^{(2)}$. The boundary conditions are

$$\begin{aligned} &T_1 = 0 \text{ and } u_3 = A\cos\left(\frac{2\pi x_1}{\lambda}\right) && \text{at } x_3 = 0 \\ &T_1 = 0 \text{ and } T_3 = 0 && \text{at } x_3 = \infty \end{aligned} \tag{5-22}$$

The displacement fields $u_i^{(0)}$, $u_i^{(1)}$ and $u_i^{(2)}$ are obtained analytically as

$$\begin{cases} u_1^{(0)}\left(x_1,x_3\right) = \dfrac{2\pi}{\lambda} x_3 e^{\frac{-2\pi}{\lambda}x_3} \sin\left(\dfrac{2\pi}{\lambda}x_1\right) \\ u_3^{(0)}\left(x_1,x_3\right) = \left(1+\dfrac{2\pi}{\lambda}x_3\right) e^{\frac{-2\pi}{\lambda}x_3} \cos\left(\dfrac{2\pi}{\lambda}x_1\right) \end{cases} \tag{5-23}$$

$$\begin{cases} u_1^{(1)}\left(x_1,x_3\right) = \left(\dfrac{3\pi}{2\lambda}x_3 - \dfrac{1}{8}\right) e^{\frac{-4\pi}{\lambda}x_3} \sin\left(\dfrac{4\pi}{\lambda}x_1\right) \\ u_3^{(1)}\left(x_1,x_3\right) = -\left(\dfrac{2\pi^2}{\lambda^2}x_3^2 + \dfrac{\pi}{\lambda}x_3\right) e^{\frac{-4\pi}{\lambda}x_3} + \dfrac{3\pi}{2\lambda} x_3 e^{\frac{-4\pi}{\lambda}x_3} \cos\left(\dfrac{4\pi}{\lambda}x_1\right) \end{cases} \tag{5-24}$$

and

$$\begin{cases} u_1^{(2)}\left(x_1,x_3\right) = \left(\dfrac{13\pi}{64\lambda}x_3 - \dfrac{3}{16}\right) e^{\frac{-2\pi}{\lambda}x_3} \sin\left(\dfrac{2\pi}{\lambda}x_1\right) + \dfrac{\pi}{\lambda} x_3 e^{\frac{-6\pi}{\lambda}x_3} \sin\left(\dfrac{6\pi}{\lambda}x_1\right) \\ \qquad -\left(\dfrac{\pi^3}{2\lambda^3}x_3^3 + \dfrac{21\pi^2}{8\lambda^2}x_3^2 + \dfrac{45\pi}{64\lambda}x_3 - \dfrac{5}{16}\right) e^{\frac{-6\pi}{\lambda}x_3} \sin\left(\dfrac{2\pi}{\lambda}x_1\right) \\ u_3^{(2)}\left(x_1,x_3\right) = \left(\dfrac{13\pi}{64\lambda}x_3 - \dfrac{11}{128}\right) e^{\frac{-2\pi}{\lambda}x_3} \cos\left(\dfrac{2\pi}{\lambda}x_1\right) + \dfrac{\pi}{\lambda} x_3 e^{\frac{-6\pi}{\lambda}x_3} \cos\left(\dfrac{6\pi}{\lambda}x_1\right) \\ \qquad +\left(\dfrac{5\pi^3}{2\lambda^3}x_3^3 - \dfrac{29\pi^2}{8\lambda^2}x_3^2 - \dfrac{71\pi}{64\lambda}x_3 + \dfrac{11}{128}\right) e^{\frac{-6\pi}{\lambda}x_3} \cos\left(\dfrac{2\pi}{\lambda}x_1\right) \end{cases} \tag{5-25}$$

Since the substrate is nearly incompressible, Poisson's ratio $\nu_s \approx 0.5$. The strain energy in the substrate can be obtained by integrating the strain energy density W^s to yield

$$U^s = \frac{\pi}{3}\frac{E_s A^2}{\lambda}\left(1 + \frac{5}{32}\frac{\pi^2 A^2}{\lambda^2}\varepsilon_{pre}\right)L_0 \tag{5-26}$$

where L_0 is the original length of the substrate.

5.3 Post-Buckling Analysis

The buckling analysis presented in Section 5.1 and 5.2 is for stiff thin film-compliant substrate system subjected to prestrain. The post-buckling behavior, i.e. the system subjected to the applied strain after buckling, is studied in this section to determine the system stretchability/compressibility. Figure 5-4 illustrates the buckled Si thin film and relaxed PDMS substrate of length L_0 (left figure) and the system that is subjected to the applied strain $\varepsilon_{applied}$ and has the length $\left(1+\varepsilon_{applied}\right)L_0$ (right figure). The coordinate x_1'' in the right figure is related to x_1 in the left figure by $x_1''=\left(1+\varepsilon_{applied}\right)x_1$. The out-of-plane displacement w of the buckled thin film can be represented by

$$w=A''\cos\left(\frac{2\pi x_1''}{\lambda''}\right)=A''\cos\left[\frac{2\pi\left(1+\varepsilon_{applied}\right)x_1}{\lambda''}\right] \tag{5-27}$$

for the relaxed configuration (Figure 5-4 (a)) and stretched configuration (Figure 5-4b). Here the amplitude A'' and wavelength λ'' are to be determined in terms of the applied strain $\varepsilon_{applied}$. In the strain-free configuration x_1' of the thin film (Figure 5-3b), Equation (5-27) is of the form

$$w=A''\cos\left[\frac{2\pi\left(1+\varepsilon_{applied}\right)x_1'}{\left(1+\varepsilon_{PRE}\right)\lambda''}\right] \tag{5-28}$$

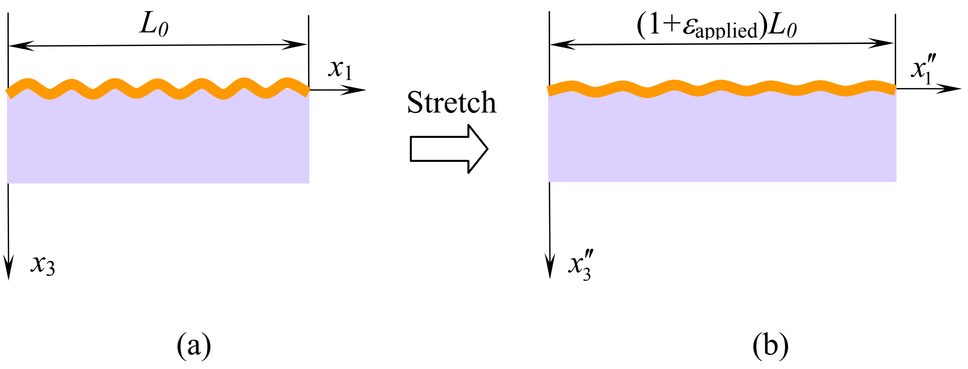

Figure 5-4 Buckled Si thin film and relaxed PDMS substrate of length L_0 (a) and $(1+\varepsilon_{applied})L_0$ (b) under applied strain $\varepsilon_{applied}$

The bending energy in the thin film is given in the following equation:

$$U^b = \frac{\pi^4}{3}\bar{E}_f t^3 A''^2 \left[\frac{1+\varepsilon_{applied}}{(1+\varepsilon_{pre})\lambda''}\right]^4 (1+\varepsilon_{pre})L_0 \tag{5-29}$$

where $\left(1+\varepsilon_{pre}\right)L_0$ is the length of the strain-free thin film (Figure 5-3b).

The vanishing shear $T_1 = 0$ in Equation (5-3) gives the in-plane displacement

$$u_1 = \frac{\pi(1+\varepsilon_{applied})A''^2}{4(1+\varepsilon_{pre})\lambda''}\sin\left[\frac{4\pi(1+\varepsilon_{applied})x_1'}{(1+\varepsilon_{pre})\lambda''}\right] - \frac{\varepsilon_{pre}-\varepsilon_{applied})}{(1+\varepsilon_{pre})}x_1' \tag{5-30}$$

and the membrane energy in the thin film becomes

$$U^m = \frac{1}{2}\bar{E}_f t\left[\left(\frac{1+\varepsilon_{applied}}{1+\varepsilon_{pre}}\right)^2 \frac{\pi^2 A''^2}{\lambda''^2} - \frac{\varepsilon_{pre}-\varepsilon_{applied}}{1+\varepsilon_{pre}}\right]^2 (1+\varepsilon_{pre})L_0 \tag{5-31}$$

where $\left(1+\varepsilon_{pre}\right)L_0$ is the length of the strain-free thin film (Figure 5-3b).

The displacement field in the substrate can be written using the perturbation method, as

$$\begin{cases} u_1\left(x_1,x_3\right)=A''\left[\varepsilon_{applied}\dfrac{x_1}{A''}+u_1^{(0)}+\delta u_1^{(1)}+\delta^2 u_1^{(2)}+\cdots\right] \\ u_3\left(x_1,x_3\right)=A''\left[-\dfrac{\nu_s}{1-\nu_s}\varepsilon_{applied}\dfrac{x_3}{A''}+u_3^{(0)}+\delta u_3^{(1)}+\delta^2 u_3^{(2)}+\cdots\right] \end{cases}, \tag{5-32}$$

where $\delta = A''/\lambda''$ is small value, and $u_1^{(i)}$ and $u_3^{(i)}$ are the i^{th} order, non-dimensional functions to be determined via the same approach as Section 5-2 for the prestrain state. For the nearly incompressible substrate $\nu_s \approx 1/2$, and the strain energy in the substrate can be obtained as

$$U^s = \frac{\pi}{3}\frac{E_s A''^2}{\lambda''}(1+\varepsilon_{applied})\left[1+\varepsilon_{applied}+\frac{5}{32}\frac{\pi^2 A''^2}{\lambda''^2}(1+\varepsilon_{applied})^2\right]L_0 \tag{5-33}$$

5.4 Results and Discussion

The wavelength and amplitude of wrinkled stiff thin film-compliant substrate system can be obtained using virtual work principle.

5.4.1 Wavelength and Amplitude due to Prestrain

The total energy consists of the membrane and bending energy in the thin film and the strain energy in the substrate, i.e. $U = U^m + U^b + U^s$. Minimization of the total energy, i.e. $\dfrac{\partial U}{\partial A} = \dfrac{\partial U}{\partial \lambda} = 0$ gives the wavelength and amplitude

$$A = t\frac{\left(\dfrac{\varepsilon_{pre}}{\varepsilon_c} - \dfrac{1+\dfrac{\xi}{3}}{\left(1+\xi\right)^{1/3}}(1+\varepsilon_{pre})\right)^{1/2}}{(1+\varepsilon_{pre})^{1/2}\left(1+\xi\right)^{1/3}} \tag{5-34}$$

For $\varepsilon_{pre} >> \varepsilon_{cr}$, the numerator is approximately $\left(\frac{\varepsilon_{pre}}{\varepsilon_{cr}} - 1\right)^{1/2}$, which yields the amplitude in Equation (5-35)

$$A \approx \frac{A_0}{(1+\varepsilon_{pre})^{1/2}(1+\xi)^{1/3}} \text{ and } \lambda \approx \frac{\lambda_0}{(1+\varepsilon_{pre})(1+\xi)^{1/3}} \tag{5-35}$$

where $\lambda_0 = 2\pi t(\overline{E}_f / 3\overline{E}_s)^{1/3}$ and $A_0 = t(\varepsilon_{pre}/\varepsilon_{cr} - 1)^{1/2}$ are the wavelength and amplitude based on small deformation theory respectively, and $\xi = 5\varepsilon_{pre}(1+\varepsilon_{pre})/32$. As in the previous analyses, finite deformation theory predicts non zero amplitude when the prestrain, ε_{pre} exceeds the critical strain, ε_{cr}. However, the wavelength is different from that given by previous theories due to the large prestrain. Figure 5-5 shows the comparison for (a) wavelength and (b) amplitude of buckled structures for Si (100 nm thickness) on PDMS as a function of the prestrain. It can be seen from this figure that the wavelength depends on the prestrain, and the results agree well with experimental data and the results based on the numerical method (FEM) without any parameter fitting. The numerical method will be explained in Chapter Six. For small prestrain, λ approaches λ_0.

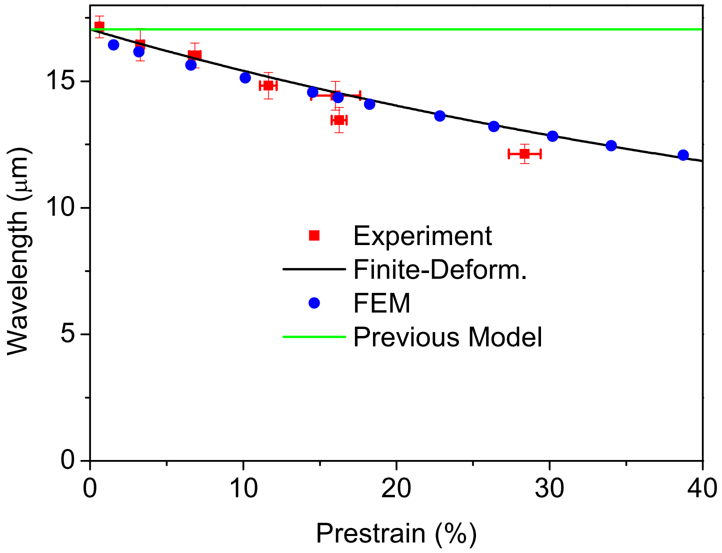

(a) Wavelength

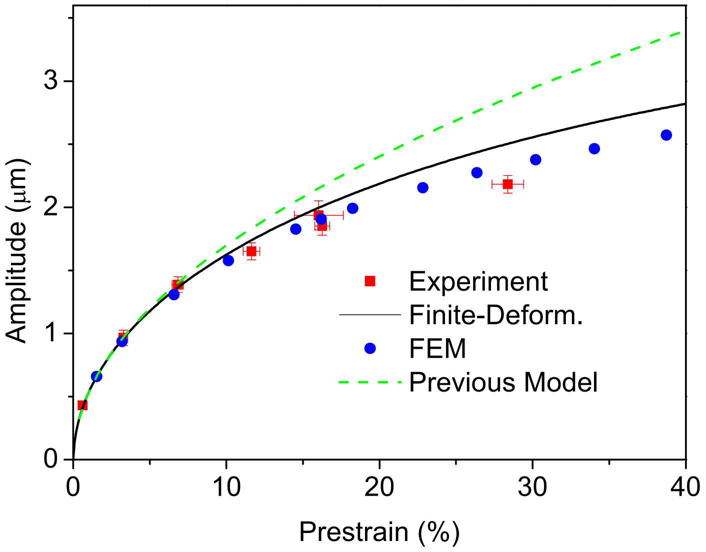

(b) Amplitude

Figure 5-5 Comparison of wavelength and amplitude as function of prestrain

5.4.2 Membrane and Peak Strains in Thin Film due to Prestrain

For $\varepsilon_{pre} < \varepsilon_{cr}$ (the typical critical strain is 0.034% for the Si/PDMS system), relaxing the prestrain does not lead to buckling. Instead, the film supports a small compressive strain $-\varepsilon_{pre}$, which is referred to as the membrane strain. When $\varepsilon_{pre} > \varepsilon_{cr}$, the film buckles to relieve some of the strain. The membrane strain, ε_{mem}, as evaluated in the plane that passes through the midpoint of the thickness of the film, is obtained from Equation (5-13) to be $\varepsilon_{men} = -\frac{1+\xi/3}{(1+\xi)^{1/3}}\varepsilon_{cr}$. For prestrain up to 100%, this membrane strain remains essentially constant, i.e. $\varepsilon_{men} = -\varepsilon_{cr}$. The maximum strain in the film, also called the peak strain ε_{peak}, is the sum of membrane strain, ε_{mem}, and the bending strain, $\varepsilon_{bending}$, induced by the buckled geometry. In most cases of practical interest, the strain associated with the buckled geometry is much larger than ε_{mem}.

Thus this peak strain can be written as

$$\varepsilon_{peak} = 2(\varepsilon_{pre}\varepsilon)^{1/2} \frac{(1+\xi)^{1/3}}{(1+\varepsilon_{pre})^{1/2}}. \tag{5-36}$$

The magnitude of ε_{peak} is typically much smaller than the overall strain, $\varepsilon_{pre} - \varepsilon_{mem}$, which the film accommodates by buckling. For example, in the case of ε_{pre}= 29.2%, ε_{peak} is only 1.8% for the system of Figure 5-1. This mechanical advantage provides an effective level of stretchability/compressibility in materials that are intrinsically brittle. Figure 5-6 shows ε_{peak} and ε_{mem} as a function of ε_{pre}. Both the membrane and peak strains agree well with finite element analysis. The membrane strain is negligible compared to the peak strain and constant throughout this range. Likewise, the peak strain is much smaller than the prestrain, such that the system can accommodate large strains. As a result, ε_{peak} determines the point at which fracture occurs in the film. For Si, the fracture strain is around $\varepsilon_{fracture} = 1.8\%$ (Saif and MacDonald, 1996; Sato, et al., 1997). The maximum allowable prestrain is, therefore, approximately $\frac{\varepsilon_{fracture}^2}{4\varepsilon_{cr}}\left(1+\frac{43}{48}\frac{\varepsilon_{fracture}^2}{4\varepsilon_{cr}}\right)$, which, for the system examined here, is ~29% or almost twenty times larger than $\varepsilon_{fracture}$.

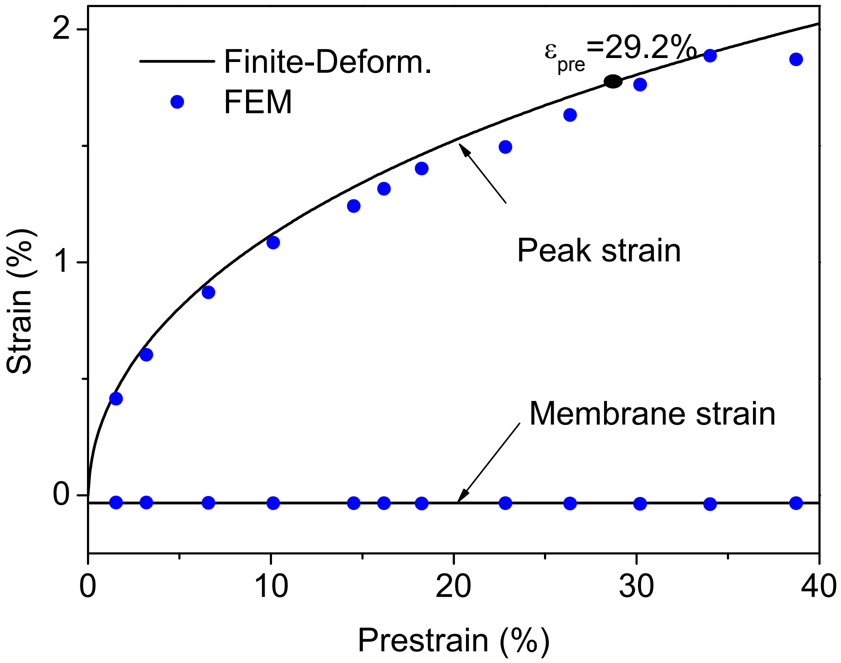

Figure 5-6 Comparison of membrane and peak strains as function of prestrain

5.4.3 Stretchability and Compressibility due to Applied Strain

The minimization of total energy, which is the sum of thin film (membrane and bending) energy and substrate energy according to Equations (5-29), (5-31) and (5-33), gives the amplitude

$$A'' = t\frac{\left(\dfrac{\varepsilon_{pre}-\varepsilon_{applied}}{\varepsilon_{cr}} - \dfrac{1+\varepsilon_{applied}+\dfrac{\zeta}{3}}{(1+\varepsilon_{applied}+\zeta)^{1/3}}(1+\varepsilon_{pre})\right)^{1/2}}{(1+\varepsilon_{pre})^{1/2}(1+\varepsilon_{applied}+\zeta)^{1/3}} \qquad (5\text{-}37)$$

for $\varepsilon_{pre}-\varepsilon_{applied} >> \varepsilon_{cr}$, where the numerator is approximately $\left(\dfrac{\varepsilon_{pre}-\varepsilon_{applied}}{\varepsilon_{cr}}-1\right)^{1/2}$, which gives the amplitude and the wavelength in Equations (5-38) and (5-39)

$$A'' \approx t\frac{\left(\frac{\varepsilon_{pre}-\varepsilon_{applied}}{\varepsilon_{cr}}-1\right)^{1/2}}{(1+\varepsilon_{pre})^{1/2}(1+\varepsilon_{applied}+\zeta)^{1/3}} \tag{5-38}$$

$$\lambda'' = \frac{\lambda_0(1+\varepsilon_{applied})}{(1+\varepsilon_{pre})(1+\varepsilon_{applied}+\zeta)^{1/3}} \tag{5-39}$$

where $\zeta = 5(\varepsilon_{pre}-\varepsilon_{applied})(1+\varepsilon_{pre})/32$. Figure 5-7 shows the experimentally measured and theoretically predicted wavelength λ'' and amplitude A'' versus the applied strain $\varepsilon_{applied}$ for a buckled Si thin film/PDMS substrate system formed at a prestrain of 16.2%. The constant wavelength and amplitude predicted by the previous mechanics models, with ε_{pre} replaced by $\varepsilon_{pre}-\varepsilon_{applied}$, are also shown in comparison with the FEM results. The measured wavelength increases for tension and the measured amplitude decreases, reaching zero once the tensile strain reaches the prestrain. The finite-deformation buckling theory agrees well with experiments and finite element analysis for both amplitude and wavelength. The previous mechanics models also capture the amplitude trend but deviate from the experimental results for large tensile strain (>10%). The amplitude A vanishes when the applied strain reaches the prestrain + the critical strain ε_{cr}. Therefore, the stretchability (maximum applied tensile strain) $=\varepsilon_{pre}+\varepsilon_{fracture}+\varepsilon_{cr}$, which varies linearly with the prestrain. The peak strain in the film is

$$\varepsilon_{peak} = 2\left[(\varepsilon_{pre}-\varepsilon_{applied})\varepsilon_{cr}\right]^{1/2}\frac{(1+\varepsilon_{applied}+\zeta)^{1/3}}{(1+\varepsilon_{pre})^{1/2}} \tag{5-40}$$

Figure 5-8 shows ε_{peak} and ε_{mem} as a function of $\varepsilon_{applied}$. The results predicted by finite-deformation buckling theory agree well with the FEM results. The Si film fails once $\varepsilon_{applied}$ reaches 12.5%. The compressibility is the maximum applied compressive strain when the peak Si strain reaches $\varepsilon_{fracture}$. The compressibility, as shown in Figure 5-9, decreases almost linearly with increasing prestrain, and vanishes when the maximum applicable pretrain $= \frac{\varepsilon_{fracture}^2}{4\varepsilon_{cr}}\left(1+\frac{43}{48}\frac{\varepsilon_{fracture}^2}{4\varepsilon_{cr}}\right)$ is reached. Therefore the compressibility is well approximated by $\frac{\varepsilon_{fracture}^2}{4\varepsilon_{cr}}\left(1+\frac{43}{48}\frac{\varepsilon_{fracture}^2}{4\varepsilon_{cr}}\right)-\varepsilon_{pre}$. Figure 5-9 also shows the strechability $\varepsilon_{pre}+\varepsilon_{fracture}+\varepsilon_{cr}$. As the prestrain increases, the stretchability improves but the compressibility worsens. Such a figure is useful for the design of Si thin films in PDMS stretchable electronics. For example, if a Si thin film and PDMS substrate system has equal stretchability/compressibility, then the prestrain is about 13.4%. In other word, the prestrain is an important value to optimize the stiff thin film-compliant substrate system with same stretchability and compressibility for this type stretchable electronics in the application.

In summary, a set of nonlinear partial differential equations are formulated to evolve the wrinkling shape of stiff thin film-compliant substrate system under prestrain and applied strain. Perturbation analysis is performed for this highly nonlinear system to obtain the analytical solution. The results agree well with experiments and finite element analysis in wavelength and amplitude. In particular, it is found that the wavelength depends on the prestrain and applied strain. Based on the accurate wavelength and amplitude, the membrane and peak strains in thin films, as well as the stretchability and compressibility of the system can be obtained by the nonlinear analytical model.

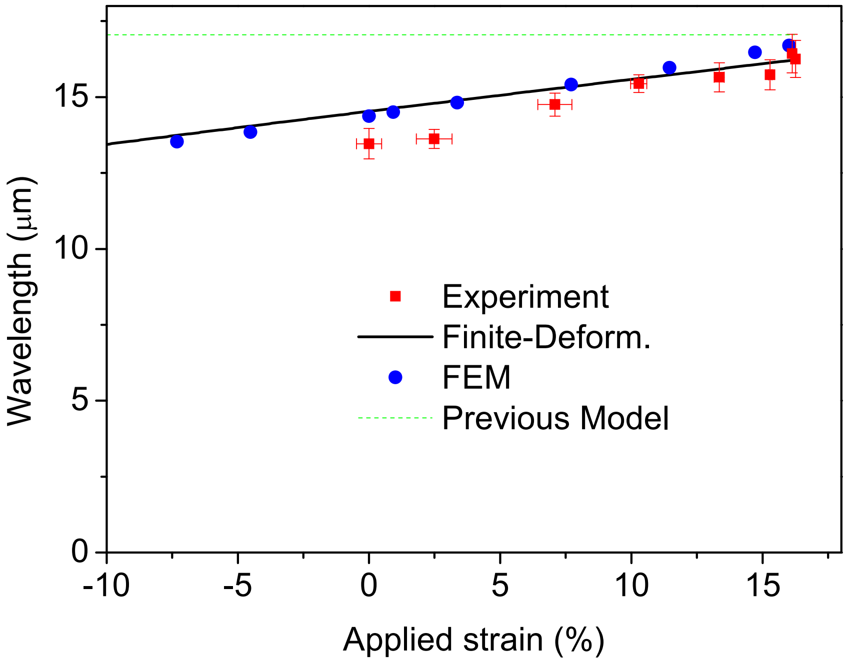

(a) Wavelength

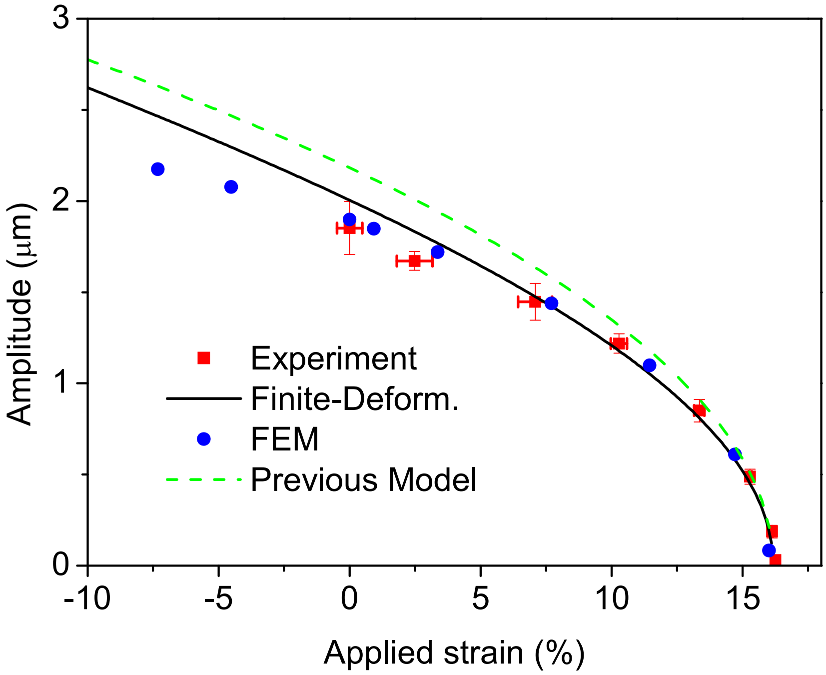

(b) Amplitude

Figure 5-7 Comparison of wavelength and amplitude as functions of $\varepsilon_{applied}$ with

$\varepsilon_{pre} = 16.2\%$

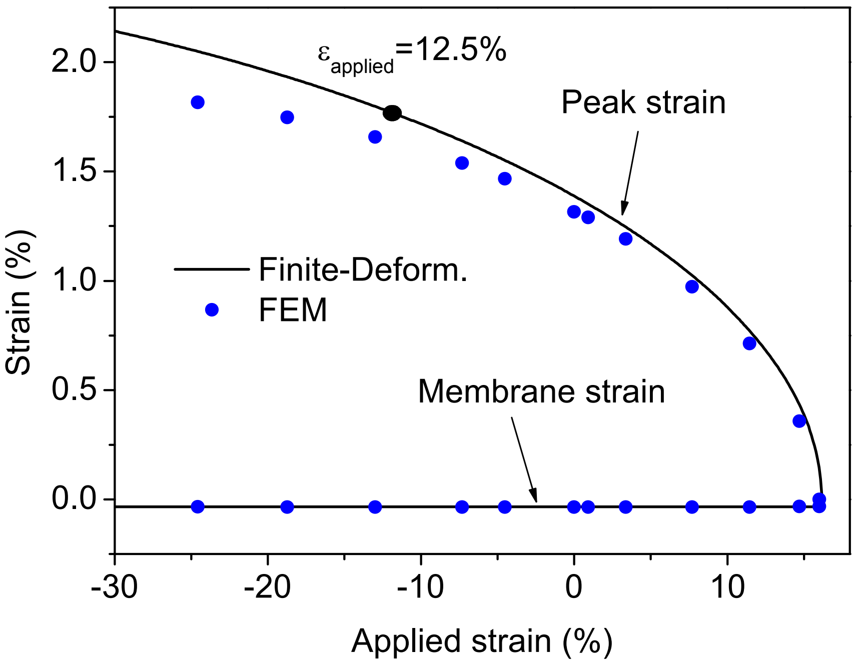

Figure 5-8 Comparison of membrane and peak strains in film as function of $\varepsilon_{applied}$ with ε_{pre} = 16.2%

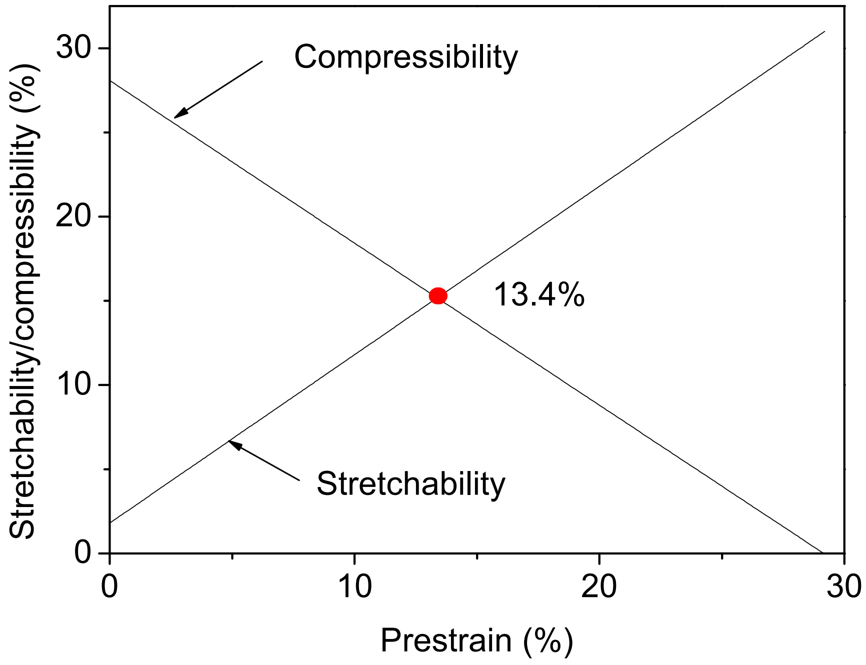

Figure 5-9 Strechability and compressibility of buckled structures of Si on PDMS.

Chapter Six

Two-Dimensional Numerical Simulation for Single Crystal Silicon

Numerical methods are widely used in mechanical analysis since computing power has increased dramatically over the last 30 years. The finite element method (FEM) is one such tool available researchers and engineers. Recently, the FEM has been used to study wrinkling of stiff thin film-compliant substrate system. By using the FEM, Hadi (2001) made comparison between different wrinkling theories and numerical results. Efimenko, et al. (2005) demonstrated the supporting effects of elastometric artificial skins with wrinkles. Jiang, et al. (2008) studied width effect of thin-films analytically, and compared his results with the experimental and numerical results obtained by the FEM.

The FEM is a useful numerical tool when investigating the wrinkling phenomenon of stiff thin film-compliant substrate system. There are two main challenges associated with numerical simulation. (1) Extremely large differences in the geometrical size of the thin films and substrates. The thin film thickness is around 100 nm, that can be 4 orders of magnitude smaller than the substrate thickness which is 1~3 mm. (2) Extremely large differences in the material properties of the thin films and substrates. The thin film modulus is 100 GPa generally that can be 5 orders of magnitude higher than the substrate modulus which is 1~3 MPa.

The following ideas are used to address the challenges in this. When the thin film is much thinner than the substrate, different elements should be used to model the constituents. In a two-dimensional (2D) model, the thin film is modelled with beam elements and the substrate with plain strain elements. In a three-dimensional (3D) model, the thin film is modelled with shell elements and the substrate with solid (brick) elements. If plain strain elements in 2D model and solid elements in 3D model are used for meshing thin film, a fine mesh should be used to avoid shear locking. But a poor mesh may result, since the dimension in the thickness of thin film is much smaller than substrate. Thus, two different element types are used in the FE model. Using mixed element types, the error due to elements with different numbers of nodal degrees of freedom is small compared to error due to poor element mesh in modelling the thin film and relatively thick substrate using only one type of element, where a large number of elements are then required to avoid an excessively high element aspect-ratio and the ensuing non-distortion.

The procedure is presented for performing numerical simulations of buckling effect for stiff thin film-compliant substrate system. It is now possible to compute the actual shape and size of the wrinkles in structures of realistic shape and size. The effectiveness of the proposed procedure is demonstrated by computing the wrinkle details of particular stiff thin film-compliant substrate system, which have been investigated in detail, both experimentally and analytically in Chapters Two and Four. It will be shown that the computational accuracy using the FEM to determine the shape and size of wrinkles is such that the numerical simulation can now be seen as a replacement for physical experimentation, although the computational time is currently still impractically long for the present procedure to be adopted as a routine design tool. A significant and immediate benefit of the present work is that one can probe the simulation results in order to gain additional insight into the characteristics of wrinkles and their evolution under varying initial loading i.e. prestrain.

6.1 Finite Element Method

The FEM is a numerical method used widely by engineers, scientists, and mathematicians to obtain approximate solutions to the differential equations that describe a wide variety of physical (and non-physical) problems. Physical problems range in diversity from solid, fluid and soil mechanics, to electromagnetism or dynamics. The underlying premise of the method states that a complicated domain can be sub-divided into a series of smaller regions in which the differential equations are approximately solved. By assembling the set of equations in each region, the behavior over the entire problem domain is determined. Each region is referred to as an element and the process of subdividing a domain into a finite number of elements is referred to as discretization. Elements are connected at specific points, called nodes, and the assembly process requires that the solution be continuous along common boundaries of adjacent elements

The governing differential equation is now applied to the domain of a single element. At the element level, the solution to the governing equation is replaced by a continuous function approximating the distribution over the element domain. Once the element equations have been determined, the elements are assembled to form the entire domain. In terms of these variables the equilibrium equations obtained by discretizing the virtual work equation can be written symbolically as

$$F^N(u^M) = 0 \tag{6-1}$$

where F^N is the force component conjugate to the N^{th} variable in the problem and u^M is the value of the M^{th} variable. A system of linear algebraic equations results from the assembly procedure. For engineering problems, it is not uncommon for the size of the system of equations to be in the thousands, making the super-computer a desired tool for finding the solution.

The modelling of wrinkling requires elements with quadratic shape (displacement) functions rather than elements with linear shape functions, since quadratic displacement functions model the buckling mode much better with fewer elements. To describe the shape of the wrinkling wave, at least four elements per wave length should be used so that at least 5 nodes are used to approximate the profile of the wave. The substrate should at least be modelled with four elements throughout the material thickness. The sides of the substrate elements should be of equal lengths, forming a square in 2D or cube in 3D.

The model needs to be long enough in the length direction to incorporate more than four wrinkling waves or the length of the model must be equal to the natural wrinkling wavelength. Otherwise an excessively high buckling load will be obtained. The boundary conditions of two ends can be carefully modelled using sliding wall conditions, i.e. all nodes along the boundary are same displacement in direction of perpendicular to the edge (Vonach and Rammerstorfer, 2000), but still the length of the model is important, and must be an even multiple of the natural wavelength or an unacceptably high buckling load is obtained. The model boundaries can also be modelled with simpler non-periodic boundary conditions.

The bending stiffness of a membrane, although small, is a key factor in determining the shape and amplitude of the wrinkles. Therefore, it is essential that this be included in the model that aims to capture the details. Beam element is adapted to study thin film in 2D modeling. Base on FEM, there are several types of beam elements for modeling purposes, and the 2-node linear beam in a plane is chosen for thin films since it is more computationally efficient in the 2D simulation. For the substrate, the plane strain element, a 4-node bilinear plane strain element is used.

Material modeling generally requires a thin film to be modelled as a linear elastic material and the soft substrate to be modelled as a hyperelastic material. This hyperelastic material model uses the Neo-Hookean constitutive law which accounts for the nonlinearity in the stress-strain relation. The Neo-Hookean material law is fully nonlinear in the displacements and the strains. It can therefore be used for large displacement/large strain calculations. The strain energy potential is given as

$$U = C_1(I_1 - 3) + \frac{1}{C_2}(J - 1)^2 \tag{6-2}$$

where I_1 is the first strain invariant,

J is the elastic volume strain,

C_1 and C_2 are materials parameters.

Two materials parameter could be calculated using Young’s modulus and Poisson’s ration (Treloar, 1975) i.e.

$$C_1 = \frac{E}{4(1+\nu)} \text{and } C_2 = \frac{6(1-2\nu)}{E} \tag{6-3}$$

After the finite element model is set up, the wrinkling simulation is performed in three stages: (1) buckling mode analysis, (2) prestrain applied on substrate and (3) shrinking of substrate and buckling of thin film.

6.1.1 Traction Force Analysis.

The interaction between thin film and substrate is the main reason to cause buckling of the thin film. The buckling mode shapes of thin film are determined by the traction force due to the interaction. The initial stage of the analysis involves applying a uniform prestrain to the stiff thin film-compliant substrate system. Then the area bounding the thin film location is constrained. The substrate traction force is then found by releasing the applied displacement (see Figure 6-1). Several strategies can be used to apply this initial prestrain. One technique is to prescribe a set of edge displacements, corresponding to the level of prestrain required, and is particularly useful for setting up the true stress state of a membrane structure, e.g. to reproduce the conditions that may exist at the beginning of fabrication. After applying the initial prestrain, they are constrained such that the nodes are sheared between thin film and substrate elements. The next step is to release the applied strain and allow the substrate to shrink. A static, geometrically nonlinear equilibrium check is then performed, which induces the re-distribution of the state of prestrain, together with small in-plane displacements. Thereafter the reaction force can be found at the constrained nodes.

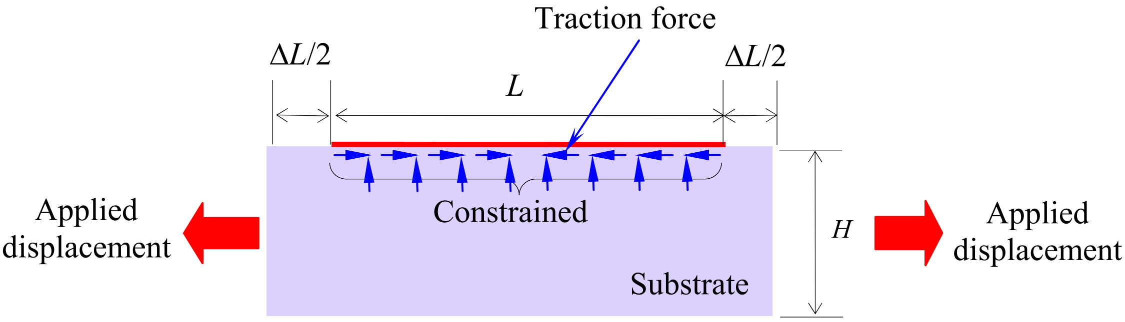

Figure 6-1 Applied load and traction force

6.1.2 Eigenvalue/Eigenvector Extraction.

The next step of the analysis determines the buckling mode-shapes due to prestrain. These modes are then used as small, initial imperfections that trigger the formation of wrinkles in the subsequent, geometrically nonlinear simulation. An eigenvalue buckling analysis is used to obtain the possible wrinkling modes of the membrane subjected to its actual boundary conditions and loading. The loading is typically defined in terms of a set of applied forces which are obtained in the previous stage, and is required to represent the loads due to prestrain. It is important that both the initial strain and displacements from the previous stage of the analysis, as well as those due to the applied displacement, should be included in the calculation of the tangent stiffness matrix. The eigenvalues and eigenvectors of the tangent stiffness matrix correspond to the load magnitudes and shapes of the possible wrinkling modes of the membrane.

In standard buckling analysis of imperfection-sensitive structures, the imperfections that are seeded in the structure are normally obtained as linear combinations of the eigenvectors corresponding to the lowest eigenvalues. The main objective of the buckling analysis is to find the lowest eigenvalue, corresponding to the load which would cause the first wrinkle to form, since the first buckling forms almost as soon as the load is applied. The main interest here is the evolution of the first buckling, leading to the formation of a second one, and so on until buckling takes place at a large number of locations to become the wrinkling pattern. It is desirable to introduce in the membrane a general form of imperfection, e.g. a combination of many eigenvectors. In cases where some features of the final wrinkling pattern are known, introducing eigenmodes that resemble this pattern in the imperfection shape, as well as several other eigenmodes, generally increases the speed of numerical convergence.

After computing the buckling mode-shapes, a linear combination of all, or some selected eigenmodes is introduced into the structure as a geometrical imperfection in the form of out-of-plane deformations of the membrane as follows:

$$\Delta w = \sum_{i} w_i \phi_i \qquad (6\text{-}4)$$

where w_i is the i-th eigenmode and ϕ_i is a scaling factor whose magnitude is chosen as a proportion of the thickness of the membrane. The scaling values are between 1% and 5% of the thickness.

6.1.3 Simulation of Wrinkle Growth.

The simulations of wrinkle growth are performed in the same procedure as the key fabrication steps of the stiff thin film-compliant substrate system introduced in Chapter Two. A geometrically nonlinear incremental analysis is performed under edge displacement incrementation. The equilibrium path of a wrinkled membrane includes many unstable branches, each corresponding to a localized snap-through due to the formation of an additional wrinkle. A popular algorithm to compute the full response of the structure is an arc-length solution. But all attempts to use the arc-length solution method in here were unsuccessful, possibly because wrinkling is a highly localized type of instability. Hence, monotonic displacement incrementation is the only viable option.

In the nonlinear numerical simulation, it is assumed that the problem is stable at the beginning and that instabilities may develop in the course of incremental solution. In order to compute the static equilibrium state, especially, after introducing the imperfections, the pseudo-inertia and pseudo-viscous forces are introduced at all nodes to help numerical convergence. The fictitious viscous forces are calculated on the basis of the model's response in the first iteration of the analysis step, by assuming that the energy dissipated is a prescribed fraction of the strain energy during the first step. This fraction is called the damping intensity or stabilization factor in FEM. While the model is stable, viscous forces and, therefore, the viscous energy dissipated are very small. Thus, the additional artificial damping has no effect. If a local region goes unstable, the local velocities increase and, consequently, part of the strain energy then released is dissipated by the applied damping. In this simulation, the value taken is 2×10^{-4} and the results are found to achieve good accuracy. It is generally desirable to set this parameter to the lowest possible value for which convergence can still be achieved.

6.2 Simulation Results

The experimental study of wrinkle formation in the fabrication process has been reported in Chapter Two. Firstly, the substrate is elastically stretched to a certain prestrain value. Then, it is brought into conformal contact with the silicon ribbon and the whole system is released to reach the equilibrium state. Following the analytical solution (Chapter Three and Five), the fabrication mechanism is simplified as a 2D problem, and correspondingly, the 2-D stiff thin film-substrate FE model is constructed to simulate the single crystal silicon ribbons upon the PDMS substrate. This FE model consists of a thin (0.1 μm) and stiff (Young Modulus, E_f = 130 GPa; Poisson ratio, ν_f = 0.27) silicon ribbon and a thick (3 mm) and soft (Young Modulus, E_s = 1.8 MPa; Poisson ratio, ν_s = 0.48) substrate. For all simulations, the horizontal displacement is set to be zero along the PDMS substrate bottom in the model, and periodicity conditions are prescribed along both edges of the substrate. The numerical simulations are carried out using commercial software ABAQUS (2007).

The simulation analysis is divided into three stages as discussed in Section 6.1. First, prestrain is applied to the substrate by prescribing a set of edge displacements, corresponding to the level of prestress required. The nodes are fixed on the thin film upper surface to obtain the reaction force from the release of the prestrained substrate. The traction force is obtained from this stage. Then the buckling analysis is performed by applying the reaction force obtained from the first step to the whole system so as to determine the buckling mode-shapes. The first mode is then imposed as small, initial imperfections that trigger the formation of wrinkles in the subsequent, geometrically nonlinear simulation. Finally, with the imperfection of the first mode shape, the substrate in the absence of silicon is stretched according to the prestress required. In the stressed condition, the silicon thin film is fully bonded to the substrate and the whole system is released to the equilibrium state by a geometrically nonlinear incremental analysis.

6.2.1 Amplitude and Wavelength

The amplitude and wavelength of wavy silicon thin film are simulated using FEM in this section. Figure 6-2 shows the sketch of the FE model. It shows that the prestrain energy from substrate is transferred to the silicon ribbon and causes the silicon ribbon to wrinkle. Since the amplitude and wavelength of wavy silicon ribbon should be changed with the prestrain, the wrinkle formation and propagation within a finite length of silicon ribbon is simulated at the different prestrain values. As mentioned provious, there are two challenges associated with this type of numerical analysis. (1) Extremely large differences in the elastic properties of the films and substrates e.g. the film modulus is approximately 130 GPa and is five orders of magnitude higher than the substrate modulus which is approximately 1.8 MPa. (2) Extremely large differences exist in the thickness of the films and substrates e.g. the film thickness is approximately 100 nm, and is four orders of magnitude smaller than the substrate thickness, approximately 3 mm. In order to overcome these two challenges, a fine mesh is used near the thin film/substrate interface and a coarse mesh is used far away from the interface in the FE model. The smallest element size is 0.4 μm × 0.4 μm, and hence more than 160 thousands elements in total are required for the mesh. The finite element mesh sensitivity has been carefully checked using a refined mesh i.e. convergence study. To avoid element distortion in the event of large deformation, the mesh is designed to incline to the prestrain direction (illustrated in Figure 6-2). To do so, the elements become nearly rectangle during shrinking and numerical convergence is found to be easier. In addition, very small computational increments of less than 10^{-2} are used to ensure that the results are convergent for systems involving vastly different elastic moduli.

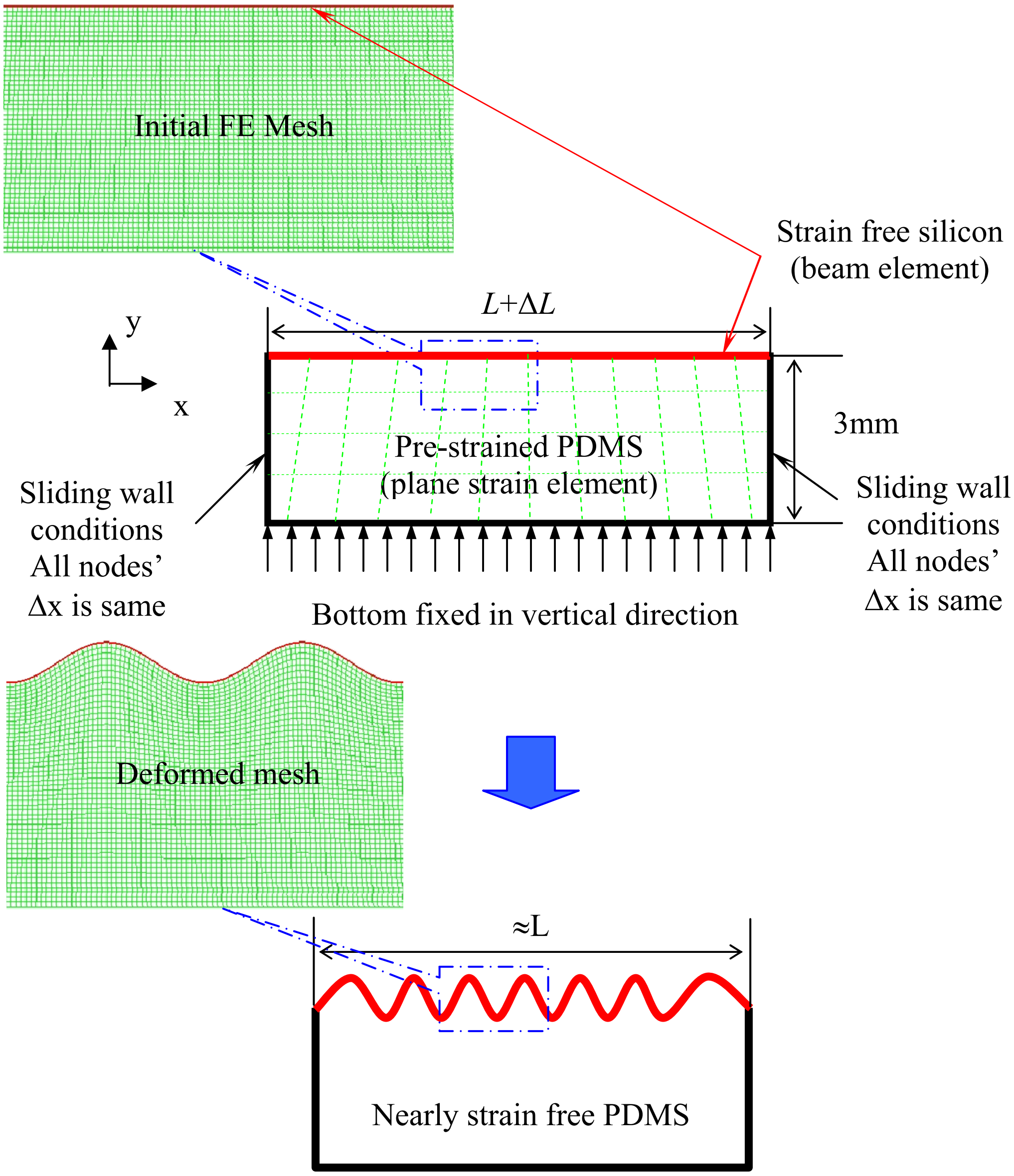

Figure 6-2 Illustration of FE model configuration

The wrinkling of the thin film (silicon ribbon) is computed at different prestrain values. Figure 6-3 shows the numerically simulated wrinkling patterns at

4%, 10% and 20% prestrain which resemble typical experimental observation in Figures 2-6 and 2-7. From these simulation results, it is found that the wrinkle is formed at the middle of the silicon ribbon, where there are flat regions at the two ends of the silicon ribbon. In the wrinkling region, the wave amplitude increases with prestrain and the wavelength decreases slightly. The comparison between the FE simulation results and experimental data is shown in Figure 6-4. Good agreement is observed between the numerical and experimental results. For the wavelength and amplitude, the numerical error is less 3%. The FEM can capture well the wrinkling of stiff thin film-compliant substrate system. Thus, the validated FE model and procedure can be used in the next step to study post-buckling and edge effect.

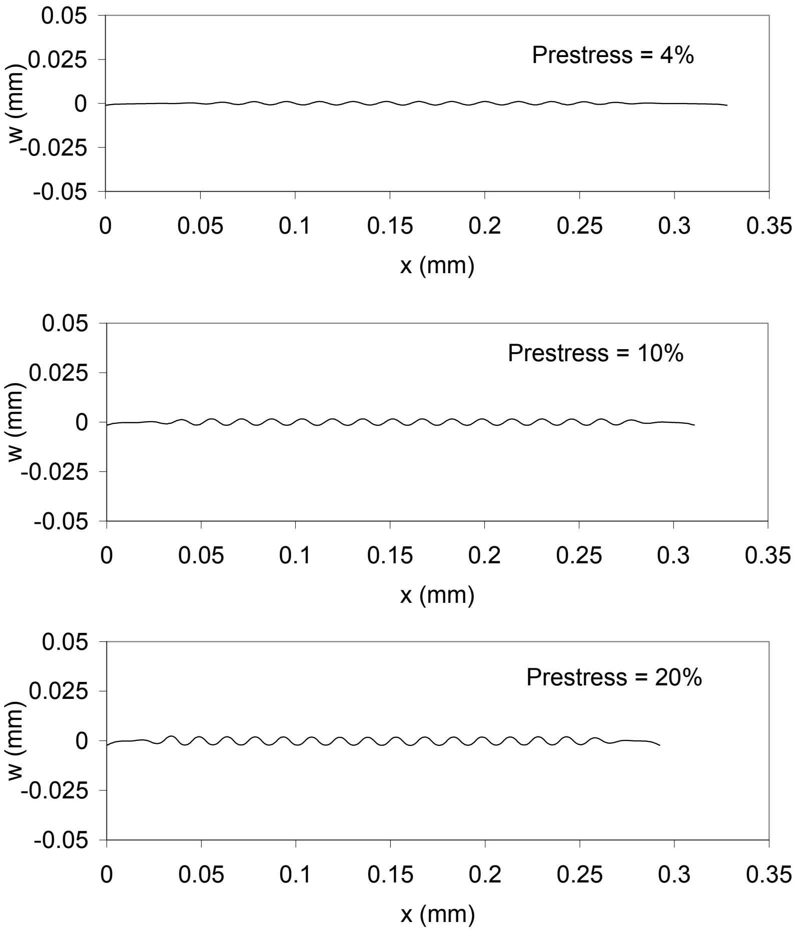

Figure 6-3 Numerical simulation results for wrinkle patterns of silicon ribbon at different substrate prestrain values.

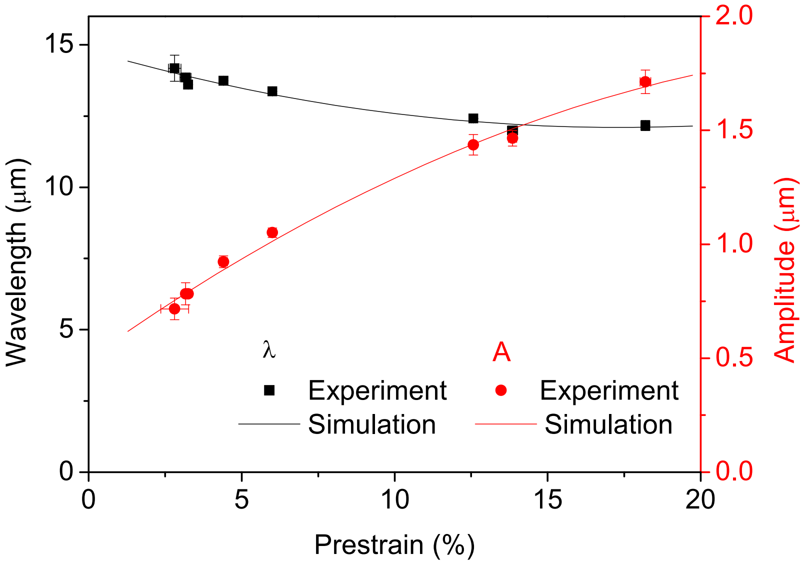

Figure 6-4 Comparison between numerical and experimental results for wavelength and amplitude at different prestrain

6.2.2 Post-buckling simulation

The numerical simulation of buckling presented in Section 6.1 is for stiff thin film-compliant substrate system subjected to prestrain. The post-buckling behavior, i.e. the system subjected to the applied strain after buckling, is studied in this section.

The numerical result can be used to determine the system stretchability/compressibility. Figure 6-5 illustrates the buckled Si thin film and relaxed PDMS substrate of length L (Figure 6-5a) and the system that is subjected to the applied strain $\varepsilon_{applied}$ and has the length $(1 \pm \varepsilon_{applied})L$ (Figure 6-5b and c). The numerical results are good agreement with the experimental and nonlinear analytical results. The comparison has been presented in Figures 5-5 and Figure 5-6 in Chapter Five.

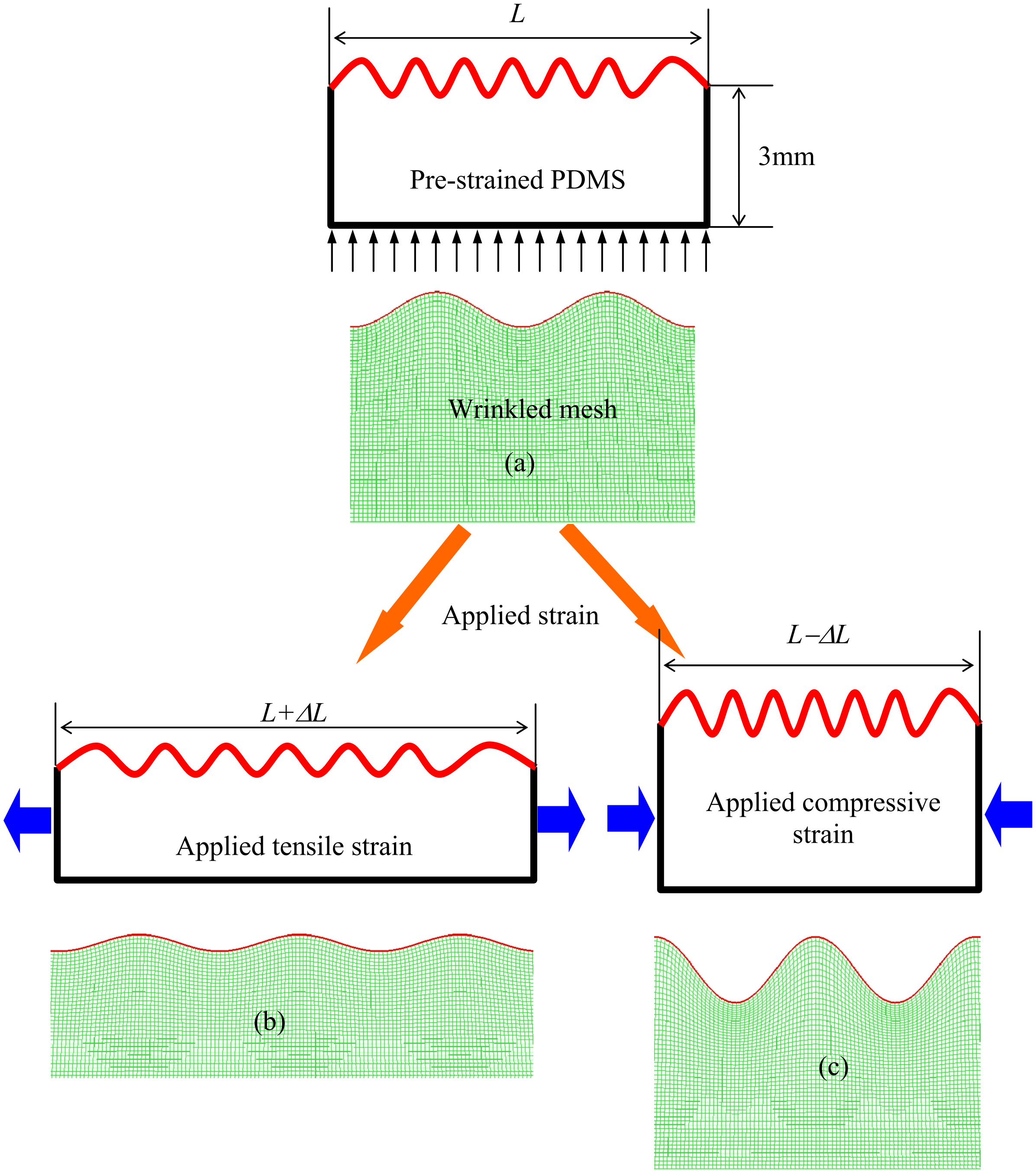

Figure 6-5 Illustration of FE model under applied strain

6.2.3 Edge Effect

Section 6.2.1 demonstrates that the numerical model could accurately capture the effects of systems that are located far from the boundaries. The results, however, do not apply to regions of the films that lie near the edges. In these regions, the amplitudes of the waves decrease gradually to zero, as illustrated schematically in Figure 6-6 and by the optical images in Figures 6-7 and 6-8.

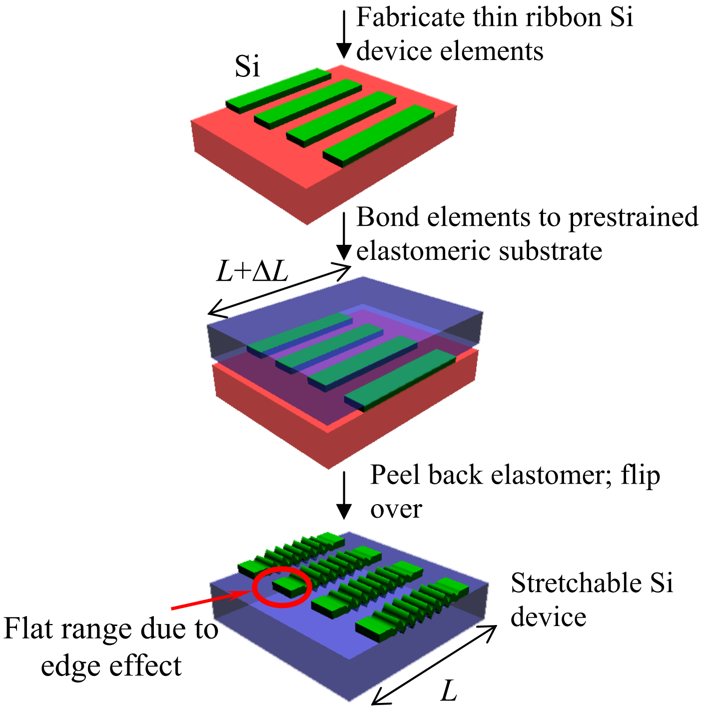

Figure 6-6 Schematic illustration of process for fabricating buckled single crystal silicon ribbons (green) on PDMS (blue) substrate with edge effect.

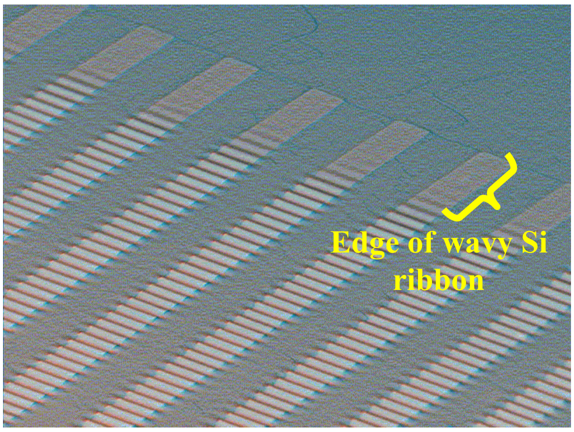

Figure 6-7 Wavy single crystal silicon ribbons on PDMS substrate.

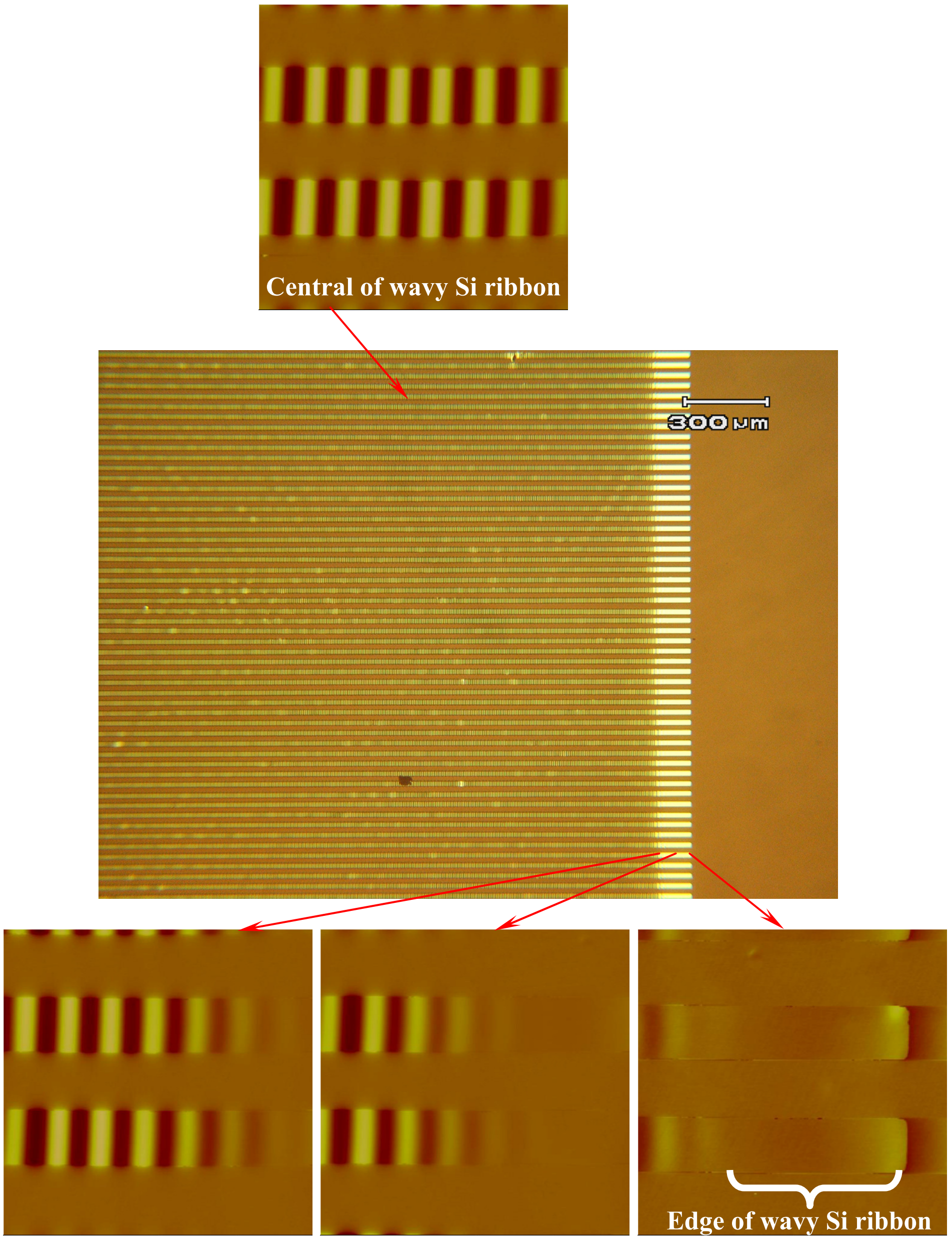

Figure 6-8 Optical image of edge effect

Analytical solutions are not possible in the region near the edge, therefore necessitating the use of the numerical method to reveal the physics and the effect of film thickness, prestrain, and thin film and substrate materials properties. The simulation study presented here aims to explain quantitatively the mechanical behavior of the system at and near the edge (i.e. the flat area). This effect is not only observed for the particular system shown in Figures 6-6 and 6-7, but also for the more general case of thin films on compliant supports. The FE model is schematically explained Figure 6-9.

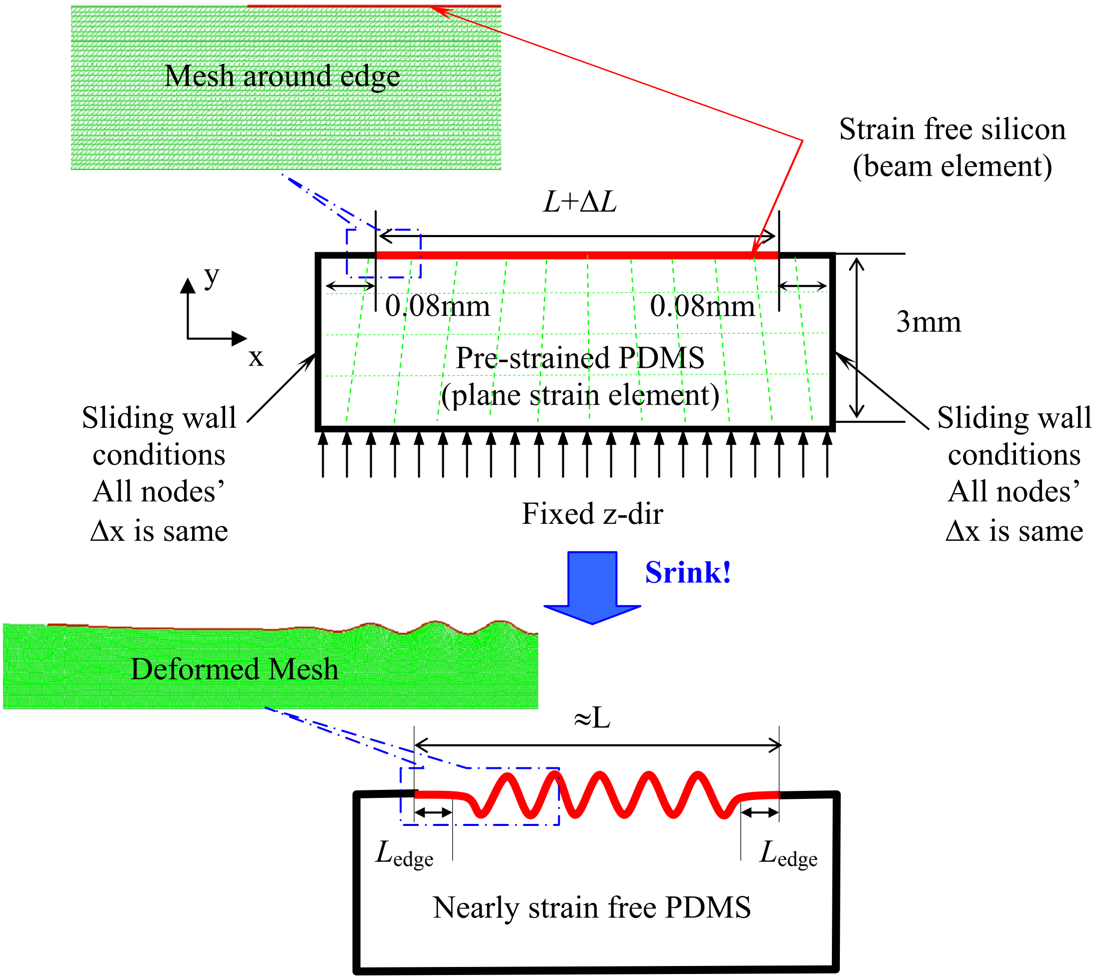

Figure 6-9 Illustration of finite element model for edge effect

This edge effect can be seen clearly in atomic force microscope (AFM) images of Figure 6-10a for 100nm-thick ribbons of silicon with widths of 20 μm and separations of 20 μm, bonded to a 3.5 mm-thick PDMS substrate. The frames on the left (images and line cuts) correspond to periodic structures that exist at regions far from the free edge: those on the right show regions near the free edge. The buckled shape shown in Figure 6-10c is obtained from FE analyses that is described in the following paragraph. In figure 6-10, the images in the left and right columns are correspond to the center part and edge of the silicon thin film, respectively.

The modeled two-dimensional system consists of a 1.3 mm-long and 3 mm-thick PDMS substrate subjected to a prestrain ε_{pre} imposed at its two edges. A shorter (L=1 mm-long) and much thinner (100 nm-thick) silicon thin film resides on and is coupled to the top surface of the stretched PDMS substrate. The thin film covers the center part of the substrate surface, leaving bare regions of the substrate (uncovered by the film) near the two edges, as schematically shown in Figure 6-9. The thin film and substrate are modeled by beam and plane-strain elements, respectively.

Young's moduli and Poisson's ratios of the silicon film and PDMS substrate are E_f = 130 MPa, ν_f = 0.27, E_s = 1.8 MPa and ν_s = 0.48, respectively. The wavelength λ and amplitude A near the center of film (i.e. away from the edges) obtained from the FE analysis are shown as a functions of ε_{pre} in Figure 6-10 for the silicon thin film and PDMS substrate. For comparison, λ and A determined by

AFM are also shown in Figure 6-10(a), where the prestrain, ε_{pre}, has been obtained from experimental measurements, i.e.

$$\varepsilon_{pre} = (\lambda_{contour} - \lambda)/\lambda \tag{6-5}$$

where $\lambda_{contour}$ is the contour length and λ is the wavelength of the buckled film.

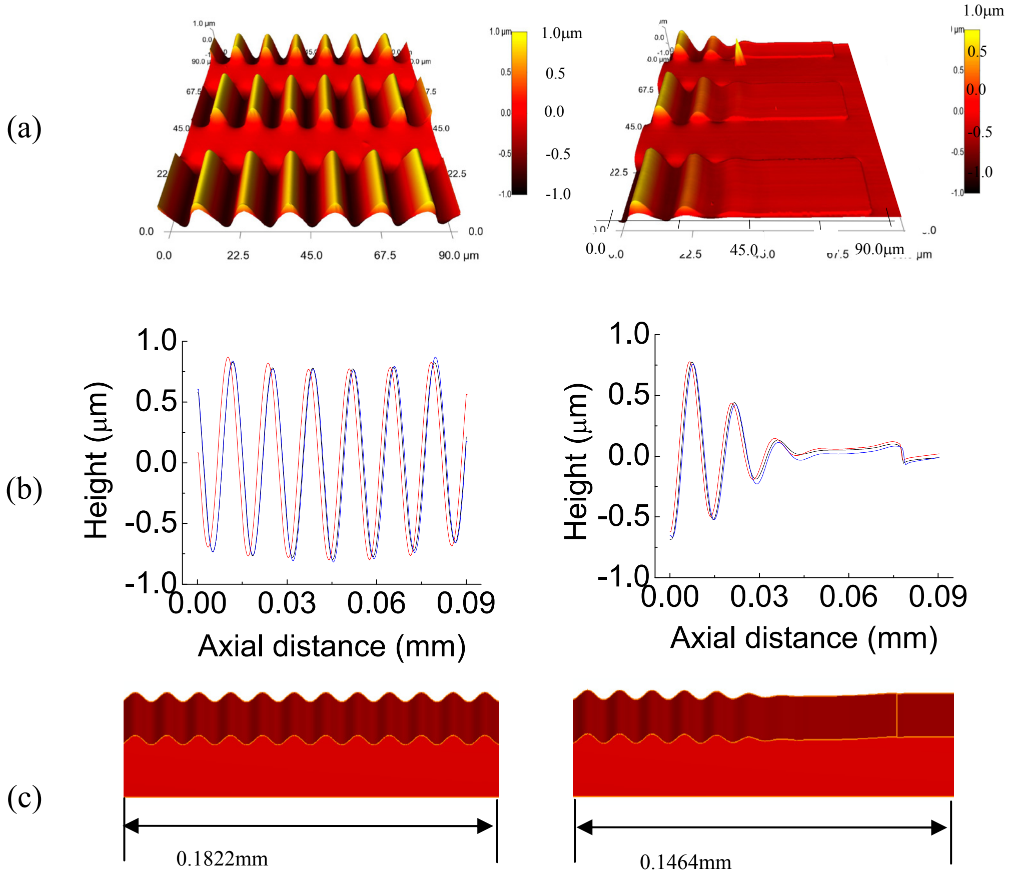

Figure 6-10 (a) Images and (b) linecuts of atomic force micrographs, and (c) finite element results of buckled single crystal silicon ribbons on PDMS substrate.

Figure 6-11 also shows the analytical solution of λ and A according to Equation (3-47). The experimental and analytical solutions all agree well with the numerical results without any parameter fitting, therefore providing a validation of the

FE analysis again. The wavelength λ near the center of the film, as shown in Figure 6-11, is approximately 14 μm.

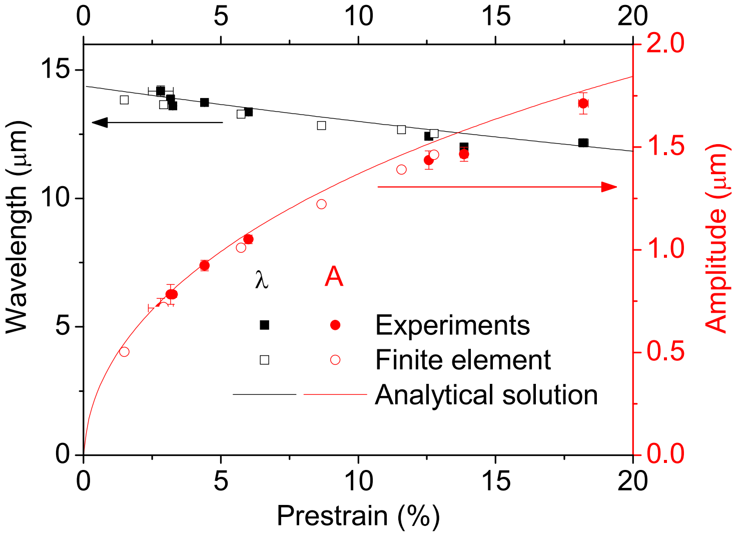

Figure 6-11 Wavelength and amplitude around center part of buckled silicon thin film versus prestrain.

The edge-effect length L_{edge} is defined as the distance from the edge to the midpoint between the first peak and valley nearest to the free edge as shown in the inset of Figure 6-12. L_{edge} versus ε_{pre}, for Young's modulus E_s=3Mpa of the PDMS substrate is shown in Figure 6-12. The experimentally measured L_{edge} from Figure 6-10 agrees well with the numerical results as shown in Figure 6-12, again without any parameter fitting.

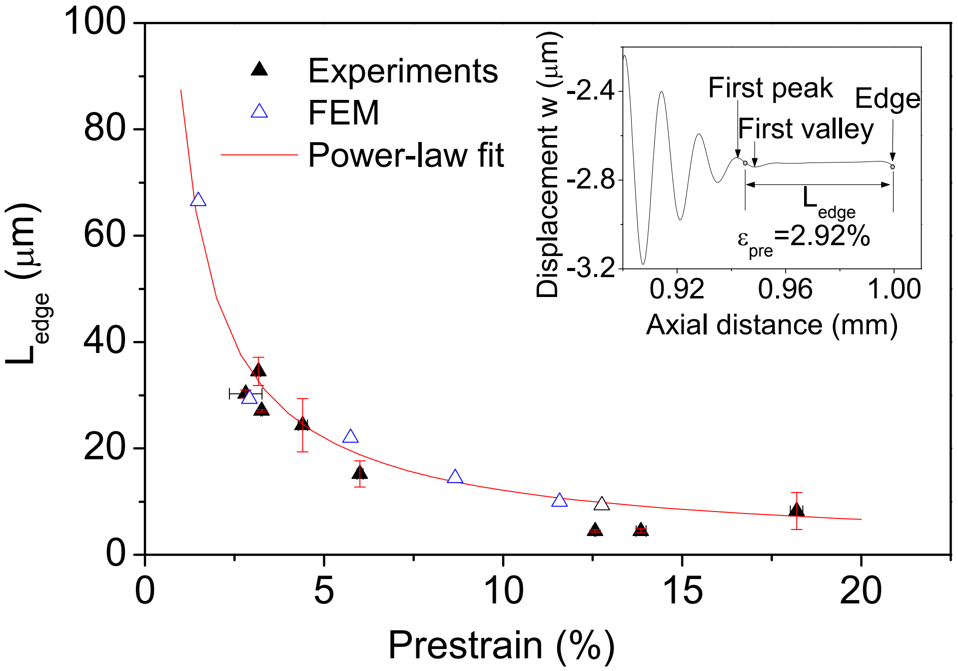

Figure 6-12 Edge-effect length L_{edge} versus prestrain

Figure 6-13 shows the edge-effect length L_{edge} versus the prestrain ε_{pre} for two different values of the PDMS modulus E_s =1.8 MPa and 3MPa with same geometrical size. The value of L_{edge} for E_s =1.8 MPa is higher than that for E_s =3MPa, which suggests that the edge effect increases as the substrate modulus decreases. In fact, by dimensional analysis the edge-effect length can be shown to be proportional to the film thickness t,

$$L_{edge} = tf(\varepsilon_{pre}, \varepsilon_{cr}) \tag{6-6}$$

where f is a non-dimensional function of the prestrain ε_{pre} and buckling critical strain ε_{cr}, and it decreases as ε_{pre} or ε_{cr} increases.

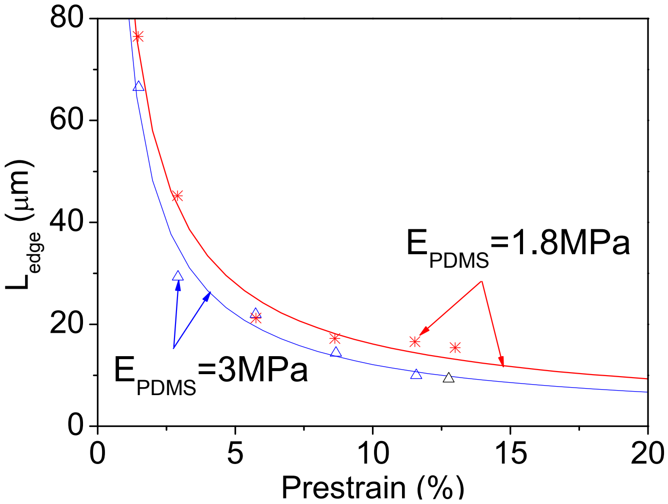

Figure 6-13 Edge-effect length L_{edge} versus modulus of substrate

The distribution of axial force in the buckled thin film, as shown in Figure 6-14, explains the edge effect. Except near the edges, the axial force is constant in the thin film, and it is this compressive force that causes the thin film to buckle. Nevertheless, this compressive force decreases to zero at the free edges and hence the film in these regions does not buckle. Therefore, the flat region of the thin film results from the traction-free boundary condition at the edges.

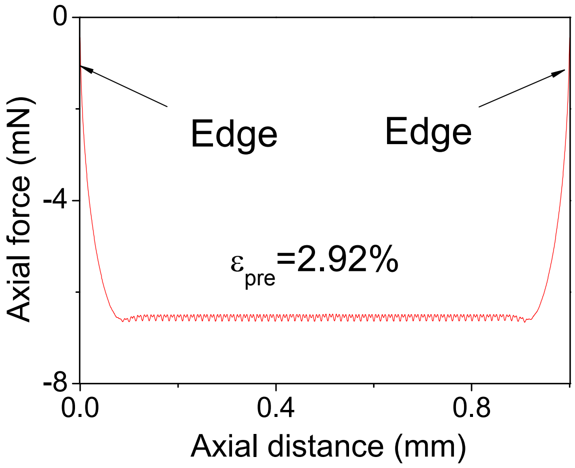

Figure 6-14 Axial force in thin film

In summary, the FEM can capture well the wrinkling effect of the stiff thin film-compliant substrate system. The results of 2D FE model are in good agreement with the experimental and analytical results in term of amplitude and wavelength of wrinkling wave vary associates with prestrain. Therefore the FE model can be used for more complex scenario which the analytical method is difficult to solve e.g. near the edge. The flat region around the edges of buckled thin films of compliant substrates is due to the traction-free edges. The edge-effect length L_{edge} is proportional to the thin-film thickness, and decreases with the increasing prestrain and substrate modulus. These findings would provide useful design guidelines for implementation of the near edge regions in certain classes of applications in stretchable electronics and other areas, e.g. well-placed edges can lead to flat regions in a larger scaled buckled system where planarity is required for efficient photo detection.

Chapter Seven

Three-Dimensional Numerical Simulation for Integrated Circuits

Three-dimensional numerical simulation by means of the FEM is needed to solve the problem of stretchable and foldable integrated circuits, which cannot be simplified to 2D analysis. The numerical simulation will be carried out in the context of nonlinear mechanics. The FEM can help to reveal key features of mechanics in buckling, such as the stress and strain distributions in different layers. The results can be used to understand the formation of wave structures with non-linear buckling. A challenge in 3D numerical analysis that is not present in 2-D analysis is that the thin film becomes a multilayer structure when modeling 3-D integrated circuits, in addition to the previous challenges mentioned in Chapter Six, i.e. large differences in material properties and geometrical size between the stiff thin film and compliant substrate.

7.1 Three-Dimensional Finite Element Models

A typical stretchable and foldable thin film with silicon integrated circuits has been shown in Chapter Three (Figure 3-2). There are three main parts: $p-$MOSFET, $n-$MOSFET and interconnect lines in the single integrated circuits. Each part is combined by different materials layer on different area of thin film and including combination of PI (Polyimide), SiO_2, Si and Metal layer (chromium–gold–chromium). To model this type of thin film, a multilayer shell element should be used. That is, the

$p-$ MOSFET and $n-$ MOSFET regions consist of five material layers (SiO_2/metal/SiO_2/Si/PI) with thicknesses of approximately 0.05 μm / 0.15 μm / 0.05 μm/0.25 μm / 1.2μm respectively, and the metal interconnects consists of four materials layers (SiO_2/metal/SiO_2/PI) with the thickness of approximately 0.05 μm / 0.15 μm / 0.05 μm / 1.2μm, respectively. The bending and membrane stiffness are important in determining the shape of the wrinkles. Therefore, it is essential that the FE model should capture these wrinkling pattern details.

In the FEM, shell elements are used to model structures in which one dimension, the thickness, is significantly smaller than the other two dimensions. The action of shell depends on the ratio of the thickness to a characteristic dimension:

- Very thick shell: 3D effects are significant.
- Thick shell: membrane, bending and higher order transverse shear should be considered.
- Moderately thick shell: membrane, bending and first order transverse shear are counted.
- Thin shells: membrane and bending energy should be considered but transverse shear can be neglected
- Very thin shells (also call membranes): dominated primarily by membrane effects.

A typical thin film integrated circuit thickness is from 1.45 μm to 1.7 μm, and is much smaller than the width (300 μm) and length (600 μm) dimensions of the circuit. Transverse shear deformation can be neglected. Hence it is appropriate to consider thin shell for the numerical simulations as it accounts for the membrane and bending energy, and this is consistent same the analytical model in Chapter Four and Chapter Five.

Shell elements developed for the FEM can be classified into three main types: (1) constructing flat shell elements by combining plane stress and plate bending elements; (2) establishing shell elements degenerated from 3-D elements and considering transverse shear; (3) formulating curved shell elements based upon classical shell theory.

Each of the above three shell element types has its pros and cons. The first type is the simplest but the least accurate. Thus for good accuracy, the shell structure has to be modelled using a relatively large number of flat elements. The second type of shell element (first proposed by Ahmad et. al. 1970) is formulated from 3D continuum Mindlin-Reissner theory. Reduced integration is employed to mitigate the shear locking problem. It is relatively complex and higher order elements (9-nodes or 12-nodes) are usually needed to provide accurate solutions with fewer numbers of elements. But the overstiff solution may still occur in problems with highly constrained boundaries, and the stiffness formulation and solution equations for this element type can be very time consuming and may affect the overall efficiency. Special attention is required to treat the interface between thin film and substrate where elements meeting are coplanar. The numerical accuracy could be affected due to interaction between thin film (shell element) and substrate (solid element). Thus, the second type of shell element is not used in this simulation. As for the third type of shell element, the geometrical description of the curved element is accurate, but it is difficult to construct displacement function of C^1 continuity and C^0 continuity is implemented instead. When the FE mesh is designed well, for example the element size is small enough, the good accuracy will be obtained. The quadrilateral finite-membrane-strain thin-shell element with multilayer section is chosen in this numerical simulation. This is more computational efficient than using high-order elements. In view of the fact that the film is very thin and transverse shear deformation can be neglected. The formulating curved shell element with C^0 continuity is able to capture well the thin shell behaviour in accordance with the Kirchhoff shell theory. In this element (Figure 7-1), the normal rotations θ_x and θ_y are represented by using $\partial w / \partial x$ and $\partial w / \partial y$ as shear deformation is neglected. Thus the shears $\theta_x + \partial w / \partial x$ and $\theta_y + \partial w / \partial x$ may reduce to zero for thin shells. When the FE mesh is carefully designed, the good accuracy can be obtained. If high-order shell elements (for example 9-nodes) are used for thin film, then the same high-order solid elements (with 27-nodes) have to be used for substrate to connect thin film mesh. To do so the computational time will increase rapidly.

Shell elements may be either of single variable (commonly displacement) or of multi-variables (hybrid element, mixed element and hybrid/mixed element). The formulation of displacement based single-variable shell element is mainly based upon the Hellinger-Reissner variational principle while the hybrid /mixed methods are based upon Hu-Washizu variational principle (Belytschko et al. 2000).

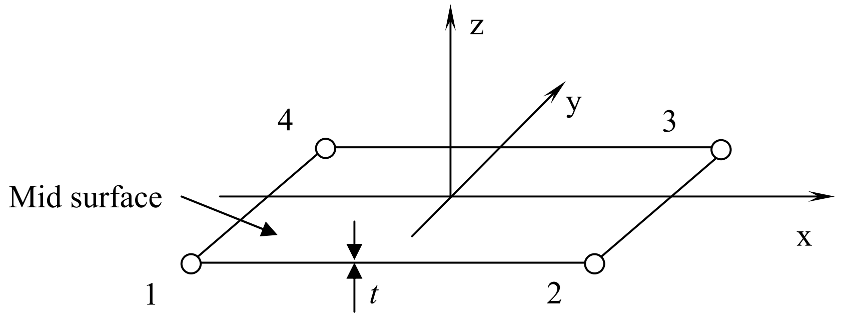

Figure 7-1 4-node quadrilateral element

There are 5 degree of freedom at each node: $u_i, v_i, w_i, \left(\frac{\partial w}{\partial x}\right)_i, \left(\frac{\partial w}{\partial y}\right)_i$ (i=1,2,3,4). For each element, the deflection $w(x, y)$ is represented by

$$w(x,y) = \sum_1^4 \left[N_{ui}u_i + N_{vi}vi + N_{wi}w_i + N_{xi}\left(\frac{\partial w}{\partial x}\right)_i + N_{yi}\left(\frac{\partial w}{\partial x}\right)_i \right] \tag{7-1}$$

where $N_{ui}, N_{vi}, N_{wi}, N_{xi}, N_{yi}$ are shape functions. The stiffness matrix is

$$\mathbf{k} = \int_v \mathbf{B}^T \mathbf{E} \mathbf{B} dV \tag{7-2}$$

where $\mathbf{B}$ is the strain-displacement matrix and $\mathbf{E}$ the stress-strain matrix.

Typically, 4-node quadrilateral general purpose shell element is usually used with full integration. But the 4-node reduced integration, thin-shell elements with five degrees of freedom per node is more computationally efficient. Hourglass control is used to suppress mesh instability associated with spurious zero energy mode (Flanagan and Belytschko, 1981).

Experimental observations (Kim, 2008) show that the buckling patterns are almost the same for each circuit (Figure 7-2). Thus the FE model dimensions are chosen in such a way as to cover the substrate around only one typical circuit (Figure 7-3 top). Multi-layer shell elements depicted in Figure 7-4 are used to model the thin film which is bonded to the substrate surface. The thickness is defined through the section property definition. In the $p-$MOSFET and $n-$MOSFET regions, there are five material layers (SiO_2/metal/SiO_2/Si/PI) with thicknesses of 0.05 μm / 0.15 μm / 0.05 μm /0.25 μm / 1.2 μm. The metal interconnects consists of four materials layers (SiO_2/metal/SiO_2/PI) with the thickness of 0.05 μm / 0.15 μm / 0.05 μm / 1.2 μm.

The manufacturing process results the presence holes in the thin film located between each integrated circuit (Figure 7-3), and no FE meshes are used in these locations as shown on the edge of thin film mesh in Figure 7-4. The eight-node, hexahedral brick elements are used for the PDMS substrate (Figure 7-3 bottom).

The deformation patterns show periodicity between each circuit. Thus, sliding wall conditions are applied to the external surface of the substrate as same as the boundary conditions in 2D FE model. This condition allows all surface nodes to have the same displacement in the direction of surface normal whereas the other two directions are unconstrained (Vonach and Rammerstorfer, 2000). In addition, the nodes of the bottom substrate are constrained in the vertical direction.

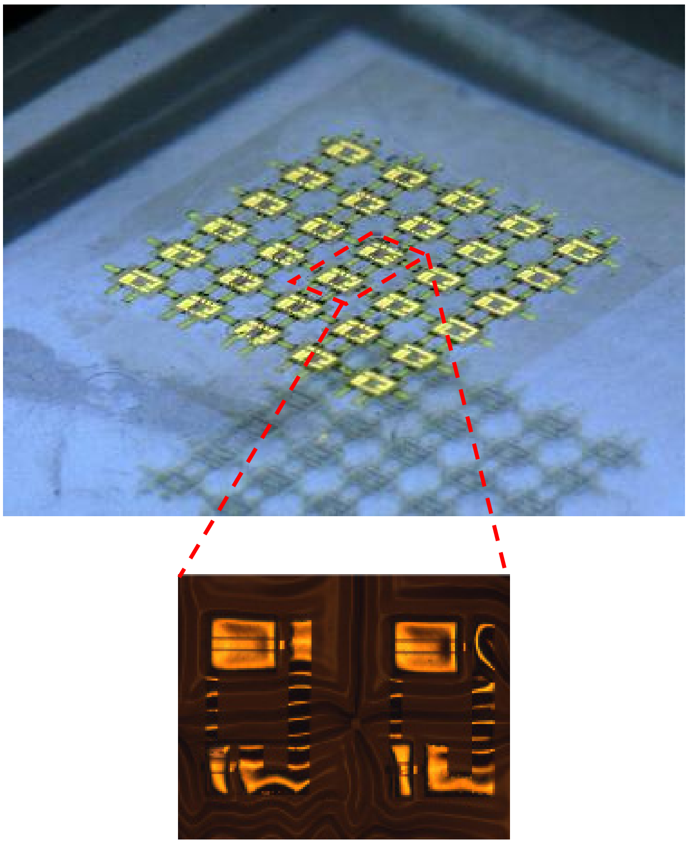

Figure 7-2 Overview of wrinkling pattern

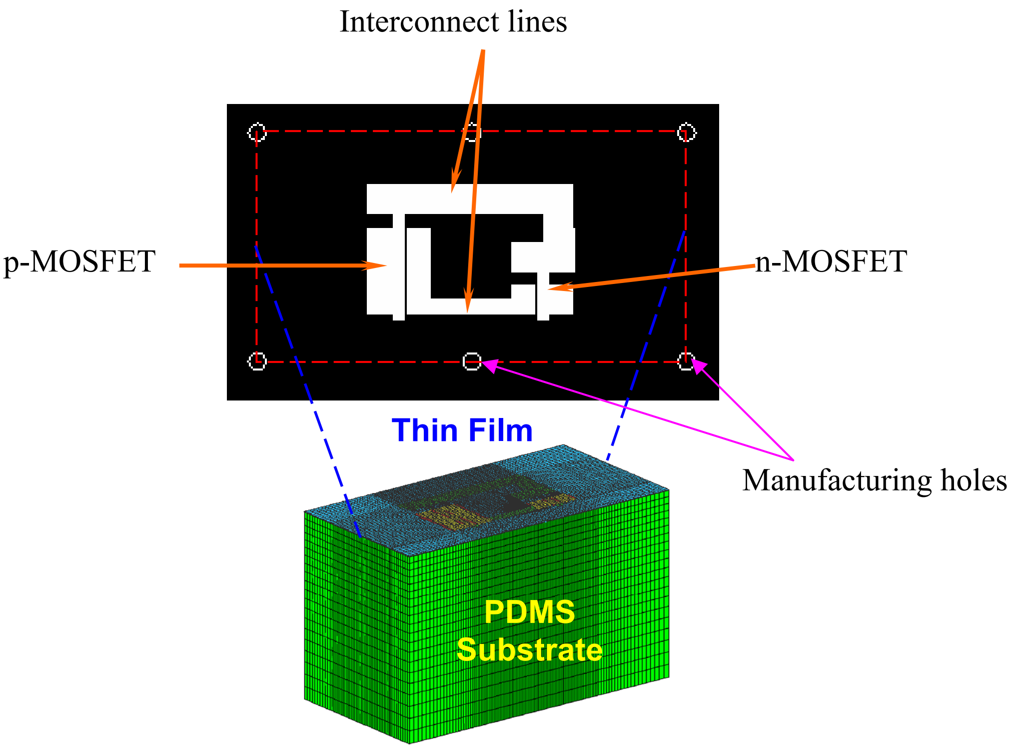

Figure 7-3 CAD drawing and FE mesh of integrated circuits and substrate

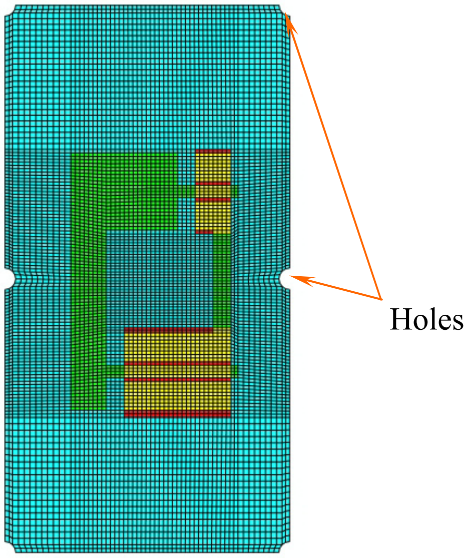

Figure 7-4 Finite element mesh of thin film

Each layer of thin film (Si-CMOS/PI system) is modeled as linear elastic and the PDMS (184-PDMS) substrate is modeled as nearly incompressible hyperelastic. This hyperelastic material model uses the Neo Hookean constitutive law which accounts for the nonlinearity of the stress-strain relation in a simple way (Figure 7-5). The material properties used in this study are shown in Table 7-1.

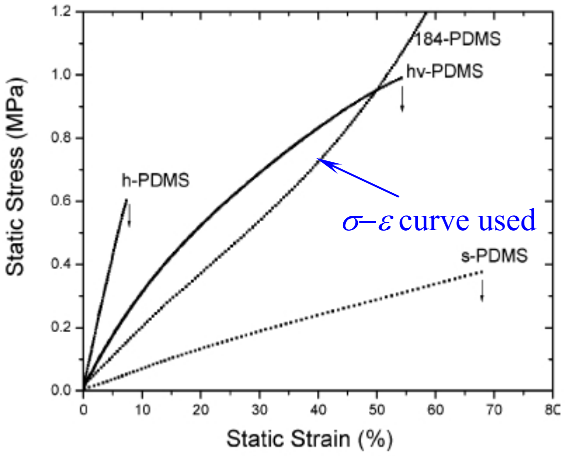

Figure 7-5 Strain-stress curve of PDMS (Choi and Rogers, 2003)

Table 7-1 Materials properties of the thin film and substrate

Materials	Young’s modulus (MPa)	Poisson’s ratio
PI	2,500	0.34
Metal (Cr-Au-Cr)	78,000	0.44
Si	130,000	0.27
SiO_2	70,000	0.17
PDMS	1.8	0.48

7.2 3-D Simulation Process

The numerical simulation studies performed in the same procedure as the key fabrication steps of thin film with ultrathin CMOS circuits. Figure 7-6 shows the numerical simulation stages with finite element mesh used.

The buckling mode shape is determined by an eigenvalue analysis using the 3D FE model with a multilayer thin film (Si-CMOS/PI system) and compliant PDMS substrate. To obtain wrinkling modes, the traction force is found using the same method as in the 2D simulation (Section 6.1.1).

After computing the buckling mode-shapes, the selected eigenmodes are introduced into the structure as a geometrical imperfection. The first eigenmode is used as an initial small geometrical imperfection to trigger the buckling of the system. The random combinations of various buckling modes are also used, and it is found that the values for the wavelength and amplitude are independent of the modes. The scaling value of imperfection takes 1% to 5% of thin film thickness. The substrate (without the thin film), with the effect of an introduced imperfection expands due to an increase in temperature (thermal loading). When the temperature reaches 160 °C (~3.9% prestrain in substrate), the multi-layer thin film (shell elements) forms a bond to the PDMS substrate (solid elements). As the temperature decreases, the simulation shows that the thin film buckles with the shrinking of the substrate using the non-linear analysis.

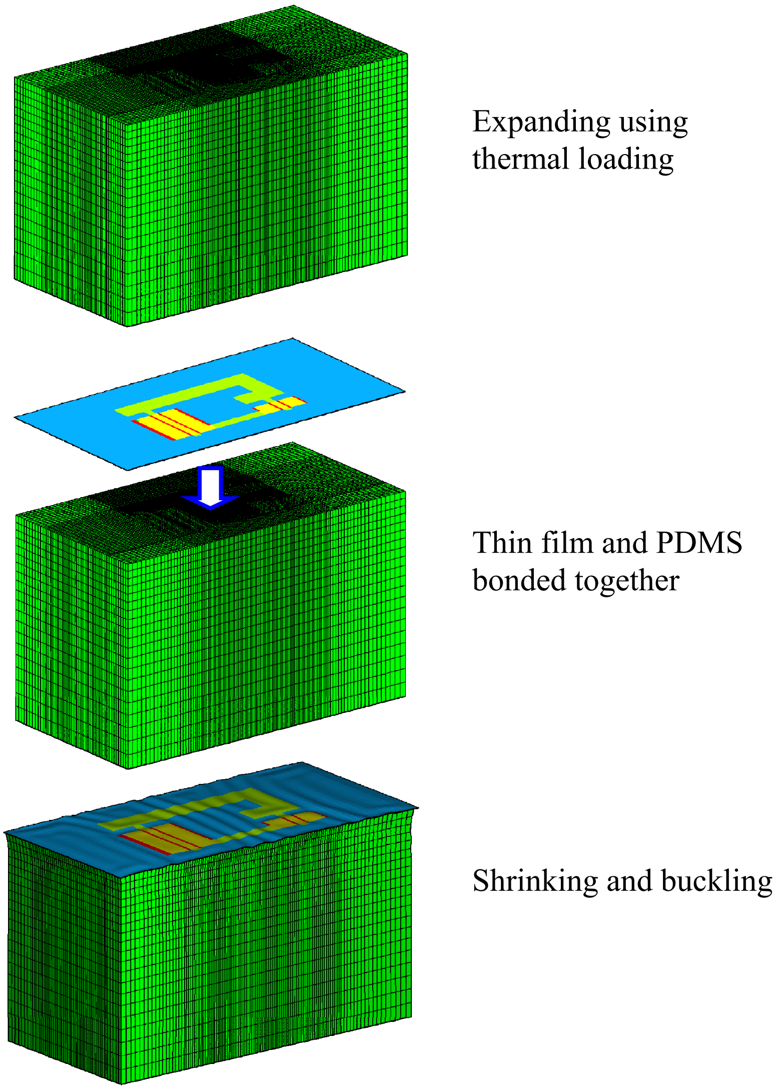

Figure 7-6 Finite element simulation process

The first wrinkle forms almost as soon as the thermal load is applied, and this leads to the formation of a second one, and so on until a large number of wrinkles have formed. As in the 2D simulation study, fictitious viscous forces are applied as the stabilization factor. To achieve good accuracy this parameter is set to the lowest possible value for which numerical convergence can still be achieved. The value used in 2D study, i.e.2×10^{-4}, is found to be also suitable in this 3D simulation. This model requires a higher number of elements to achieve reasonably good accuracy. The size of the current finite element model is ~200 thousand elements and large enough to accommodate for the buckling pattern i.e. wavelength and amplitude. The element size is based on the 2D finite element model which convergence study has been done. These simulations give an insight into the formation of buckling patterns, the mechanical behavior of the thin film.

7.3 Simulations Results

The numerical simulations are performed on a SGI Altix 3700 BX2 consisting of 128 Intel Itanium 2 processors and 768GB of shared memory. The computational time of 3D FE simulation ranges from 24 hours to a few days depending on prestrain value.

7.3.1 Growth of Thin Film Wrinkles

The wavy thin film within the silicon integrated circuit has complex patterns associated with nonlinear buckling physics in a mechanically heterogeneous system. Figure 7-7 shows the images of wrinkle forming and growing based on the results of 3D FE analysis in comparison with scanning electron micrographs of an integrated circuit sample. It can be found that the waves form most readily in regions of the smallest flexural rigidity: i.e. along the interconnect lines between the $p-$MOSFET and $n-$MOSFET sides of the inverter and the electronically inactive parts of the circuit sheet. Then, upon substrate shrinkage, the waves begin to extend from these locations to other parts of the circuit, including the comparatively rigid device regions.

It should be noted that the etch holes, representative ones of which appear near the centers of these images, have a strong influence on the waves (Figure 7-8). In particular, waves tend to nucleate at these locations; they adopt wave vectors oriented tangential to the perimeters of the holes, due to the traction-free edges at these locations. Cracks could be formed, most commonly in the metal electrodes near the etch holes, when local strains rise to 1-2%.

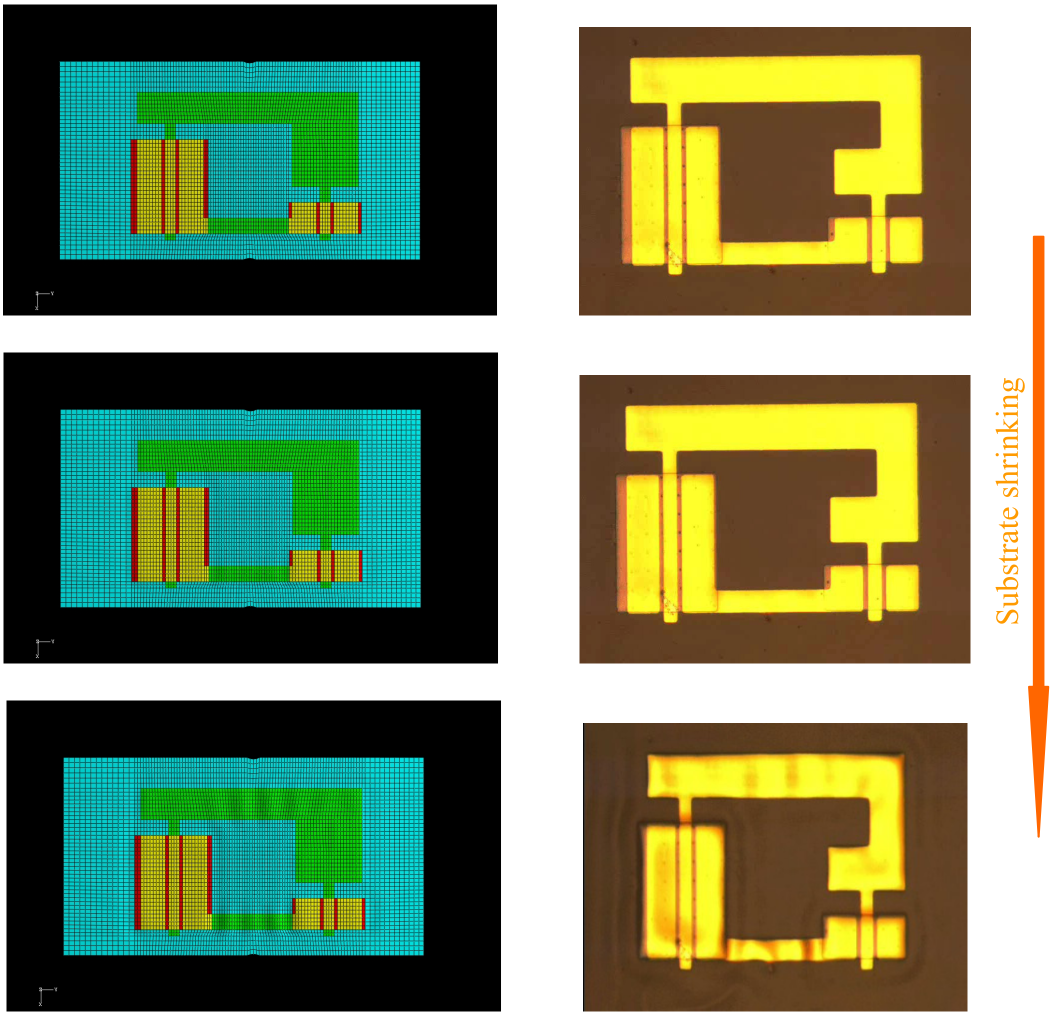

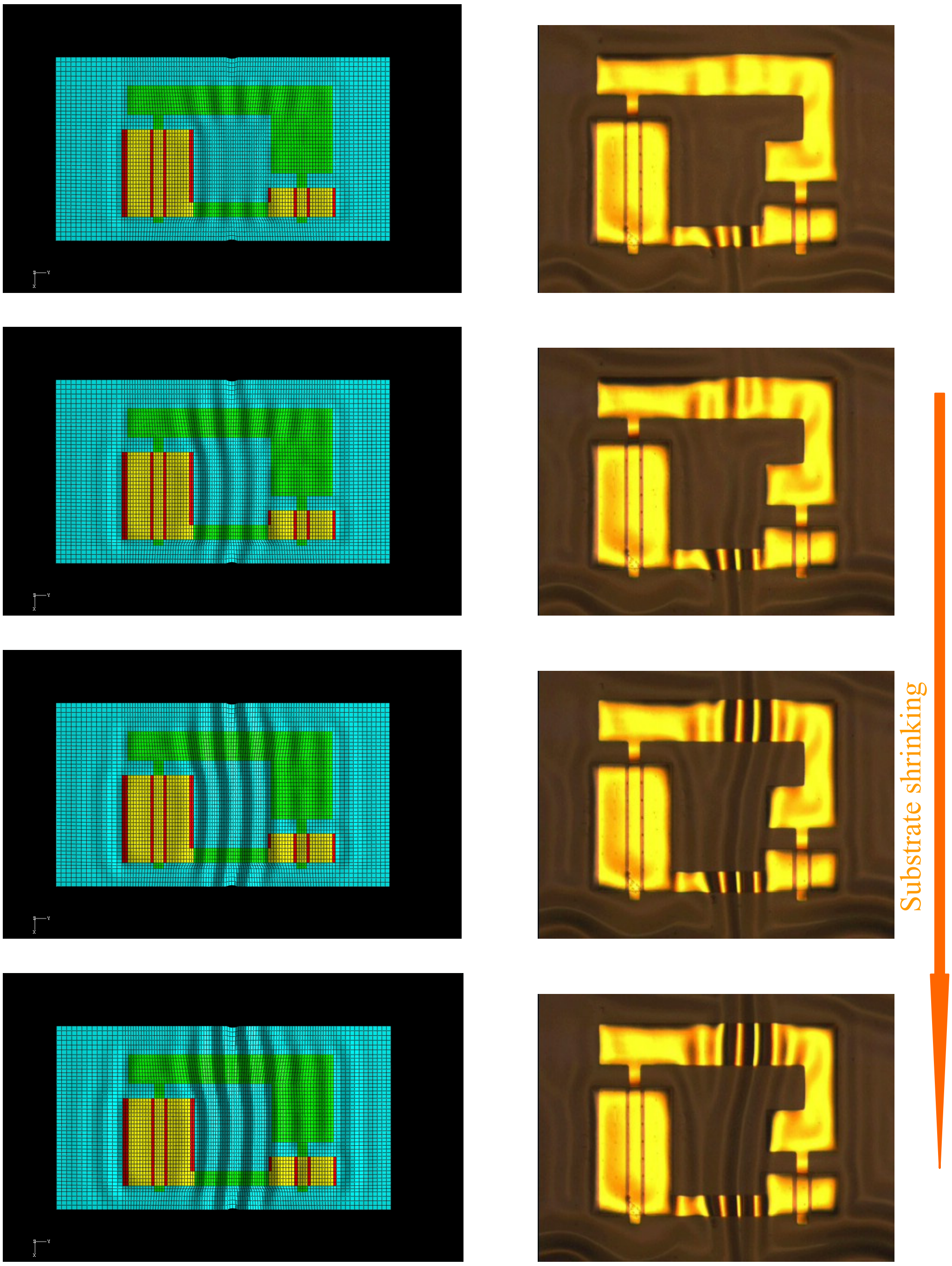

(a) Numerical simulation (b) Experimental images

Figure 7-7 Wrinkle forming due to substrate shrinking

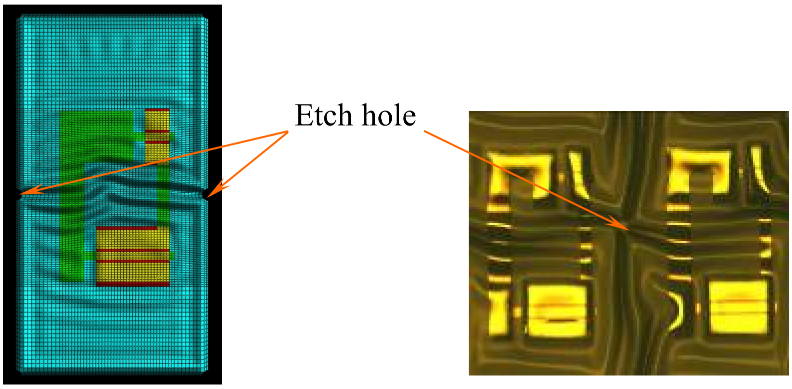

Numerical Simulation

Experimental image

Figure 7-8 Wavy pattern around etch hole at ε_{pre}=3.9%

Figure 7-9 shows the comparison between the simulation of a wavy pattern and an experimental image. The wavy Si-CMOS inverters formed with ε_{pre}=3.9%. The simulation and experimental images for ε_{pre}=2.7% and 5.7%, are shown in Figure 7-10, respectively.

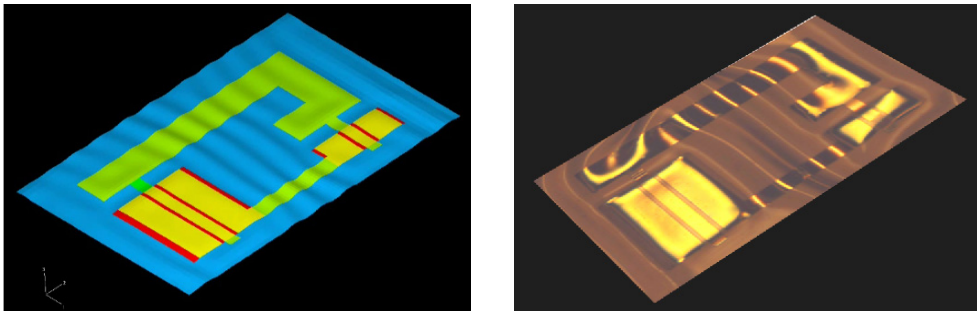

(a) Numerical simulation

(b) Experimental image

Figure 7-9 Comparison of wrinkle pattern at ε_{pre}=3.9%

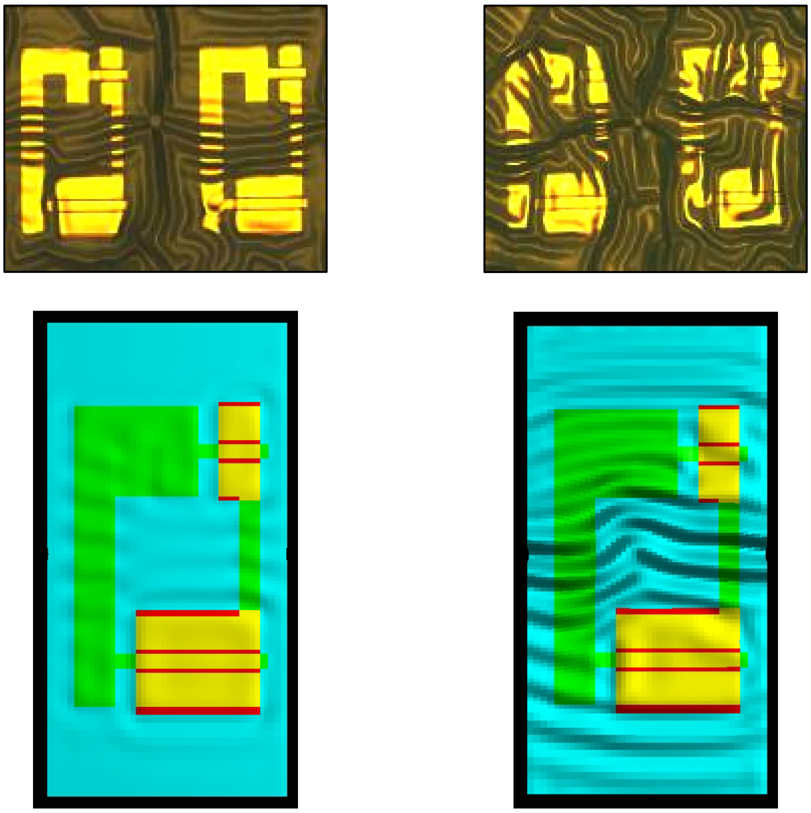

(a) ε_{pre}=2.7% (b) ε_{pre}=5.7%

Figure 7-10 Comparison of wrinkle pattern observed through numerical simulation (top) and experimental optical micrographs (bottom)

Figures 7-7 to 7-10 show that the correspondence between the simulated and experimental results of the wrinkling pattern is remarkably good, The slight differences that are present are due to the sensitivity of the buckling patterns to the precise location and detailed shapes of the etch holes, and some uncertainties in the mechanical properties of the various layers. One may conclude that the wrinkle behaviour of this type of thin film is well represented qualitatively by numerical simulation using the FEM. For quantitative comparison, the focus is on the wavelength and amplitude as presented in the next section.

7.3.2 Wavelength and Amplitude of Wrinkled Thin Film

The wrinkling behaviour can be quantitatively captured using the FE simulation. The available experimental data are wavelength and amplitude (Chapter Three), and thus they are used to validate the FEM results. Numerical simulation indicates that the $p-$MOSFET and $n-$MOSFET regions adopt periods between 160 and 180 μm and that the metal interconnects adopt periods between 90 and 110 μm, and the amplitude in the metal interconnects is around 6-8 μm. These observations are all quantitatively consistent with experimental results (Figure 7-11). For a clearer view, the deformation scaling factor is set to 5 in Figure 7-11.

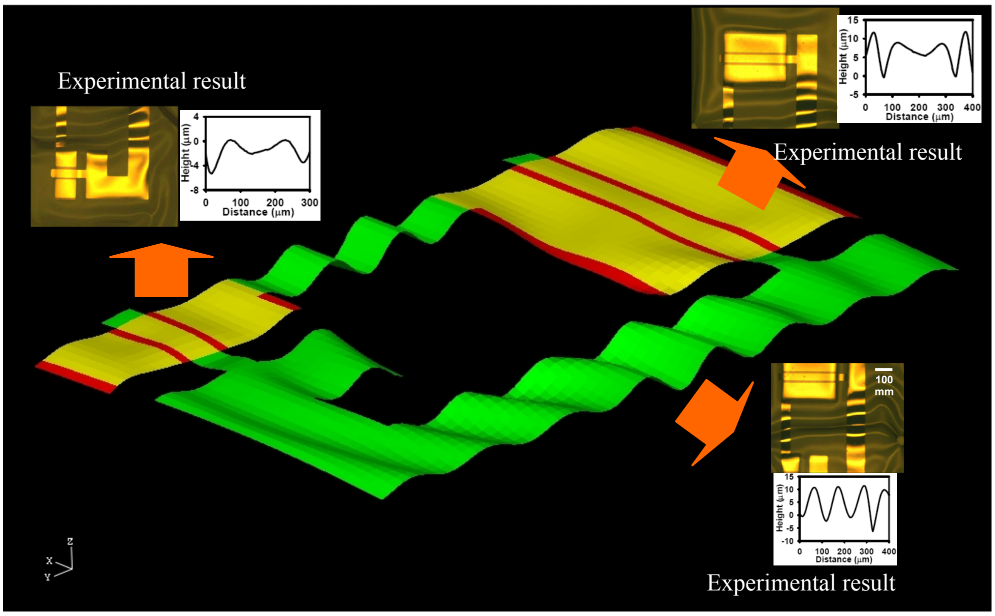

Figure 7-11 Comparison of wavelength and amplitude between numerical results and experimental data for ε_{pre}=3.9%

7.3.3 Stress and Strain in Wrinkled Thin Film

It is necessary to determine the strain or stress of thin film, since the maximum strain or stress is an important failure criterion for the thin film under stretching. The advantage of numerical simulation is that it can give insight into the details of wavy thin films, such as the stress and strain distribution in the materials used, unlike in experiments whereby such data are difficult to measure. This will help researchers to understand and evaluate the behavior in the thin film in the whole process of fabrication.

Figures 7-12 and 7-13 show the distribution of maximum principal strains on the top-surface in the metal and Si layer, respectively for three prestrains. The strain limits are set at minimum = 0.0 % and maximum= 0.1 % in order to better visualize the strain variation. The general trend is that the strain increases with increasing prestrain. In the metal layer, the maximum principal strain is located along the edge of interconnect between the $p-$MOSFET and the $n-$MOSFET at the peak of the wave. This is the sum of the membrane strain and the bending strain induced by the buckled geometry. In the Si layer of the $p-$MOSFET and $n-$MOSFET, the maximum principal strain appears at edge of the $n-$MOSFET, which is connected to the interconnect. The maximum principal strain does not exceed 0.4% for both layers in the case of 5.7% prestrain.

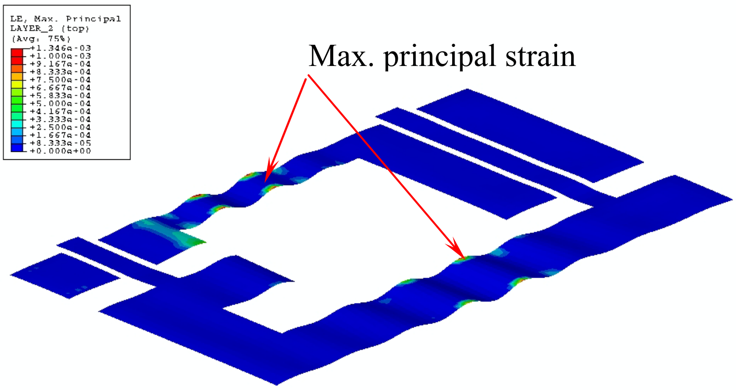

(a) 2.7% prestrain

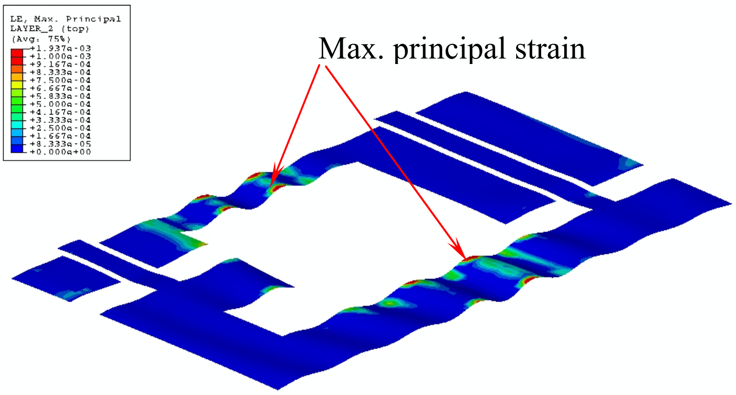

(b) 3.9% prestrain

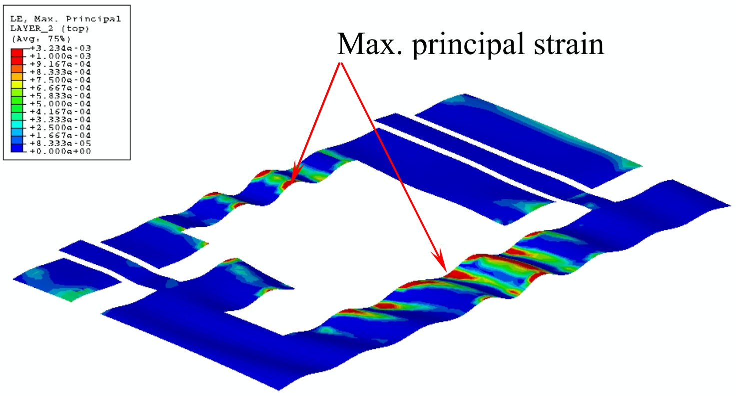

(c) 5.7% prestrain

Figure 7-12 Maximum principle strain on top-plane of metal layer

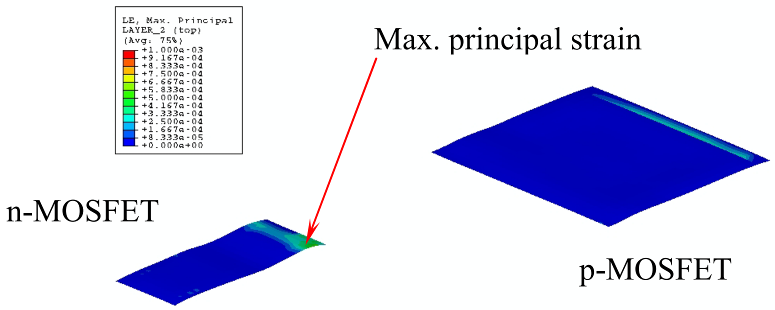

(a) 2.7% Prestrain

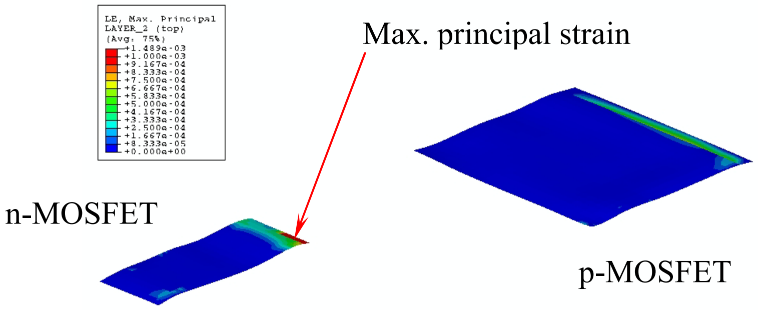

(b) 3.9% Prestrain

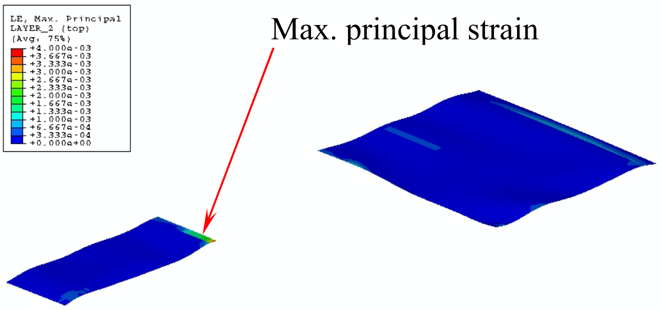

(c) 5.7% Prestrain

Figure 7-13 Maximum principle strain on top-plane of Si layer

As wrinkling is associated with the existence of stress, it is beneficial to consider the distribution of the Von Mises stress, shown in Figures 7-14 and 7-15 for the metal and Si layer. The maximum Von Mises stress occurs at valley of wavy interconnect between $p-$MOSFET and $n-$MOSFET for metal layer and at the corner on Si layer of $p-$MOSFET. The stress values are 850 N/mm^2 and 650 N/mm^2 for the metal and Si layers respectively, for 5.7% prestrain.

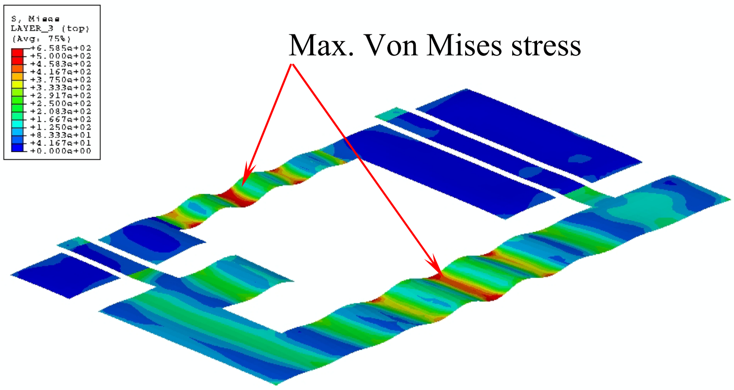

(a) 2.7% Prestrain

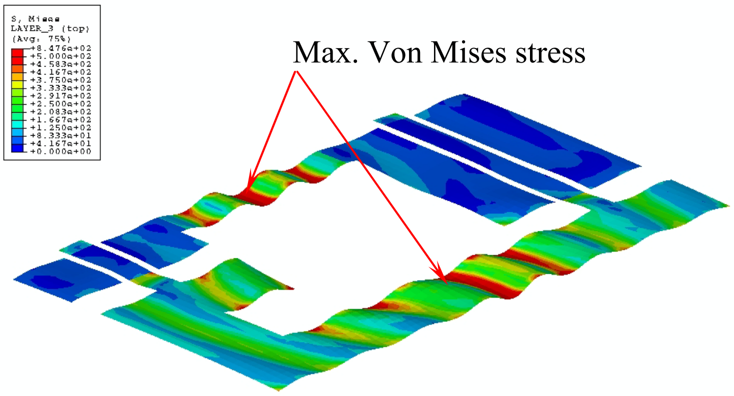

(b) 3.9% Prestrain

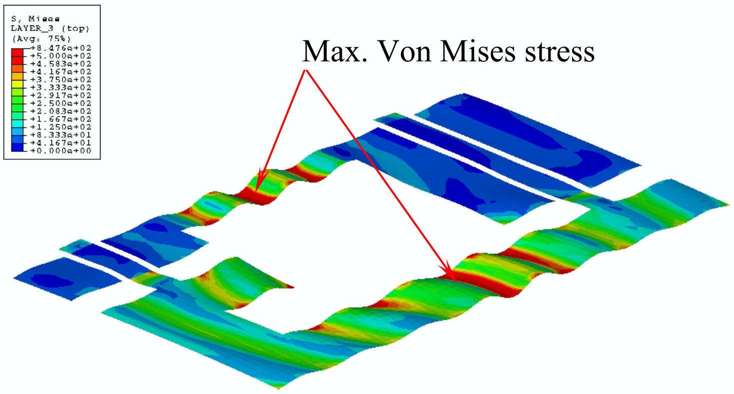

(c) 5.7% Prestrain

Figure 7-14 Von Mises Stress on top-plane of metal layer

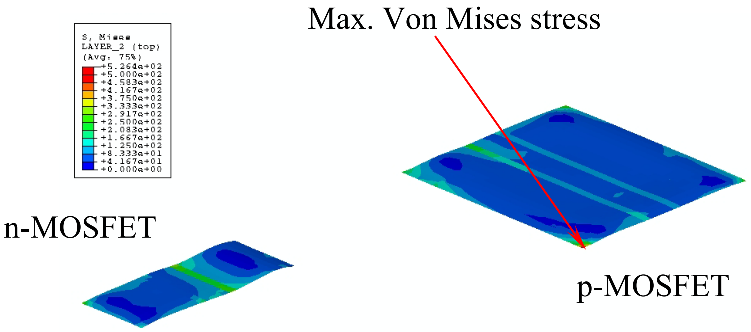

(a) 2.7% Prestrain

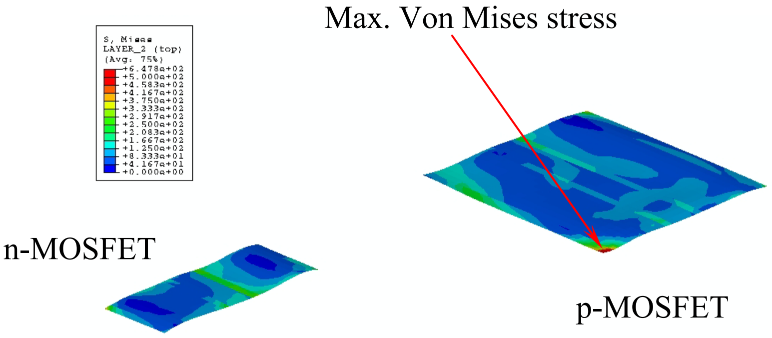

(b) 3.9% Prestrain

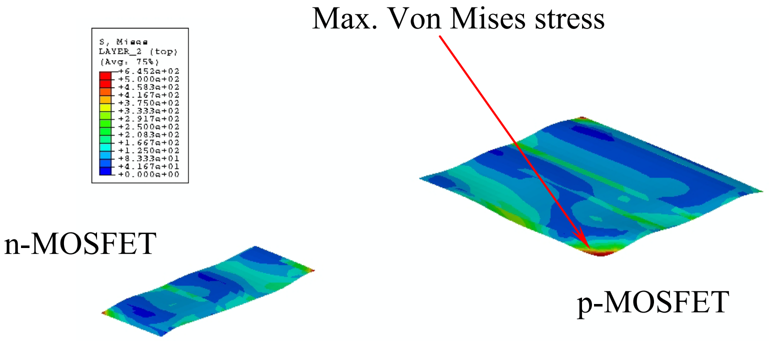

(c) 5.7% Prestrain

Figure 7-15 Von Mises stress on top-plane of Si layer

In this Chapter, 3D FE simulation of wrinkled thin film has been performed, and the accuracy of the resulting wrinkle patterns has been demonstrated for different prestrain values. The geometrical imperfections seeded in the initially flat thin film are obtained by computing the initial buckling modes of a perfectly flat thin film. The quadrilateral finite-membrane-strain thin-shell element is found to be suitable to handle the combination of membrane and bending behavior associated with wrinkling. The mesh density, about ten elements over a completely wrinkled wave of length 100μm, is found sufficient to obtain accurate results. The numerical simulation has accurately reproduced the experimental behavior of the thin films and enables us to compute the maximum strain and stress in the electronic device. The numerical simulation results show this type of stiff thin film-compliant substrate system can geometrically accommodate large mechanical deformations without inducing significant strains and stress in the materials themselves. The numerical strategy can be used to assist development of stretchable stiff thin film-compliant substrate system. The numerical simulation hence serves as a useful tool to allow engineers to design stretchable/compressible electronics for different applications.

Chapter Eight

Conclusions and Recommendation for Further Work

8.1 Conclusions

The fabrication process of various types of stretchable silicon systems has been investigated for both single crystal silicon ribbon and silicon integrated circuits on compliant substrate. It is shown that stiff thin films become unstable and buckle when the substrate shrinks in the fabrication process. The traction forces at the interface between two materials contribute to thin film instability and form wavy patterns. In particular, the wrinkle pattern has been monitored by optical images and scanning electron micrograph and measured experimentally by means of atomic force microscopy. Experimental data revealed the wavelength and amplitude of wrinkled thin film, as well as other details of the mechanical behavior of buckled thin films on a compliant substrate. It is shown that stretchability and foldability can be achieved in high performance integrated circuits by use of new structural configurations, even when using intrinsically brittle electronic materials. The stretchable electronics systems use new material structures, rather than new materials, to accomplish the desired mechanical attributes. Such material structures are designable and offer the possibility of direct integration of electronics with biological systems, medical prosthetics and monitoring devices, complex machine parts, and mechanically rugged, lightweight packages, etc.

Theoretical studies are performed on the instability of stretchable stiff thin film-compliant substrate systems. A linear analytical solution has been constructed for single crystal silicon ribbon on a compliant substrate. Theoretical modeling performed in a manner based on certain approximations implemented in the models of this class of system, e.g. infinite length for the silicon ribbon and plain strain for substrate. The analytical results quantitatively reproduce the experimental observations. The silicon ribbon is still rigid and brittle as an intrinsic material with "accordion bellows" geometry when bonded to a compliant substrate, but the overall structure is stretchable. The strains in this structure are accommodated for through changes in the amplitude and wavelength of the buckled geometries. These results and the detailed analyses are important for the many intended applications of wrinkled stiff thin film-compliant substrate system.

A finite-deformation buckling theory is established for a stiff thin film on compliant substrates. This analysis is different from linear buckling analyses in three aspects: finite geometry change, finite strain, and non-linear constitutive model. A perturbation method is used to obtain an analytical solution, and this is validated using the finite element method (FEM). The analytical solution and numerical results show that the wavelength and amplitude of the strain-dependent wrinkled thin film both agree well with experimental observation in the absence of any parameter fitting. The peak and membrane strains in thin films are obtained analytically, so too are the stretchability and compressibility of the system. These conclusions and the detailed analyses are important for the many envisioned applications for buckled stiff thin film-compliant substrate system.

The amplitude and wavelength of an infinite length single crystal silicon ribbon, qualitatively obtained through analytical solution, agree well with experimental observations. However, for the more general case, analytical solutions are not possible in some regions, e.g. finite length silicon ribbon and the flat region around the edges of buckled thin films on compliant substrates resulting from traction-free edges. Numerical analyses have to be performed using the FEM. The finite element simulation results represent well the wrinkling effect in stretchable silicon systems. Using two-dimensional FE simulation, it is found that the edge-effect length, L_{edge}, is proportional to the thin-film thickness and decreases with an increase in prestrain and substrate Young's modulus. Such results could provide useful design guidelines for implementation of these edge regions in certain classes of applications in stretchable electronics and other materials-based disciplines. For example, well-placed edges can lead to flat regions in a larger scale buckled system where, for instance, planarity is required for efficient photodetection or other similar functions.

The three-dimensional FE simulation has been applied to a silicon integrated circuit on a compliant substrate. The Si-CMOS/PI thin film system was analysed by numerical simulation, and the studies performed provide insight into the formation of buckling patterns, the mechanical behavior of the thin film and the nested hierarchy of the structure. The simulation results exhibit similar buckling patterns as experimental observations and provide important information in the design of stretchable electronic systems. For example, the expanded ranges of stretchability can reach up to 30% of their original dimensions. These mechanical criteria could be used in the development of new classes of electronic devices.

The wrinkling details in both single crystal silicon and silicon integrated circuits have been studied using analytical and numerical methods. These classes of stiff thin film-compliant substrate system can geometrically accommodate large mechanical deformations without causing significant strains in the materials themselves. The study shows that the instability and buckling analysis of stretchable silicon systems is an interesting and important area with many exciting research possibilities and viable applications in the broader field of unusual electronics devices.

8.2 Recommendation for Future Work

The research reported herein shows that there are many intriguing aspects of instability in stretchable silicon systems, from fundamental theoretical work to electronic applications. Future work is recommended to focus on the following areas:

(1) Extension of mechanical concepts to expanded ranges of stretchability for other material types.

(2) Application of alternative stretchable materials in new classes of electronic devices.

(3) Exploration of mechanical theory applied to, for example, the deformation of a silicon strip under diagonal stretching caused by lateral buckling, and a delamination of a thin film after buckling.

(4) Development of numerical methods to effectively simulate encapsulated integrated circuits.

(5) Design optimization of stretchable silicon integrated circuits.

References

ABAQUS Inc. (2007). ABAQUS Analysis User's Mannual V6.7.

Ahmad, S.; Iron, B.M. and Zienkiewicz, O.C. (1970). Analysis of Thick and Thin Shell Structure by Curved Element. *International Journal for Numerical Methods in Engineering*. Vol. 2, pp. 419-451.

Ahn, J.H.; Kim, H.S.; Lee, K.J.; Zhu, Z.; Menard, E.; Nuzzo, R.G. and Rogers, J.A. (2006). High Speed, Mechanically Flexible Single-Crystal Silicon Thin-Film Transistors on Plastic Substrates. *IEEE Electron Device Letters*. Vol. 27, No. 6, pp. 460-462.

Allen, H.G. (1969). *Analysis and Design of Structural Sandwich Panels*. Pergamon Press, New York. 283 pp.

Audoly, B. (2000). Mode-Dependent Toughness and Delamination of Compressed Thin Films. *Journal of the Mechanics and Physics of Solids*. Vol. 48, pp. 2315–2332.

Baca, A.J.; Ahn, J.H.; Sun, Y.; Meitl, M.A.; Menard, E.; Kim, H.S.; Choi, W.M.; Kim, D.H.; Huang, Y. and Rogers, J.A. (2008). Semiconductor Wires and Ribbons for High-Performance Flexible Electronics. *Angewandte Chemie International Edition*. Vol.47, pp.5524–5542.

Belytschko, T.; Liu, W.K. and Moran, B. (2000). *Nonlinear Finite Elements for Continua and Structures*. John Wiley, Chichester, New York. 650 pp.

Ben Amar, M. and Pameau, Y. (1997). Crumpled Paper. *Proceedings of the Royal Society of London – A*. Vol. 453, No. 1959, pp. 729–755.

Bowden, N.; Brittain, S.; Evans, A.G.; Hutchinson J.W. and Whitesides, G.M. (1998). Spontaneous Formation of Ordered Structures in Thin Films of Metals Supported on an Elastomeric Polymer. *Nature*. Vol. 393, pp. 146-149.

Bowden, N.; Huck, W.T.S.; Paul K.E. and Whitesides, G.M. (1999). The Controlled Formation of Ordered, Sinusoidal Structures by Plasma Oxidation of an Elastomeric Polymer. *Applied Physics Letters*. Vol. 75, pp. 2557-2559.

Brush, D.O. and Almroth, B.O. (1975). *Buckling of Bars, Plates and Shells*. McGraw-Hill Inc, New York. 378pp.

Chen, X. and Hutchinson, J.W. (2004a). A Family of Herringbone Patterns in Thin Films. *Scripta Materialia*. Vol. 50, pp. 797–801.

Chen, X. and Hutchinson, J.W. (2004b). Herringbone Buckling Patterns of Compressed Thin Films on Compliant Substrates. *Journal of Applied Mechanics-Transactions of the ASME*. Vol. 71, pp.597-603.

Cerda, E. and Mahadevan, L. (2003). Geometry and Physics of Wrinkling. *Physical Review Letters*. Vol. 90, 074302.

Choi, K.M. and Rogers, J.A. (2003). A Photocurable Poly(dimethylsiloxane) Chemistry Designed for Soft Lithographic Molding and Printing in the Nanometer Regime. *Journal of the American Chemical Society*. Vol. 125, No. 14, pp. 4060-4061.

Choi, W.M.; Song, J.; Khang, D.Y.; Jiang, H.; Huang, Y.; Rogers, J.A.; (2007). Biaxially Stretchable "Wavy" Silicon Nanomembranes. *Nano Letters*. Vol. 7, No. 6, pp.1655-1663.

Crawford, G. P. (ed.). (2005). *Flexible Flat Panel Display Technology*. Wiley-SID Series in Display Technology. England. John Willey & Sons Ltd. 528pp.

Crone, B.; Dodabalapur, A.; Lin, Y.Y.; Filas, R.W.; Bao, Z.; LaDuca, A.; Sarpeshkar, R.; Katz H.E. and Li, W. (2000). Large-Scale Complementary Integrated Circuits Based on Organic Transistors. *Nature*. Vol. 403, pp. 521-523.

Dinyari, R. Rim, S.B.; Huang, K.; Catrysse, P.B. and Peumans, P. (2008). Curving Monolithic Silicon for Nonplanar Focal Plane Array Applications. *Applied Physical Letters*. Vol. 92, 091114.

Duan, X.; Niu, C.; Sahi, V.; Chen, J.; Parce, J.W.; Empedocles, S. and Goldman, J.L. (2003). High-Performance Thin-Film Transistors using Semiconductor Nanowires and Nanoribbons. *Nature*. Vol. 425, pp. 274-278.

Efimenko, K.; Rackaitis, M.; Manias, E.; Vaziri, A.; Mahadevan L. and Genzer, J. (2005). Nested Self-Similar Wrinkling Patterns in Skins. *Nature Materials*. Vol. 4, pp. 293-297.

Flanagan, D. P. and Belytschko, T. (1981). A Uniform Strain Hexahedron and Quadrilateral with Orthogonal Hourglass Control. *International Journal For Numerical Methods in Engineering*. VOL. 17, pp. 679-706.

Fu, Y.Q.; Sanjabi, S.; Barber, Z.H.; Clyne, T.W.; Huang, W.M.; Cai, M.; Luo, J.K.; Flewitt A.J. and Milne, W.I. (2006). Evolution of Surface Morphology in TiNiCu Shape Memory Thin Films. *Applied Physics Letters*. Vol. 89, 171992.

Gioia, G. and Ortiz, M. (1997). Delamination of compressed thin films. *Advances in Applied Mechanics*. Vol. 33, pp.119-192.

Greene, K. (2006). 10 Emerging Technologies, MIT Technology Review. 16 pp.

Groenewold, J. (2001). Wrinkling of Plate Coupled with Soft Elastic Media. *Physica A*. Vol. 298, pp. 32-45.

Hadi, B.K. (2001). Wrinkling of Sandwich Column: Comparison between Finite Element Aanalysis and Analytical solutions. *Composite Structures*. Vol. 53, pp. 477-482.

Harris, A.K.; Wild P. and Stopak D. (1980). Silicone Rubber Substrata: A New Wrinkle in the Study of Cell Locomotion. *Science*. Vol. 208, No. 4440, pp. 177-179.

Harrison, C.; Stafford, C.M.; Zhang, W.H.; Karim, A. (2004). Sinusoidal Phase Grating Created by Tunably Buckled Surface. *Apply Physics Letters*. Vol. 85, No. 18, pp. 4016-4018.

Huang, R. (2005). Kinetic Wrinkling of an Elastic Film on a Viscoelastic Substrate. *Journal of the Mechanics and Physics of Solids*. Vol. 53, pp. 63-89.

Huang, R. and Suo, Z. (2002). Instability of a Compressed Elastic Film on a Viscous Layer. *International Journal of Solids and Structures*. Vol. 39, 1791-1802.

Huang, Z.Y.; Hong, W. and Suo, Z. (2004). Evolution of wrinkles in hard films on soft substrates. Physical Review E Vol. 70, 030601.

Huang, Z.Y.; Hong, W. and Suo, Z. (2005). Nonlinear Analysis of Wrinkles in a Film Bonded to a Compliant Substrate. *Journal of the Mechanics and Physics of Solids*. Vol. 53, pp. 2101-2118.

Huck, W.T.S.; Bowden, N.; Onck, P.; Pardoen, T.; Hutchinson J.W. and Whitesides, G.M. (2000). Ordering of Spontaneously Formed Buckles on Planar Surfaces. *Langmuir*. Vol. 16, pp. 3497-3501.

Hung P.J.; Jeong, K.; Liu, G.L. and Lee, L.P. (2004) Microfabricated Suspensions for Electrical Connections on the Tunable Elastomer Membrane. *Applied Physics Letters*. Vol. 85 No.24, 6051.

Hutchinson, J.W. and Suo, Z. (1991). Mixed-Mode Cracking in Layered Materials. *Advances in Applied Mechanics*. Vol.29, pp. 63–191.

INSPEC. (1988). *Properties of Silicon*. Institution of Electrical Engineers, New York. 1100 pp.

Jiang, H.; Khang, D.Y.; Fei, H.; Kim, H.; Huang, Y.; Xiao, J. and Rogers J.A. (2008). Finite Width Effect of Thin-Films Buckling on Compliant Substrate: Experimental and Theoretical Studies. *Journal of the Mechanics and Physics of Solids*. Vol. 56, No. 8, pp. 2585-2598.

Jiang, H.; Khang, D.Y.; Song, J.; Sun, Y.; Huang, Y.; Rogers, J.A. (2007). Finite Deformation Mechanics in Buckled Thin Films on Compliant Supports. *Proceedings of the National Academy of Sciences of the United States of America* Vol. 104, pp. 15607-15612.

Jiang, X.Y.; Takayama, S.; Qian, X.P.; Ostuni, E.; Wu, H.K.; Bowden, N.; LeDuc, P.; Ingber D.E. and Whitesides G.M. (2002). Controlling Mammalian Cell Spreading and Cytoskeletal Arrangement with Conveniently Fabricated Continuous Wavy Features on Poly(dimethylsiloxane). *Langmuir*. Vol. 18, pp. 3273-3280.

Khang, D.Y.; Jiang H.; Huang, Y. and Rogers, J.A. (2006). A Stretchable Form of Single-Crystal Silicon for High-Performance Electronics on Rubber Substrates. *Science*. Vol. 311, pp. 208-212.

Kim, D.H.; Ahn, J.H.; Choi, W.M.; Kim, H.S.; Kim, T.H.; Song, J.; Huang, Y.Y.; Liu, Z.J.; Lu, C. and Rogers, J.A. (2008). Stretchable and Foldable Silicon Integrated Circuits. *Science*. Vol. 320, pp. 507-511.

Ko, H.C.; Stoykovich1, M.P.; Song, J.; Malyarchuk, V.; Choi, W.M.; Yu, C.J.; Geddes, J.B.; Xiao, J.; Wang, S.; Huang, Y. and Rogers, J.A. (2008). A

Hemispherical Electronic Eye Camera Based on Compressible Silicon Optoelectronics. *Nature*. Vol. 454, pp. 748-753.

Koh C.G. and Kelly, J.M. (1989). Compression Stiffness of Bonded Square Layers of Nearly Incompressible Material. *Engineering Structures*. Vol. 11, pp. 9-11.

Koh, C.G. and Lim, H.L. (2001). Analytical Solution for Compression Stiffness of Bonded Rectangular Layers. *International Journal of Solids and Structures*. Vol. 38, pp. 445-455.

Lacour, S.P.; Jones, J.; Wagner, S.; Li, T. and Suo, Z. (2004). Stretchable Interconnects for Elastic Electronic Surfaces. *Proceedings of the IEEE.* Vol. 93, pp. 1459-1467.

Lacour, S.P.; Wagner, S.; Narayan, R.J.; Li, T. and Suo, Z. (2006). Stiff Subcircuit Islands of Diamondlike Carbon for Stretchable Electronics. J*ournal of Applied Physics* Vol.100, 014931.

Lee, C.H.; Sazonov, A.; Robertson, J.; Nathan, A.; Esmaeili-Rad, M.R.; Servati, P. and Milne, W.I. (2006). How to Achieve High Mobility Thin Film Transistors by Direct Deposition of Silicon Using 13.56 MHz RF PECVD? *IEEE International Electron Devices Meeting, IEDM '06.* pp. 295-299.

Lobkovsky, A.; Gentges, S.; Li, S.H.; Morse, D. and Witten, T. (1995). Scaling Properties of Stretching Ridges in a Crumpled Elastic Sheet. *Science* Vol. 270, pp. 1482-1484.

Loo, Y.L.; Someya, T.; Baldwin, K.W.; Bao, Z.; Ho, P.; Dodabalapur, A.; Katz, H.E. and Rogers, J.A. (2002). Soft, Conformable Electrical Contacts for Organic Semiconductors: High-Resolution Plastic Circuits by Lamination. *The Proceedings* *of the National Academy of Science of the United States of America*. Vol. 99, pp. 10252-10256.

Lumelsky, V.; Shur, M.S. and Wagner, S. (2001). Sensitive Skin. *IEEE Sensors Journal*. Vol. 1, No. 1, pp. 41-51.

Mack, S.; Meitl, M.A.; Baca, A.J.; Zhu, Z.T. and Rogers, J.A. (2006). Mechanically Flexible Thin-Film Transistors that Use Ultrathin Ribbons of Silicon Derived from Bulk Wafers. *Applied Physics Letters*. Vol. 88, 213101.

Maikap, S.; Liaoa, M.H.; Yuana, F.; Leeb, M.H.; Huang, C.F.; Chang, S.T. and Liu, C.W. (2004). Package-Strain-Enhanced Device and Circuit Performance. *IEEE International Electron Devices Meeting, IEDM'04.* pp. 233-236.

Meitl, M.A.; Zhu, Z.T.; Kumar, V.; Lee, K.J.; Feng, X.; Hunag, Y.; Adesida, I.; Nuzzo, R.G.; and Rogers, J.A. (2006). Transfer Printing by Kinetic Control of Adhesion to an Elastomeric Stamp. *Nature Materials.* Vol. 5, pp.33-38.

Menard, E.; Lee, K.J.; Khang, D.Y.; Nuzzo R.G. and Rogers, J.A. (2004). A Printable form of Silicon for High Performance Thin Film Transistors on Plastic Substrates. *Applied Physics Letters*. Vol. 84, No. 26, pp. 5398-5400.

Moon, M.W.; Lee, S.H. Sun, J.Y.; Oh, K.H.; Vaziri A. and Hutchinson, J.W. (2007). Wrinkled Hard Skins on Polymers Created by Focused Ion Beam. *The Proceedings of the National Academy of Sciences of the United States of America.* Vol. 104, No. 4, pp. 1130-1133.

Moroz, V.; Strecker, N.; Xu, X.P.; Lee, S and Bork, I. (2003). Modeling the Impact of Stress on Silicon Processes and Devices. *Materials Science in Semiconductor Processing*. Vol. 6, pp. 27-36.

Nathan, A.; Park, B.; Sazonov, A.; Tao, S.; Chan, I.; Servati, P.; Karim, K.; Charania, T.; Striakhilev, D.; Ma, Q. and Mruthy, R.V.R. (2000). Amorphous Silicon Detector and Thin Film Transistor Technology for Large-Area Imaging of X-rays. *Microelectronics Journal*. Vol. 31. pp. 883-891.

Niu, K. and Talreja, R. (1999). Modelling of Wrinkling in Sandwich Panels under Compression. *Journal of Engineering Mechanics*. Vol. 125, No. 8, pp. 875-883.

Ohzono, T. and Shimomura, M. (2005). Geometry-Dependent Stripe Rearrangement Processes Induced by Strain on Preordered Microwrinkle Patterns. *Langmuir*. Vol. 21, pp. 7230-7237

Rogers, J.A. (2001). Toward Paperlike Displays. *Science*. Vol. 291, No. 5508, pp. 1502-1503.

Saif, M.T.A. and MacDonald, N.C. (1996). Micro Mechanical Single Crystal Silicon Fracture Studies-Torsion and Bending. *Proceedings of the IEEE The Ninth Annual International Workshop on Micro Electro Mechanical Systems*, MEMS '96, San Diego, CA, USA. pp 105-109

Sato, K.; Shikida, M.; Yoshioka, T.; Ando, T. and Kawabata T. (1997). Micro Tensile-Test of Silicon Film having Different Crystallographic Orientations. *Proceeding of International Conference on Solid State Sensors and Actuators*, *1997*. TRANSDUCERS '97 Chicago. Vol. 1, pp. 518-521

Schmid, H.; Wolf, H.; Allenspach, R.; Riel, H.; Karg, S.; Michel B. and Delamarche, E. (2003). Preparation of Metallic Films on Elastomeric Stamps and Their Application for Contact Processiong and Contact Printing. *Advanced Functional Materials*. Vol. 13, No. 2, pp. 145-153.

Servati, P. and Nathan, A. (2005). Functional Pixel Circuits for Elastic AMOLED Displays. *Proceedings of the IEEE*. Vol. 93, No. 7, pp. 1257-1264.

Sharp, J.S. and Jones, R.A.L. (2002). Micro-Buckling as a Route towards Surface Patterning. *Advanced Materials*. Vol. 14, No. 11, pp. 799-802.

Sinha, R. (2005).. Philips READIUS; World's First "Rollable Display" Pocket E-Reader Concept. *Mobile Magazine*. http://www.mobilemag.com/content/100/333/C4565/.

Someya, T.; Sekitani, T.; Iba, S.; Kato, Y.; Kawaguchi, H. and Sakurai, T. (2004). A Large-Area, Flexible Pressure Sensor Matrix with Organic Field-Effect Transistors for Artificial Skin Applications. *The Proceedings of the National Academy of Sciences of the United States of America.* Vol. 101, No.24, pp. 9966-9970.

Stafford, C.M.; Guo, S.; Harrison C. and Chiang, M.Y.M. (2005). Combinatorial and High-Throughput Measurements of the Modulus of Thin Polymer Films. *Review of Scientific Instruments*. Vol. 76, 062207.

Stafford, C.M.; Harrison, C.; Beers, K.L.; Karim, A.; Amis, E.J.; Vanlandingham, M.R.; Kim, H.C.; Volksen, W.; Miller R.D. and Simonyi, E.E. (2004). A Buckling-Based Metrology for Measuring the Elastic Moduli of Polymeric Thin Films. *Nature Materials*. Vol. 3, pp. 545-550.

Stafford, C.M.; Vogt, B.D.; Harrison, C. Julthongpiput D. and Huang, R. (2006). Elastic Moduli of Ultrathin Amorphous Polymer Films. *Macromolecules*. Vol. 39, pp. 5095-5099.

Streetman, S.G. and Banerjee, S.K. (1981). *Solid State Electronic Devices*. Pearson, New Jersey.

Sun Y. and Rogers, J.A. (2007a). Inorganic Semiconductors for Flexible Electronics. *Advanced Materials*. Vol. 19, pp. 1897-1916.

Sun, Y. and Rogers, J.A. (2007b). Structural Forms of Single Crystal Semiconductor Nanoribbons for High Performance Stretchable Electronics. *Journal of Materials Chemistry*. Vol. 17, pp. 832-840.

Sun, Y.; Choi, W.M.; Jiang, H.; Huang, Y. and Rogers, J. A. (2006a). Controlled Buckling of Semiconductor Nanoribbons for Stretchable Electronics. *Nature Nanotechnology*. Vol.1, pp. 201-207.

Sun, Y.; Kumar, V.; Adesida, I.; Rogers, J.A. (2006b). Buckled and Wavy Ribbons of GaAs for High-Performance Electronics on Elastomeric Substrate. *Advanced Materials*. Vol. 18, 2857-2862.

Symon, K. (1971). *Mechanics* (3d ed.). Addison-Wesley Pub. Co., Reading, Mass. 639 pp.

Teixeira, A.I.; Abrams, G.A.; Bertics, P.J.; Murphy C.J. and Nealey, P.F. (2003). Epithelial Contact Guidance on Well-Defined Micro- and Nanostructured Substrates. *Journal of Cell Science*. Vol. 116, No.10, pp. 1881-1892.

Thompson, S.E.; Armstrong, M.; Auth, C.; Alavi, M.; Buehler, M.; Chau, R.; Cea, S.; Ghani, T.; Glass, G.; Hoffman, T.; Jan, C.H.; Kenyon, C.; Klaus, J.; Kuhn, K.; Zhiyong Ma, Brian Mcintyre, Kaizad Mistry, Anand Murthy,, Borna Obradovic, Nagisetty, R.; Nguyen, P.; Sivakumar, S.; Shaheed, R.; Shifren, L.; Tufts, B.; Tyagi, S.; Bohr, M.; and El-Mansy, Y. (2004) A 90-nm Logic Technology Featuring Strained-Silicon. *IEEE Transactions on Electron Devices*. Vol. 51, No. 11, pp. 1790-1797.

Timoshenko, S.P. and Gere, J.M. (1963). *Theory of Elastic Stability (2ed)*. McGraw-Hill, New York. 541 pp.

Timoshenko, S.P. and Woinowsky-Krieger, S. (1959). *Theory of Plates and Shells (2ed)*. McGraw-Hill, New York. 580 pp.

Treloar, L.R.G. (1975). *The Physics of Rubber Elasticity,* Clarendon Press, Oxford, Third Edition. 310 pp.

Volynskii, A.L.; Bazhenov, S.; Lebedeva O.V. and Bakeev, N.F. (2000). Mechanical Buckling Instability of Thin Coatings Deposited on Soft Polymer Substrates. *Journal of Materials Science*. Vol. 35, pp. 547-554.

Vonach, W.K. and Rammerstorfer, F.G. (2000). Wrinkling of thick orthotropic sandwich plates under general loading conditions. *Archive of Applied Mechanics*. Vol. 70, pp. 338- 348.

Wagner, S.; Lacour, S.P.; Jones, J.; Hsu, P.H. I.; Sturm, J.C.; Li, T.; Suo, Z. (2004). Electronic Skin: Architecture and Components. *Physica E*. Vol.25, pp. 326-334.

Wilder, E.A. Guo, S. Lin-Gibson, S. Fasolka M.J. and Stafford, C.M. (2006). Measuring the Modulus of Soft Polymer Networks via a Buckling-Based Metrology. *Macromolecules*. Vol. 39, pp. 4138-4143.

Wu, M.; Bo, X. Z.; Sturm, J. C. and Wagner, S. (2002). Complementary Metal-Oxide-Semiconductor Thin-Film Transistor Circuits from a High-Temperature Polycrystalline Silicon Process on Steel Foil Substrates, *IEEE Transaction on Electron Devices*. Vol. 49, pp. 1993-2000.

Yoo, P.J.; Suh, K.Y.; Park S.Y. and Lee H.H. (2002). Physical Self-Assembly of Microstructures by Anisotropic Buckling. *Advanced Materials*. Vol. 14, No. 19, pp. 1383-1387.

Yuan, H.-C.; Ma, Z.; Roberts, M. M.; Savage, D.E. and Lagally, M.G. (2006). High-Speed Strained-Single-Crystal-Silicon Thin-Film Transistors on Flexible Polymers. *Journal of Applied Physics*. Vol. 100, 013708.

Publications arising from this research

1. Liu, Z.J.; Koh, C.T. and Lu.C. (2007). Instability and Buckling Analysis Stretchable Silicon System. *ICMAT-07*, Singapore.
2. Koh, C.T.; Liu, Z.J.; Khang, D.Y.; Song, J.; Lu, C.; Huang, Y.; Rogers. J.A. and Koh, C.G. (2007) Edge Effects in Buckled Thin Films on Elastomeric Substrates. *Applied Physics Letter*. Vol. 91, 133113.
3. Kim, D.H.; Choi, W.M.; Ahn, J.H.; Kim, H.S.; Song, J.; Huang, Y.; Liu, Z.J.; Koh, C.G. and Rogers, J.A. (2008). Complementary Metal Oxide Silicon Integrated Circuits Incorporating Monolithically Integrated Stretchable Wavy Interconnects. *Applied Physics Letter*. Vol. 93, 044102.
4. Kim, D.H.; Ahn, J.H.; Choi, W.M.; Kim, H.S.; Song, J.; Huang, Y.; Liu, Z.J.; Lu, C. and Rogers, J.A. (2008). Stretchable and Foldable Silicon Integrated Circuits. *Science*. Vol. 320, pp. 507-511.
5. Song, J.; Jiang, H.; Liu, Z.J.; Khang, D.Y.; Huang, Y.; Rogers, J.A.; Lu, C. and Koh, C.G. (2008) Buckling of a Stiff Thin Film on a Compliant Substrate in Large Deformation. *International Journal of Solids and Structures*. Vol. 45, pp. 3107-3121.

---

1. *Papers 1 and 2 contain the work done in Chapters 4 and 6.*
2. *Paper 4 contains the work done in Chapters 2 and 7.*
3. *Paper 5 contains the work done in Chapter 5.*
4. *Paper 3 contains the extension work of this thesis.*

In all these papers, the candidate's major contribution is in the analytical and numerical studies. The long lists of authors reflect the collaboration between three groups, i.e. Singapore (NUS and IHPC), UIUC and Northwestern University).